Role of Mechanosensitive Chromatin Organization in the Nucleus of Eukaryotic Cells

by

Benjamin Seelbinder

B.A., Otto-von-Guericke University in Magdeburg (Germany) - 2012

M.A., Otto-von-Guericke University in Magdeburg (Germany) - 2014

A thesis submitted to the

Faculty of the Graduate School of the

University of Colorado in partial fulfillment

of the requirement for the degree of

Doctor of Philosophy

Department of Mechanical Engineering

2019

This thesis entitled:

Role of Mechanosensitive Chromatin Organization in the Nucleus of Eukaryotic Cells

written by Benjamin Seelbinder

has been approved for the Department of Mechanical Engineering

_____

Corey P. Neu, Ph. D.

_____

Sarah Calve, Ph. D.

Date_____

The final copy of this thesis has been examined by the signatories, and we find that both the content and the form meet acceptable presentation standards of scholarly work in the above mentioned discipline.

IACUC protocol # 1507.01

ABSTRACT

Seelbinder, Benjamin (Ph.D., Mechanical Engineering)
Department of Mechanical Engineering, University of Colorado at Boulder

Role of Mechanosensitive Chromatin Organization in the Nucleus of Eukaryotic Cells

Thesis directed by Professor Corey P. Neu

In the human body, there are about 200 different cell types that share a common genome but have specialized roles. During development, cells use mechanical cues from their environment as a guide for tissue-specific cell differentiation, a phenomenon referred to as mechanosensation. The mechanisms underlying mechanosensitive adaptation of cells to their environment are still debated, however. The cell's nucleus is thought to be a mechanosensitive organelle as it is tightly connected to all parts of the cytoskeleton. The disruption of nuclear connections, in disease or experiments, have shown to abrogate cellular responses to mechanical stimuli. Furthermore, the spatial organization of chromatin in the nucleus has emerged as a new mechanism to control local and global gene transcription. The organization of chromatin changes dynamically from an unstructured organization in the zygote to a cell type-specific chromatin architecture during development. Since the nucleus is a large organelle within a cell, its morphology has also been directly linked to the function of differentiated cells.

Taken these concepts together, it can be hypothesized that mechanical cues from the environment influence cell behavior through the spatial reorganization of chromatin and, further, that this reorganization is mediated by forces transmitted to nucleus. In this thesis, the dynamic change in chromatin arrangements in response to mechanical stimuli and its role in cell function were investigated. Chapter 1 provides an overview of the hierarchical organization of chromatin

in the nucleus and its evolution during development. Showcased are also examples of cell type-specific nuclear architectures and their morphological relevance for distinct cell functions. In Chapter 2, a new device for the live imaging of cells under cyclic stretch is presented and utilized to analyze the dynamic response of mouse embryonic fibroblasts to different magnitudes of strain. Findings from this study suggest that rapid nuclear condensation might be a mechanism to protect from DNA damage under high strain loads. Chapter 3 investigates the influence of contraction-mediated nuclear strains on the reorganization of chromatin in embryonic mouse cardiomyocytes during development. The results from this research showed that CMs establish a cell-type specific nuclear architecture that was mediated through the transfer of strain from myofibrils to the nucleus. Overall, the results in thesis support that intranuclear strains influence the organization of chromatin and direct cell behavior on short-term scales and cell differentiation on long-term scales.

To Supriya,

thanks for always being there for me.

TABLE OF CONTENTS

LIST OF TABLES

LIST OF FIGURES

Chapter 1

Mechanisms and Functions of Cell Type-specific Chromatin Organization

ABSTRACT

The human body consists of about 200 different cell types that share a common genome but have diverse morphologies and functions to fulfill specialized roles. How differential gene expression is coordinated during development and maintained throughout an organism's life is far from understood. The spatial organization chromatin in the nucleus has emerged as a new mechanism to control transcriptional activity from the single gene up to gene networks. The organization of chromatin changes dynamically from an unstructured organization in the zygote to cell type-specific chromatin arrangements during development. Here we showcase examples of cell type-specific nuclear architectures and summarize recent paradigms of chromatin organization. We describe chromatin organization changes during development, morphological functions of cell type-specific nuclear architectures and discuss the potential underlying mechanisms of nuclear architectures. Overall, the organization of chromatin has turned out to be remarkedly structured on several scales, the underlaying mechanisms are still largely debated, however.

1.1. CHROMATIN ORGANIZATION

The genetic information is conserved in a 4-letter code represented by nucleotides that form long double stranded deoxyribonucleic acid (DNA) molecules. The human genome consists of 23 long DNA molecules (chromosomes) that range in size from 46-250 million nucleotide base pairs (bp) resulting in a total of 3 billion bp. All somatic cells contain two sets of chromosomes and therefore, considering that one bp is approximately 0.34 nm, harbor 2 m of genetic material in nucleus with a diameter of about 5 µm[1,2]. Despite these numbers, DNA was long thought to be randomly distributed inside the nucleus like a ball of entangled strings. However, newer evidence showed that DNA is highly organized and that this organization might be crucial in local and global gene regulation. In this section, we want to summarize the current paradigms of structural DNA organization in the nucleus of eukaryotic cells.

1.1.1. Nucleosome

To manage the large amount of genetic information, DNA is compacted inside the nucleus as it wraps in regular intervals (200 ± 40 bp) around octameric protein complexes, comprised of histones, to form a nucleosome (**Figure 1.1**)[3]. Nucleosomes dynamically assemble into compact domains that, due to their constant exchange of constituent nucleosomes, behave like a "liquid drop"[4]. The interaction and exchange rate of nucleosomes, and therefore chromatin compaction and accessibility, can be altered through post-translation modifications of amino acid residues at the histone surface[4], either directly by changing charge-interactions[5] or by recruiting protein complexes that control gene transcription and chromatin positioning[6].

1.1.2. Chromosome Territories

The organization of DNA into loose, accessible euchromatin and condensed, closed off heterochromatin along a chromosome strand is a well-established concept. But only recently has

it been shown that chromosome themselves are spatially organized within the nucleus. The notion that chromatin might also be spatially segregated was postulated as early as 1885 by Carl Rabl[7] and again by Theodor Boveri who coined the term Chromosome Territory in 1909[8]. However, the idea of chromosome territories was discarded with the advent of electron microscopy as the intermingling of chromatin was thought to be directly observed. Henceforth the "spaghetti model" of essentially randomly organized chromatin prevailed until 1970 when a group of researchers (Stephen M. Stack, David B. Brown and William C. Dewey) tried to find first proof for Rabl's and

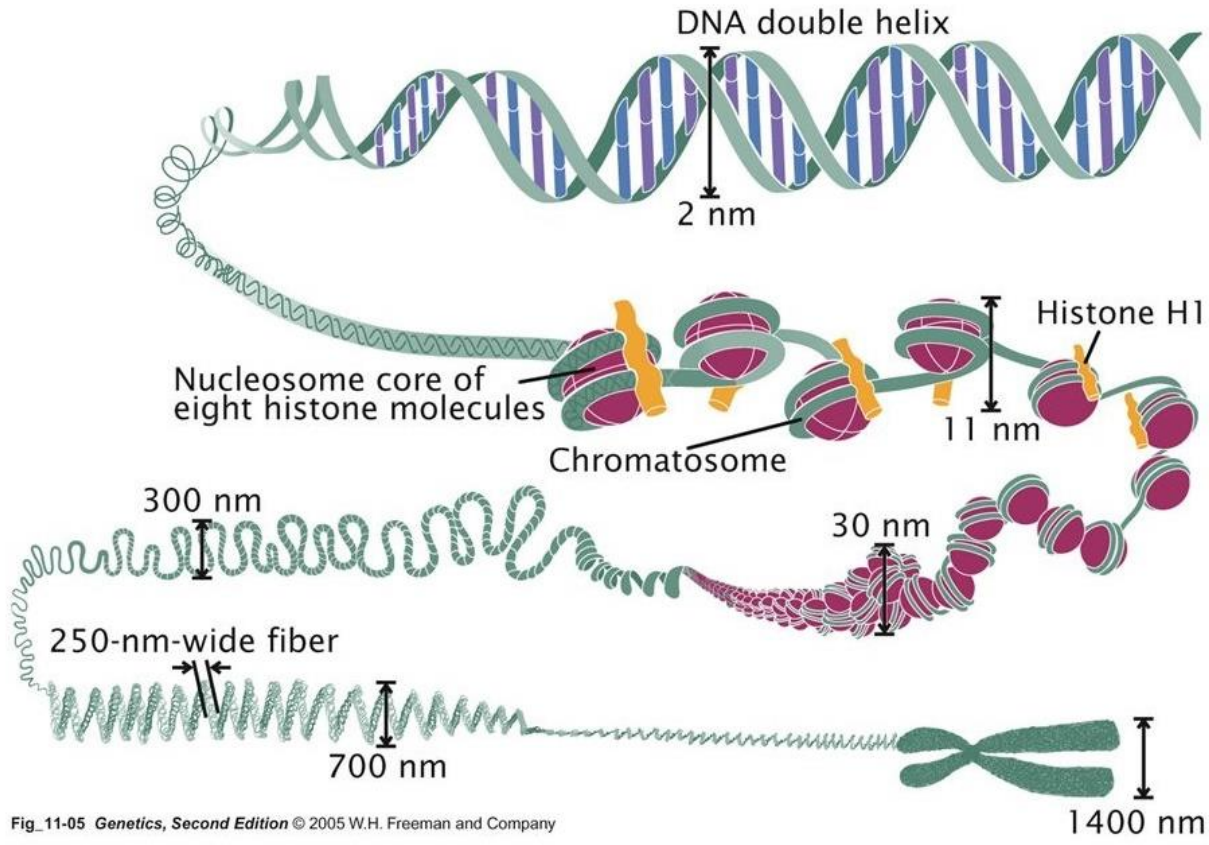

Figure 1.1. DNA compaction through histone scaffolding. In the nucleus, DNA is repeatably wound around octameric histone cores. The resulting nucleosomes form a compact chromatin fiber; adopted from[3]

Boveri's theory. More definitive evidence was provided shortly after by the team of Zorn *et al.* The team observed that when damage was applied only to a small part of the nucleus, using an UV-laser, that this damage would be confined to a small number of chromosomes[9]. Later, as sequence specific chromatin dyes became available, researchers definitively showed that chromosomes indeed stay confined within their region with remarkably low overlap (**Figure 1.2a**)[10,11]. Some findings suggest that this precise abidance of chromosome territories is facilitated by motor proteins[6]; however, the actual mechanisms if still largely debated.

1.1.3. Compartments and TADs

On a smaller scale, chromosome territories are organized into layered compartments of topological-associated domains (TAD, **Figure 1.2b**)[11,12]. Genome regulation depends on the interaction of distant regulatory elements. TADs are regions on the genome (usually several hundred kilobases) with high local interactions between regulatory elements[13]. TADs are also physically constraint as they form chromatin loops through the binding of insulator proteins, such as cohesin, at their boundary[14]. TADs of the same type cluster together over long distances to form compartments[15,16]. There are two main types of compartments: A-compartments that contain active gene rich TADs and B-compartments that contain inactive gene poor TADs. A-compartments are more likely found towards the nuclear interior, while B-compartments are more frequently found at the nuclear periphery[17] where they are also referred to as lamina-associated domains (LAD)[18]. A and B-type compartment can be further categorized into sub-types (A1-2 and B1-3) which are again defined through the clustering of TADs of the same type[19].

1.1.4. Chromatin Hubs

Like the genome, processes in the nucleus are also structured and compartmentalized. In the classical view, free-floating transcription enzymes (polymerases) would translocate and bind

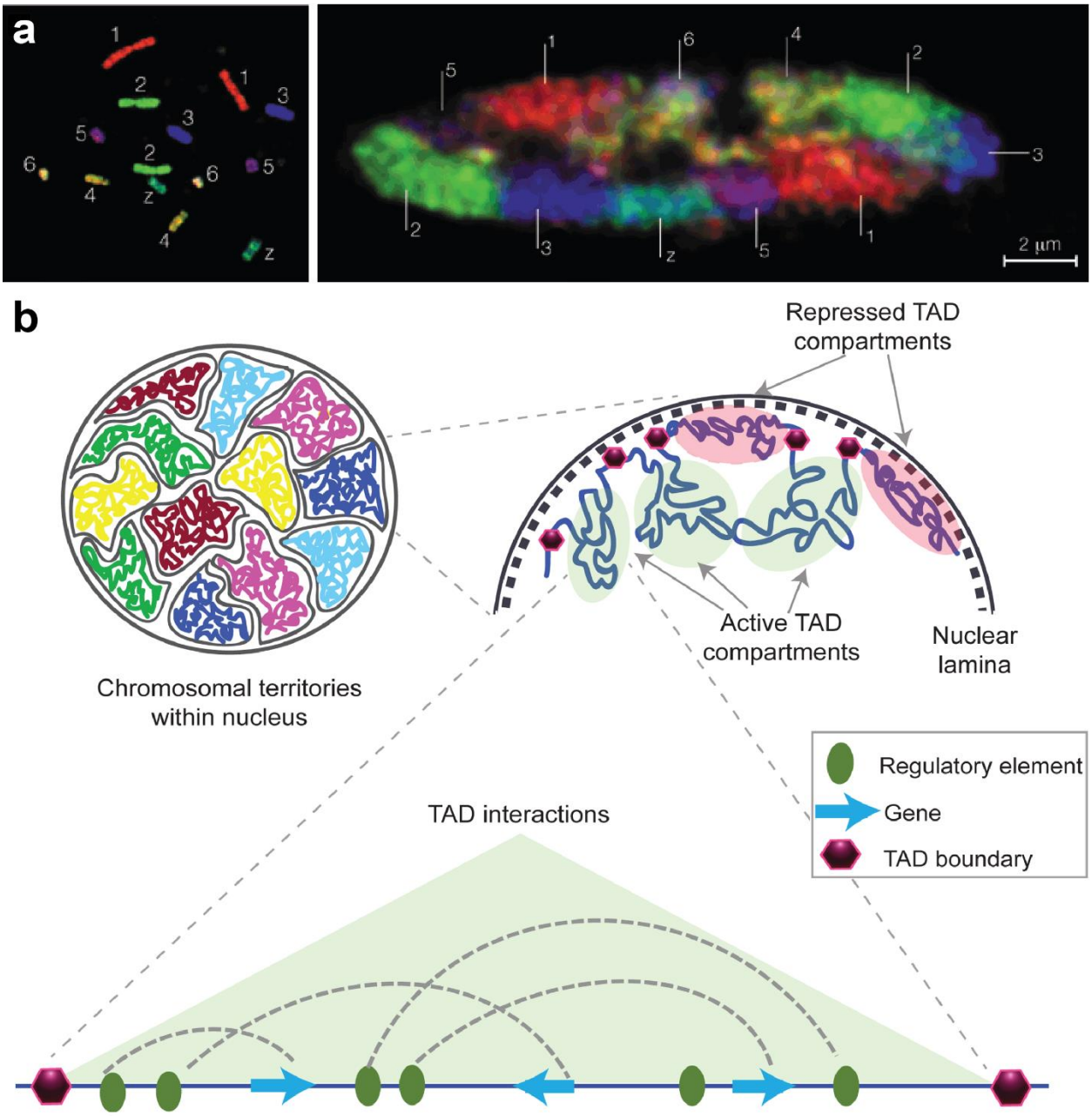

Figure 1.2. Spatial organization of chromatin in the nucleus. a) Fluorescently labeled oligonucleotides enable the sequence specific staining of chromatin. Left: Staining of condensed and isolated chicken chromosomes shows chromosome specific staining. Right: The same staining in a chicken fibroblast nucleus shows that chromosomes stay mostly within their territory; modified from[7]. **b)** Chromosomes are structured into regions with increased internal interaction between regulatory elements, called topological associated domains (TAD). TADs from different chromosomes cluster together into transcriptionally active and inactive compartments, with active comportments being positions towards the nuclear interior; modified from[11].

to chromatin in an undirected fashion. However, newer findings suggest that RNA polymerases are fixed to the nuclear scaffold with genes being moved to and simultaneously transcribed by an array of fixed polymerases, called a transcription factory[20,21]. Active TADs from one or multiple neighboring chromosomes loop out and cluster into active chromatin hubs were they are transcribed by transcription factories[22]. Transcription and post-transcriptional processes (e.g. splicing) involve many multiprotein complexes. Amongst other reason, this way of transcription might have developed due to its ability to locally concentrate and therefore coordinate and share these costly proteins more effectively. Other functional hubs in the nucleus include repair factories, which contain high concentrations of DNA repair enzymes[23]. As with chromosome territories, the relocation of genes to these hubs seems to be driven by motor proteins as knock down of nuclear myosin I has shown to inhibit transcriptional activity[21] and chromatin repair[23]. Due to these findings, the spatial organization of chromatin has emerged as a new key player to control global and single gene regulation, particularly during development.

1.1.5. Chromatin Organization During Development

Since the emergence of chromatin organization as a new mechanism for gene regulation, efforts have been made to map the change of this organization during embryonic development. Analysis of matured mouse sperm showed that the genomic organization was remarkably similar to that of differentiated cells[24,25], despite the sperm genome being haploid and mostly transcriptionally inactive. In contrast, genomic organization in mouse oocytes was shown to be different from that of somatic cells[26] and changed dramatically during development. Oocytes decrease their transcriptional activity during maturation. At the same time, genomic organization has been found to be decreased as well and mature oocytes are void of TADs and compartments

and show a uniform, decondensed distribution of chromatin with little variation in contact probabilities across the genome[26,27].

After fertilization, chromatin organization increased gradually in the formed zygote, as measured by the formation of TADs and compartment, during each stage of development[28–30]. Most analysis of chromatin organization is performed using chromatin conformation capture techniques (Hi-C sequencing) to analyze the interaction probability of genomic regions. Microscopy studies further showed that chromatin became more mobile[31] and that gene-rich chromatin regions shifted from being randomly distributed to having a distinct chromosome-specific distribution after fertilization[32]. By using whole chromosome stains, nuclear position of different chromosomes were observed to be more likely to be similar between cells of the same cell type and, furthermore, amongst cell types of the same tissue[33]. Since different cell types of the same tissue share differentiation pathways and active gene networks, the group argued that the similarity in chromosome arrangement might arise from the clustering of related networks into similar chromatin compartments.

While studies agree that chromatin organization in zygotes undergoes stark changes after fertilization, there is still dispute over the dynamics of these changes during development. Findings in Zebrafish, for example, showed that zygotes start out with a higher order of organization, which then subsided after fertilization and increased again during later stages[34]. It is also unclear how cell-type specific nuclear architectures gradually emerge from the decondensed, underordered organization in the zygote and more work is needed to understand these processes. Next, we want to explore functional aspects of chromatin organization that go beyond the implications of gene regulation.

1.2. MORPHOLOGICAL FUNCTIONS OF NUCLEAR ARCHITECTURES

Cells of the same type show a common genome organization, presumably due to the clustering of similar gene networks into shared chromatin compartments, as discussed above. The spatial arrangement of chromatin is likely to have major role in gene regulation and the establishment of genetic memories through the spatial segregation of chromatin. However, studies of different distinct cell types suggest that establishment of cell-type specific nuclear architectures has implications beyond gene regulation. In these examples, shape and mechanical properties of the nucleus directly contribute to the cell's functions.

1.2.1. Light Guidance in Mouse Rod Receptor Cells

Silenced condensed chromatin is primarily found at the nuclear envelope while lightly packed transcribed chromatin is more likely situated towards the nuclear interior in somatic cells. The team of Solovei *et al.* reported that the rod receptor cells in the eyes of mice have an inverted architecture with a dense core of chromatin concentrated in the center of the nucleus (**Figure 1.3a**)[35]. This inverted nuclear architecture was only found in nocturnal animals[36] and the team argued that the dense chromatin core could act as a lens to focus light deeper into the underlying receptors. Computational modeling of light propagation through retinas with different nuclear architectures further verified this hypothesis.

1.2.2. Signal Integration in Hippocampal Neurons

In a different study, the group of Wittmann *et al.* observed that neurons in the hippocampus tend to have strongly folded nuclear envelopes[37]. By culturing hippocampal neurons *in vitro*, the group further revealed that neuronal nuclei formed these folds dynamically in response to induced synaptic activity and that the nuclei reverted to a round shape after inhibition of synaptic activity (**Figure 1.3c**). Neurons use their cell body to integrate incoming signals in the form of calcium

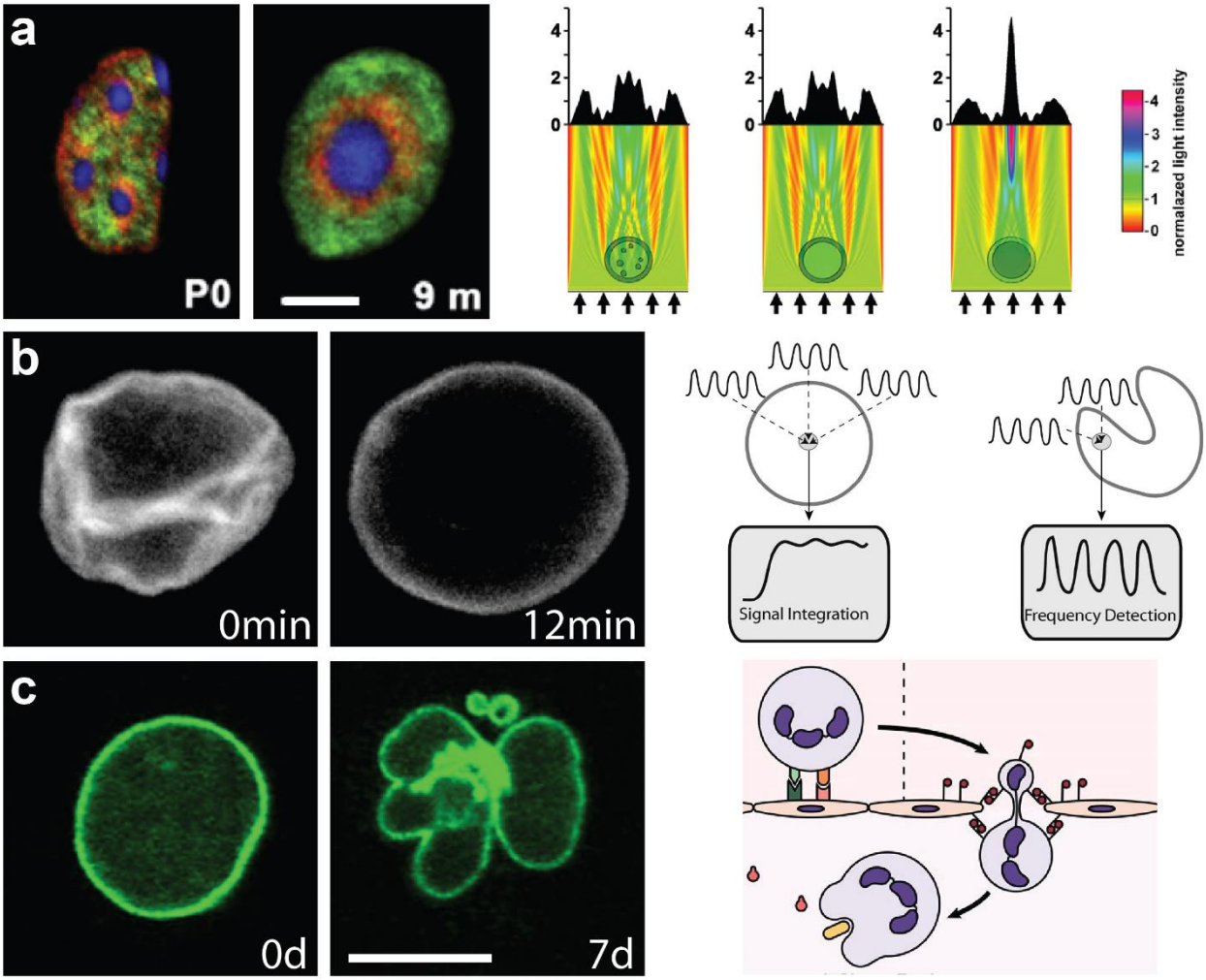

Figure 1.3. Morphological functions of nuclear architectures. a) Chromatin arrangement of rod receptor cells at birth (P0) and in 9-month-old adult mice. Matured nuclei show an inverted architecture with a dense chromatin core in the center acting like a light collecting lens; chromatin density: blue=dense (chromocenters, H3K9me3), red=medium (hetero-chromatin, H3K20me3), green=light (euchromatin, H3K4me3); scale=2 µm; modified from[42]. **b)** Live imaging of hippocampal neuron nuclei (Lamin B-eGFP) show the reduction of nuclear infoldings before (0 min) and 12 min after inhibition of synaptic activity via NMDA. Nuclear compartmentalization through infoldings change neuronal signal integration; modified from[44,45]. **c**) Nuclear envelope (Lamin B staining) before (0 d) and 7 days after induction of granulocyte differentiation. Cells develop a compliant multilobed nuclear architecture for enhanced tissue invasion; scale=10 µm; modified from[46].

waves. Since neuronal bodies (soma) are very small, their nucleus makes up most of their cell body. In a follow-up study, the group investigated whether the compartmentalization of the nucleus, as a result of nuclear membrane folding, is used by neurons to modulate calcium transients. Through computational modeling of calcium propagation in neurons with different (previously recorded) nuclear morphologies, the group showed that folded nuclei are more sensitive to calcium signals and, further, that the compartmentalization of folded nuclei might be used to distinguish between constant and oscillatory calcium waves[38].

1.2.3. Enhanced Tissue Invasion of Neutrophil Granulocytes

In another example, the group around Olins *et al.* investigated the formation of multi-lobed nuclei during the differentiation of neutrophil granulocytes (**Figure 1.3b**)[39]. Neutrophils patrol the body in search of infection and may need to squeeze through narrow gaps between tissues to reach their target. The group suggested that the formation of a compliant multi-lobed nucleus enhances the neutrophil's capability for tissue invasion. In a follow-up study, the group further verified that nuclear lamina proteins, the main contributors of nuclear mechanical resilience, are strongly reduced or absent in neutrophils[40]. In a related example, sperm must be very compact to compete effectively. Despite having a similar TAD and compartment structure, the DNA in sperm nuclei is extremely tightly packed through scaffolding onto protamine instead of histones[24]. These examples highlight that nuclear organization might not just be genetically but also morphologically integral for the function of differentiated cells.

1.3. NUCLEOSKELETON

To discuss the potential mechanisms that underlie chromatin organization, it is important to review current findings of the skeleton structures in and around the nucleus they likely provide the scaffold that enables these processes.

1.3.1. Nuclear Lamina

The nucleus is compartmentalized by two lipid bilayer membranes. The outer nuclear membrane has large outward bulges that form the endoplasmic reticulum in which all membrane proteins are synthesized. The inner nuclear membrane is lined with a fibrous protein meshwork, called the nuclear lamina, which provides mechanical stability and connects the nucleus to other parts of the cell. The nuclear lamina is comprised of two separate but overlapping protein networks that consist intermediate filament-type proteins called lamins. A-type lamins form a thick meshwork with viscoelastic properties, while B-type lamins form a thin meshwork with elastic mechanical properties that is connected to the inner nuclear membrane[41]. Both networks combined provide flexibility and resilience to the nucleus to maintain shape and integrity against external forces. As a result, the nucleus is approximately 5-10 fold stiffer then the cell body[42,43].

1.3.2. LINC Complexes

The increased mechanical stability of the nucleus was puzzling at first as the central location of the nucleus within the cell body would seem to blanket it from external forces. However, the nucleus turned out to be interconnected with the cytoskeleton and, by extension, to the extracellular matrix via LINC (Linker of Nucleo- and Cytoskeleton) complexes[44]. LINC complexes are comprised of structural proteins that span the outer (nesprins) and inner (SUNs) nuclear membranes. On the outer side of the nucleus, different nesprin isotypes bind to different parts of the cytoskeleton: nesprin-1 and 2 to actin, nesprin-3 to intermediary filaments and

nesprin-4 to microtubules[45,46]. In the perinuclear space between both nuclear membranes, a combination of SUN isotypes form a tetrameric complex that binds to one nesprin through highly conserved KASH domains[47]. On the inner side of the nucleus, the tetrameric SUN complex connects to the nuclear lamina[48].

1.3.3. Nuclear Matrix

Due to its interconnectedness with the rest of the cytoskeleton, the peripheral nucleoskeleton has been implicated in the processing of mechanical cues from the extracellular environment, a phenome referred to as mechanosensation. Cells use these cues to guide their differentiation[49,50] and disruption of these connections have reaching consequences during development, as will be discussed later. Hence, much attention has been focused on studying the peripheral nucleoskeleton. In contrast, the composition and function of the internal nucleoskeleton is far less understood despite being investigated for more than half a century. Early observations using light microscopy found the nucleus to be devoid of internal structure and researchers assumed that the nuclear contents are suspended in a liquid medium called the nuclear sap. The advent of electron microscopy, again, dramatically changed this view and in conjunction with advances in sample preparation techniques the first images of the nuclear scaffolds were recorded in the 1960's (**Figure 1.4a**)[51]. These images show the substructure of the nucleus to be comprised of clusters, called interchromatin granules, which are evenly distributed throughout the nucleus and connected through branching 10 nm sized filamentous fibers (**Figure 1.4b**). This structure has yet to be visualized in living cells and efforts of identifying the composition of the nuclear matrix showed ambiguous results so far[52], hence still leaving the existence of the nuclear matrix as a biological entity in question. One frequently identified constituent is a protein that was first discovered through its involvement in the formation of the spindle apparatus during mitosis, called

nuclear-mitotic apparatus (NuMA) protein[53–55]. With its globular head and tail domains connected by a rod-like coiled-coil domain, NuMA shows many features of a structural protein. Increasing or decreasing of the coiled-coil domain's length, through insertions or deletions, has shown to changes the spacing of the nuclear matrix lattice correspondingly[56]. In the same study, deletions in the head domains also resulted in the reorganization of the nuclear architecture with chromatin and subnuclear bodies predominantly clustering at the nuclear periphery and deletion of the nuclear localization signal showed the formation of aggregates in the cytoplasm with a structure similar to that of the nuclear matrix. NuMA has also been shown to interact with the nuclear lamina[57]. These findings suggest that NuMA plays a critical role for the establishment of nuclear architectures.

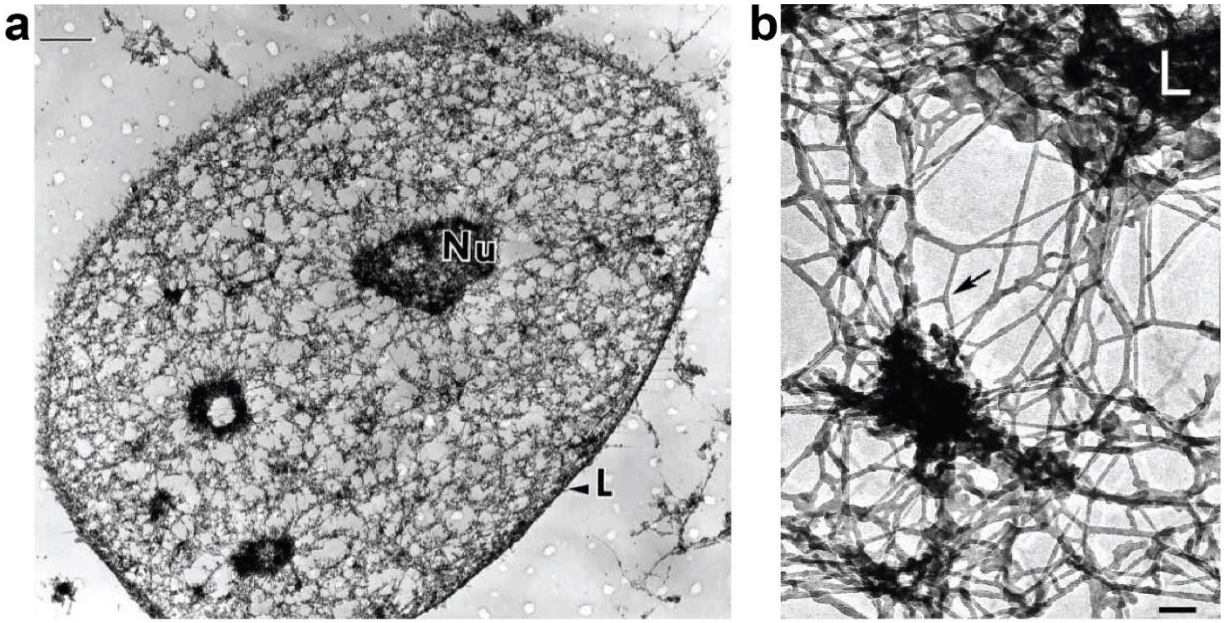

Figure 1.4. Nuclear matrix visualized by electron microscopy. a) After removal of chromatin, a proteinaceous network of connected interchromatin granules can be observed throughout the nucleus using electron microscopy. Indicated are the nucleolus (Nu) and the nuclear lamins (L); scale=1 µm. **b)** At higher magnification, branching fibers of 10 nm thick filaments connect different interchromatin granules with each other and to the nuclear lamina can be observed; scale=0.1 µm; adopted from[50].

1.3.4. Nuclear Actin

Actin is another structural protein found in the nucleus, but whose function is better understood in the cellular processes. In the cytoplasm, filamentous actin is one of the three cytoskeleton components and majorly contributes to the cell's resistance to tensile forces[58]. At the same time, actin is highly dynamic and can serve as a scaffold for myosin motor proteins to exert force for cell migration and cell divisions but also to transport cargo and arrange organelles[59]. Actin itself has no nuclear location sequence and is imported into the nucleus via cofilin[60]. The concentration of actin in the cytoplasm usually far exceeds that in the nucleus and nuclear actin was first observed in amphibian oocytes where its concentration is relatively high. Since actin plays a role in cellular organization, it was assumed that it might have a similar function in the nucleus. However, the function of nuclear actin is still under debate.

1.4. MECHANISMS OF CHROMATIN ORGANIZATION

In the previous sections, we discussed that the spatial arrangement of chromatin is tightly controlled from the single gene up to genomic scales. It is unknown how this organization is facilitated or regulated; however, studies have provided evidence for different potential mechanisms that might be involved in chromatin organization and which are summarized in this section.

1.4.1. Chromatin Insulators

TAD boundaries are enriched for a binding sequence that is recognized by the zinc-finger protein CTCF (CCCTC-binding factor)[16,61]. CTCF further recruits cohesion, a multi-protein complex that forms a ring like structure around the TAD boundaries thereby forming a chromatin loop[4,62]. The formation of a loop increases the interaction of gene regulatory elements within a TAD, hence

CTCF and cohesion are also known as insulator proteins. Post-translational modification of histone amino acid residues, known as epigenetic modifications, control gene regulation through changes in chromatin compaction[5] or recruitment of effector proteins[6]. Evidence suggests that epigenetic modifications also regulate the clustering of TADs with similar activity into chromatin compartments. Transcriptionally-active A-type compartments are associated with activating histone modification such as H3K4me1 (methylation of histone H3 at lysine 4) and H3K36me3 (trimethylation of histone H3 at lysine 36) while inactive B-type compartments are associated with H3K27me3 and H3K9me3 modifications that silence and compact chromatin[19]. Further, TADs have shown to switch from A to B-type compartments after recruitment of the H3K9me3 methyltransferase SUV39H1[63].

1.4.2. Lamins and NETs

B-type compartment are more frequently found in transcriptionally repressed regions of the nucleus such as the nucleolus and the nuclear lamina, while nuclear lamina and nucleolus-associated domains (LAD, NAD) are depleted in A-type compartments[19]. In most somatic cells, the nuclear lamina is associated with a layer of condensed chromatin. This is facilitated through nuclear envelope transmembrane proteins (NETs) that integrate into the inner nuclear membrane and contain lamina and chromatin binding domains. Importantly, multiple studies have shown that NETs are tissue-specifically expressed[64–67], and evidence suggests that they mediate tissue specific chromosome positioning. Even though NETs are anchored to the nuclear membrane, lamina-interaction or the lamina itself appears to be crucial for the tethering of chromatin to the nuclear periphery as deletion of A or B-type lamins phenocopied the inverted architecture of mouse rod receptor cells with most chromatin concentrated at the nuclear center[68]. The interaction of NETs with chromatin also appears to be dependent on epigenetic modifications[69] and current

investigations are focused on understanding the interdependent relationships of epigenetics and NET expression in the formation of cell type-specific chromatin organization[70].

1.4.3. Nuclear Actin and Myosin

How chromatin is repositioned is largely unclear; however, evidence suggests the involvement of nuclear motor proteins. Different studies showed that the reorganization of chromosome territories in response to transcriptional activation[71], serum starvation[6] or induction of DNA damage[23] was abrogated after inhibition of nuclear myosin 1 (NM1). Myosin motor proteins classically depend on actin as a scaffold for translocation and disruption of actin has also been shown to interfere with chromatin repositioning after transcriptional activation[71,72]. In contrast, the team of Belin *et al.* engineered a fluorescent probe to investigate nuclear actin activity in living cells and concluded that the short filament length (<100 subunits), the dynamic motion and the minor colocalization with nuclear myosins made actin unsuitable for long range transports[73]. The role of nuclear actin is still widely debated and nuclear myosins, other than NM1, are poorly characterized, leaving more research to be done to understand their role in chromatin positioning.

1.4.4. Nuclear Matrix

The nuclear matrix is another likely candidate to act as a scaffold for directed chromatin organization. Investigation of chromatin interactions with the nuclear matrix identified AT-rich matrix-attachment regions (MAR)[74] and targeting antibodies against the nuclear matrix protein NuMA disrupted chromatin organization and inhibited differentiation of liver acina[75]. Expression of a truncated NuMA protein also altered the distribution of epigenetically modified chromatin[75] and caused the relocation of chromatin and the nucleolus to the nuclear envelope[56]. While the

mechanistic details are unclear, these findings show that the nuclear matrix is likely to play an important role for the organization of chromatin.

1.4.5. Nuclear Mechanosensation

LINC complexes connect the nucleus to the cytoskeleton. LINC complex protein are not directly involved in the organization of chromatin; however they forward mechanical signals from the cytoskeleton into the nucleus which can trigger changes in chromatin organization[76], gene expression[77,78] and cell differentiation[78]. Mechanical cues from the environment are known to guide cell differentiation[49] and mutations in LINC complex and associated nuclear envelope proteins can cause severe developmental disorders[79,80]. Taken together, this might suggest that biophysical signals from the cell environment guide cell fate through the reorganization of chromatin.

1.5. SUMMARY AND OUTLOOK

The accumulated findings over the last decades have completely changed the paradigms of chromatin organization from the “spaghetti model” of randomly entangled chromosomes to a model that shows fine-tuned chromatin organization at different scales from the single up to the whole genome. This organization is established throughout development starting from a largely unorganized arrangement which is step-wide structured into a cell type-specific nuclear architecture. Therefore, the role of chromatin organization in gene regulation and cell differentiation is well establish. The maintenance of stable cell differentiation throughout an organism’s life is also likely facilitated through the permanent spatial segregation of chromatin. There is even good evidence that the morphological structure of the nucleus can be integral to a cell’s function. However, the underlying mechanisms of active chromatin relocation and the

preservation of chromatin locations is largely unknown and findings from proposed mechanisms are still debated. Research into NETs for the cell type-specific tethering of chromatin at the nuclear border are currently underway and should provide further clues how chromatin organizations are established during development. More efforts should be focused on the investigation of the nuclear matrix and other structural protein in the nucleus since it appears likely that the dynamic organization of chromatin is dependent on an underlying scaffold.

The nucleus has further shown to be important in the processing of biophysical cues from the environment. It is plausible to assume that this is partially achieved through changes in chromatin organization; however, the influence of nuclear strain on chromatin positioning has not been studied so far. In **Chapter 3** of this thesis, we present our findings on the influence of contraction-mediated nuclear strains on chromatin reorganization during the development and disease of mouse cardiomyocytes. Further, the fine resolution of organizational chromatin hierarchies is largely based advances in sequencing methods. These methods can resolve chromatin interactions at the sequence level but have poor temporal resolution since they can only make observations in a bulk sample of cells at the time of sample preparation. Other methods need to be developed to observe the dynamic response of chromatin in single cells, for example to mechanical stimuli. A new device for the high-magnification imaging of live cells under cyclic stretch and the resulting findings in mouse embryonic fibroblasts are presented in the following **Chapter 2**.

1.6. REFERENCES

1. Campbell, N. A. & Reece, J. B. *Biology : concepts & connections*. (Addison Wesley Longman, 1997).
2. Bloom, K. & Joglekar, A. Towards building a chromosome segregation machine. *Nature* **463**, 446–56 (2010).
3. Pierce, B. A. *Genetics : a conceptual approach*. (W.H. Freeman, 2005).
4. Nozaki, T. *et al.* Dynamic Organization of Chromatin Domains Revealed by Super-Resolution Live-Cell Imaging. *Mol. Cell* **67**, 282-293.e7 (2017).
5. Lawrence, M., Daujat, S. & Schneider, R. Lateral Thinking: How Histone Modifications Regulate Gene Expression. *Trends Genet.* **32**, 42–56 (2016).
6. Mehta, I. S., Amira, M., Harvey, A. J. & Bridger, J. M. Rapid chromosome territory relocation by nuclear motor activity in response to serum removal in primary human fibroblasts. *Genome Biol.* **11**, R5 (2010).
7. Rabl, C. Über Zelltheilung. *Morphol. Jahrb.* **10**, 214–330 (1885).
8. Cremer, T. & Cremer, M. Chromosome territories. *Cold Spring Harb. Perspect. Biol.* **2**, a003889 (2010).
9. Zorn, C., Cremer, T., Cremer, C. & Zimmer, J. Laser UV microirradiation of interphase nuclei and post-treatment with caffeine. *Hum. Genet.* **35**, 83–89 (1976).
10. Manuelidis, L. Individual interphase chromosome domains revealed by in situ hybridization. *Hum. Genet.* **71**, 288–93 (1985).
11. Cremer, T. & Cremer, C. Chromosome territories, nuclear architecture and gene regulation in mammalian cells. *Nat. Rev. Genet.* **2**, 292–301 (2001).
12. Matharu, N. & Ahituv, N. Minor Loops in Major Folds: Enhancer-Promoter Looping, Chromatin Restructuring, and Their Association with Transcriptional Regulation and Disease. *PLoS Genet.* **11**, e1005640 (2015).

13. Pope, B. D. *et al.* Topologically associating domains are stable units of replication-timing regulation. *Nature* **515**, 402–405 (2014).

14. Rao, S. S. P. *et al.* Cohesin Loss Eliminates All Loop Domains. *Cell* **171**, 305-320.e24 (2017).

15. Lieberman-Aiden, E. *et al.* Comprehensive mapping of long-range interactions reveals folding principles of the human genome. *Science* **326**, 289–93 (2009).

16. Dixon, J. R. *et al.* Topological domains in mammalian genomes identified by analysis of chromatin interactions. *Nature* **485**, 376–380 (2012).

17. Bolzer, A. *et al.* Three-dimensional maps of all chromosomes in human male fibroblast nuclei and prometaphase rosettes. *PLoS Biol.* **3**, e157 (2005).

18. Guelen, L. *et al.* Domain organization of human chromosomes revealed by mapping of nuclear lamina interactions. *Nature* **453**, 948–951 (2008).

19. Rao, S. S. P. *et al.* A 3D Map of the Human Genome at Kilobase Resolution Reveals Principles of Chromatin Looping. *Cell* **159**, 1665–1680 (2014).

20. Sutherland, H. & Bickmore, W. A. Transcription factories: gene expression in unions? *Nat. Rev. Genet.* **10**, 457–466 (2009).

21. Almuzzaini, B., Sarshad, A. A., Farrants, A. K. Ö. & Percipalle, P. Nuclear myosin 1 contributes to a chromatin landscape compatible with RNA polymerase II transcription activation. *BMC Biol.* **13**, 1–15 (2015).

22. de Laat, W. & Grosveld, F. Spatial organization of gene expression: the active chromatin hub. *Chromosome Res.* **11**, 447–59 (2003).

23. Kulashreshtha, M., Mehta, I. S., Kumar, P. & Rao, B. J. Chromosome territory relocation during DNA repair requires nuclear myosin 1 recruitment to chromatin mediated by ϒ-H2AX signaling. *Nucleic Acids Res.* **44**, 8272–91 (2016).

24. Battulin, N. *et al.* Comparison of the three-dimensional organization of sperm and fibroblast genomes using the Hi-C approach. *Genome Biol.* **16**, 77 (2015).

25. Jung, Y. H. *et al.* Chromatin States in Mouse Sperm Correlate with Embryonic and Adult

Regulatory Landscapes. *Cell Rep.* **18**, 1366–1382 (2017).

26. Flyamer, I. M. *et al.* Single-nucleus Hi-C reveals unique chromatin reorganization at oocyte-to-zygote transition. *Nature* **544**, 110–114 (2017).

27. Hug, C. B., Grimaldi, A. G., Kruse, K. & Vaquerizas, J. M. Chromatin Architecture Emerges during Zygotic Genome Activation Independent of Transcription. *Cell* **169**, 216-228.e19 (2017).

28. Ke, Y. *et al.* 3D Chromatin Structures of Mature Gametes and Structural Reprogramming during Mammalian Embryogenesis. *Cell* **170**, 367-381.e20 (2017).

29. Du, Z. *et al.* Allelic reprogramming of 3D chromatin architecture during early mammalian development. *Nature* **547**, 232–235 (2017).

30. Gassler, J. *et al.* A mechanism of cohesin-dependent loop extrusion organizes zygotic genome architecture. *EMBO J.* **36**, 3600–3618 (2017).

31. Bošković, A. *et al.* Higher chromatin mobility supports totipotency and precedes pluripotency in vivo. *Genes Dev.* **28**, 1042–7 (2014).

32. Koehler, D. *et al.* Changes of higher order chromatin arrangements during major genome activation in bovine preimplantation embryos. *Exp. Cell Res.* **315**, 2053–2063 (2009).

33. Parada, L. A., McQueen, P. G. & Misteli, T. Tissue-specific spatial organization of genomes. *Genome Biol.* **5**, R44 (2004).

34. Kaaij, L. J. T., van der Weide, R. H., Ketting, R. F. & de Wit, E. Systemic Loss and Gain of Chromatin Architecture throughout Zebrafish Development. *Cell Rep.* **24**, 1-10.e4 (2018).

35. Solovei, I. *et al.* Nuclear architecture of rod photoreceptor cells adapts to vision in mammalian evolution. *Cell* **137**, 356–68 (2009).

36. Solovei, I. & Joffe, B. Inverted nuclear architecture and its development during differentiation of mouse rod photoreceptor cells: A new model to study nuclear architecture. *Russ. J. Genet.* **46**, 1029–1032 (2010).

37. Wittmann, M. *et al.* Synaptic activity induces dramatic changes in the geometry of the cell

nucleus: interplay between nuclear structure, histone H3 phosphorylation, and nuclear calcium signaling. *J. Neurosci.* **29**, 14687–700 (2009).

38. Queisser, G., Wiegert, S. & Bading, H. Structural dynamics of the cell nucleus: basis for morphology modulation of nuclear calcium signaling and gene transcription. *Nucleus* **2**, 98–104 (2011).

39. Olins, A. L. & Olins, D. E. Cytoskeletal influences on nuclear shape in granulocytic HL-60 cells. *BMC Cell Biol.* **5**, 30 (2004).

40. Olins, A. L. *et al.* The human granulocyte nucleus: Unusual nuclear envelope and heterochromatin composition. *Eur. J. Cell Biol.* **87**, 279–90 (2008).

41. Swift, J. *et al.* Nuclear lamin-A scales with tissue stiffness and enhances matrix-directed differentiation. *Science* **341**, 1240104 (2013).

42. Guilak, F., Tedrow, J. R. & Burgkart, R. Viscoelastic properties of the cell nucleus. *Biochem. Biophys. Res. Commun.* **269**, 781–6 (2000).

43. Dahl, K. N., Kahn, S. M., Wilson, K. L. & Discher, D. E. The nuclear envelope lamina network has elasticity and a compressibility limit suggestive of a molecular shock absorber. *J. Cell Sci.* **117**, 4779–86 (2004).

44. Crisp, M. *et al.* Coupling of the nucleus and cytoplasm: Role of the LINC complex. *J. Cell Biol.* **172**, 41–53 (2006).

45. Apel, E. D., Lewis, R. M., Grady, R. M. & Sanes, J. R. Syne-1, a dystrophin- and Klarsicht-related protein associated with synaptic nuclei at the neuromuscular junction. *J. Biol. Chem.* **275**, 31986–95 (2000).

46. Zhang, Q., Ragnauth, C., Greener, M. J., Shanahan, C. M. & Roberts, R. G. The nesprins are giant actin-binding proteins, orthologous to Drosophila melanogaster muscle protein MSP-300. *Genomics* **80**, 473–81 (2002).

47. Malone, C. J., Fixsen, W. D., Horvitz, H. R. & Han, M. UNC-84 localizes to the nuclear envelope and is required for nuclear migration and anchoring during C. elegans development. *Development* **126**, 3171–81 (1999).

48. Haque, F. *et al.* SUN1 interacts with nuclear lamin A and cytoplasmic nesprins to provide a physical connection between the nuclear lamina and the cytoskeleton. *Mol. Cell. Biol.* **26**, 3738–51 (2006).

49. Engler, A. J., Sen, S., Sweeney, H. L. & Discher, D. E. Matrix elasticity directs stem cell lineage specification. *Cell* **126**, 677–89 (2006).

50. Engler, A. J. *et al.* Myotubes differentiate optimally on substrates with tissue-like stiffness: Pathological implications for soft or stiff microenvironments. *J. Cell Biol.* **166**, 877–887 (2004).

51. Nickerson, J. Experimental observations of a nuclear matrix. *J. Cell Sci.* **114**, 463–74 (2001).

52. Albrethsen, J., Knol, J. C. & Jimenez, C. R. Unravelling the nuclear matrix proteome. *J. Proteomics* **72**, 71–81 (2009).

53. Radulescu, A. E. & Cleveland, D. W. NuMA after 30 years: The matrix revisited. *Trends Cell Biol.* **20**, 214–222 (2010).

54. Lydersen, B. K. & Pettijohn, D. E. Human-specific nuclear protein that associates with the polar region of the mitotic apparatus: distribution in a human/hamster hybrid cell. *Cell* **22**, 489–99 (1980).

55. Cleveland, D. W. NuMA: a protein involved in nuclear structure, spindle assembly, and nuclear re-formation. *Trends Cell Biol.* **5**, 60–4 (1995).

56. Gueth-Hallonet, C., Wang, J., Harborth, J., Weber, K. & Osborn, M. Induction of a regular nuclear lattice by overexpression of NuMA. *Exp. Cell Res.* **243**, 434–52 (1998).

57. Barboro, P. *et al.* Unraveling the organization of the internal nuclear matrix: RNA-dependent anchoring of NuMA to a lamin scaffold. *Exp. Cell Res.* **279**, 202–18 (2002).

58. Tsuda, Y., Yasutake, H., Ishijima, A. & Yanagida, T. Torsional rigidity of single actin filaments and actin-actin bond breaking force under torsion measured directly by in vitro micromanipulation. *Proc. Natl. Acad. Sci. U. S. A.* **93**, 12937–42 (1996).

59. Ali, M. Y., Vilfan, A., Trybus, K. M. & Warshaw, D. M. Cargo Transport by Two Coupled

Myosin Va Motors on Actin Filaments and Bundles. *Biophys. J.* **111**, 2228–2240 (2016).

60. Pendleton, A., Pope, B., Weeds, A. & Koffer, A. Latrunculin B or ATP Depletion Induces Cofilin-dependent Translocation of Actin into Nuclei of Mast Cells. *J. Biol. Chem.* **278**, 14394–14400 (2003).

61. Vietri Rudan, M. *et al.* Comparative Hi-C reveals that CTCF underlies evolution of chromosomal domain architecture. *Cell Rep.* **10**, 1297–309 (2015).

62. Wutz, G. *et al.* Topologically associating domains and chromatin loops depend on cohesin and are regulated by CTCF, WAPL, and PDS5 proteins. *EMBO J.* **36**, 3573–3599 (2017).

63. Wijchers, P. J. *et al.* Cause and Consequence of Tethering a SubTAD to Different Nuclear Compartments. *Mol. Cell* **61**, 461–473 (2016).

64. de Las Heras, J. I. *et al.* Tissue specificity in the nuclear envelope supports its functional complexity. *Nucleus* **4**, 460–77 (2014).

65. Wilkie, G. S. *et al.* Several Novel Nuclear Envelope Transmembrane Proteins Identified in Skeletal Muscle Have Cytoskeletal Associations. *Mol. Cell. Proteomics* **10**, M110.003129 (2011).

66. Zuleger, N. *et al.* Specific nuclear envelope transmembrane proteins can promote the location of chromosomes to and from the nuclear periphery. *Genome Biol.* **14**, R14 (2013).

67. Makatsori, D. *et al.* The inner nuclear membrane protein lamin B receptor forms distinct microdomains and links epigenetically marked chromatin to the nuclear envelope. *J. Biol. Chem.* **279**, 25567–73 (2004).

68. Politz, J. C. R., Ragoczy, T. & Groudine, M. When untethered, something silent inside comes. *Nucleus* **4**, 153–5

69. Somech, R. *et al.* The nuclear-envelope protein and transcriptional repressor LAP2beta interacts with HDAC3 at the nuclear periphery, and induces histone H4 deacetylation. *J. Cell Sci.* **118**, 4017–25 (2005).

70. Wong, X., Luperchio, T. R. & Reddy, K. L. NET gains and losses: the role of changing nuclear envelope proteomes in genome regulation. *Curr. Opin. Cell Biol.* **28**, 105–120

(2014).

71. Chuang, C.-H. *et al.* Long-range directional movement of an interphase chromosome site. *Curr. Biol.* **16**, 825–31 (2006).

72. Dundr, M. *et al.* Actin-dependent intranuclear repositioning of an active gene locus in vivo. *J. Cell Biol.* **179**, 1095–103 (2007).

73. Belin, B. J., Cimini, B. a, Blackburn, E. H. & Mullins, R. D. Visualization of actin filaments and monomers in somatic cell nuclei. *Mol. Biol. Cell* **24**, 982–94 (2013).

74. Das, A. T., Ludérus, M. E. & Lamers, W. H. Identification and analysis of a matrix-attachment region 5' of the rat glutamate-dehydrogenase-encoding gene. *Eur. J. Biochem.* **215**, 777–85 (1993).

75. Abad, P. C. *et al.* NuMA influences higher order chromatin organization in human mammary epithelium. *Mol. Biol. Cell* **18**, 348–61 (2007).

76. Iyer, K. V., Pulford, S., Mogilner, A. & Shivashankar, G. V. Mechanical activation of cells induces chromatin remodeling preceding MKL nuclear transport. *Biophys. J.* **103**, 1416–1428 (2012).

77. Tajik, A. *et al.* Transcription upregulation via force-induced direct stretching of chromatin. *Nat. Mater.* (2016). doi:10.1038/nmat4729

78. Uzer, G. *et al.* Cell mechanosensitivity to extremely low-magnitude signals is enabled by a LINCed nucleus. *Stem Cells* **33**, 2063–2076 (2015).

79. Davidson, P. M. & Lammerding, J. Broken nuclei - lamins, nuclear mechanics, and disease. *Trends Cell Biol.* **24**, 247–256 (2013).

80. Vergnes, L., Peterfy, M., Bergo, M. O., Young, S. G. & Reue, K. Lamin B1 is required for mouse development and nuclear integrity. *Proc. Natl. Acad. Sci.* **101**, 10428–10433 (2004).

Chapter 2

LiMex – A Novel Concept for High-Magnification Imaging of Cells During Mechanical Stimulation Reveals Divergent Nuclear Behavior in Response to Low or High Magnitude Cyclic Stretch

ABSTRACT

Mechanical cues from the environment influence cell behavior. Mechanisms of cellular mechanosensation are unclear, partially due to a lack of methods that can reveal dynamic processes. Here, we present a new concept for a low-cost, magnetically-driven device that enables high-magnification imaging of cells during stretch. Using this device, we observed that nuclei of mouse embryonic skin fibroblasts underwent rapid but divergent responses to strain magnitude, showing area increase and chromatin decompaction during 5% strain, but area decrease and chromatin condensation during 20% strain. Only responses to low strain were dependent on calcium, while actin inhibition abrogated any nuclear response and increased stretch-induced DNA damage. Stretch-activation revealed a shift in actin filaments away from (5% strain) or towards (20% strain) the nuclear periphery. Our findings suggest that different pathways control strain level-dependent cell behavior and that mechanical confinement of nuclei through actin may be a protective mechanism during high strain loads.

2.1. INTRODUCTION

Mechanical cues from the environment are known to have a profound impact on cell fate[1] and cell behavior[2,3], a phenomena referred to as mechanosensation. Changes in mechanical properties due to trauma[4,5], chronic conditions[6–8], or genetic predispositions[9,10] lead to cellular degeneration and result in a range of pathologies[11]. Understanding the mechanisms involved in mechanosensation would help to work towards mitigating these conditions and allow researchers to direct cell differentiation to generate artificial tissues for drug testing[12] or organ repair[13].

The nucleus is thought to be an essential mechanosensitive organelle as it is tightly connected to all parts of the cytoskeleton through LINC (Linker of Nucleo- and Cytoskeleton) complexes[14,15]. Cyclic stretch has been shown to change nuclear morphology[16–18], induce chromatin condensation[17–19], increase mechanical resistance of nuclei[16,18,20] and alter gene expression[21,22]. Studies on isolated nuclei have demonstrated that the nucleus alone can respond to stretch, however, only when engaged via LINC complexes[20]. Disruption of LINC complexes have shown to inhibit stretch-induced changes in chromatin remodeling[23–25] and gene expression[21,22], suggesting that strain transfer from the cytoskeleton plays an important role for nuclear mechanosensation. The actin skeleton, in particular, has been shown to be crucial for nuclear responses to dynamic mechanical stimulation[18,21,23,26]. Despite these findings, the underlying mechanisms of cellular and nuclear mechanosensation pathways are mostly unclear, partially due to a lack of accessible methods to image cell behavior under mechanical stimulation in real time.

Nuclear responses to mechanical stimulation have been shown to be very rapid (seconds)[17,21] highlighting the importance of simultaneous stimulation and data acquisition to understand these processes. However, conventional and commercially available cell stretch devices (e.g. Flexcell) do not allow for the use of high magnification objectives necessary to

elucidate single cell behavior[27]. Custom-built devices designed by research groups either lack high-resolution live imaging capability[28,29] or use expensive components such as precise linear actuators[30–32] or optical traps.[33] In addition, designs are often complicated and require special expertise, which overall makes them difficult to replicate for widespread use.

Here we propose the design of a low-cost LiMex (Live-imaging, Magnetically-enabled Cell Stretcher) device that uses electromagnetic force to apply a precise equiaxial stretch to a thin silicone membrane suspended over a water-immersion objective (**Figure 2.1a**, **Extended Figure 2.1**). Using electromagnetic force is an advantage because it can be precisely controlled without requiring special components, in our case only needing an electromagnetic coil made in-house and a permanent rare earth magnet. Most of the device parts were 3D printed making the system easy to replicate at a low cost. Only one part, a tapered circular ring that interfaces with the silicone membrane, was machined due to low-friction requirements. The remaining parts (rare earth magnet, linear rails with carriages and electronics for control) were generally inexpensive and readily available (**Extended Table 2.1**). Using the LiMex device, we investigated the dynamic response of nuclei from mouse embryonic skin fibroblasts when exposed to cyclic stretch. Our experiments verified that nuclei respond rapidly to mechanical stimulation. Interestingly, we observed contrasting behavior for cells during low or high strain regiments, as we observed nuclear area shrinkage and chromatin condensation in response to high strain, but nuclear area expansion and chromatin decompaction in response to low strain. This dichotomous behavior appeared to be mediated through different pathways as only responses to low strain cyclic stretch were dependent on calcium signaling while the actin skeleton was necessary for any strain response. Imaging of actin dynamics during cyclic stretch revealed a divergent behavior similar to that of nuclei with actin filaments shifting from the cell border to towards the nuclear periphery during high strain

loads and vice versa for low strain. Moreover, actin depolymerization lead to an increase in DNA damage with increasing levels of strain, suggesting that F-actin-dependent nuclear shrinkage might serve as a protective mechanism during high strain loads.

2.2. RESULTS

2.2.1. Cell Stretch Device – Concept and Calibration

To record the dynamic responses of single cells at high magnification during mechanical stimulation, we built a system in which a thin (~127 μm) silicone membrane is stretched over a deformation ring that is fixed in place over a microscope objective (**Figure 2.1a, Extended Figure 2.1a**). The static deformation ring enabled a relatively constant imaging plane in *x*, *y* and *z*-directions while the membrane was stretched around the ring. The silicone membrane was assembled into a stretch chamber (**Extended Figure 2.1b)** and fused to a compliant silicone containment well to allow the culturing of cells. The stretch chamber, in turn, could be engaged into a piston that could move freely up and down in an electromagnetic coil via sliders. The piston contained a strong rare earth magnet at the top to transfer force from the electromagnet below. When current was applied to the coil, the resulting electromagnetic field lifted the piston up or pushed it down depending on the orientation of the magnetic field. The electromagnetic field, in turn, was controlled through an Arduino microprocessor that modulated intensity and the direction of current from a constant DC power source (**Extended Figure 2.2a**). To confirm the precision of the control system and movement of the device, a laser displacement sensor was used to show that the electromagnetic field could be used to precisely (**Figure 2.1b**) and repeatedly (**Figure 2.1c**) control the position of the piston and, therefore, the indentation of the membrane.

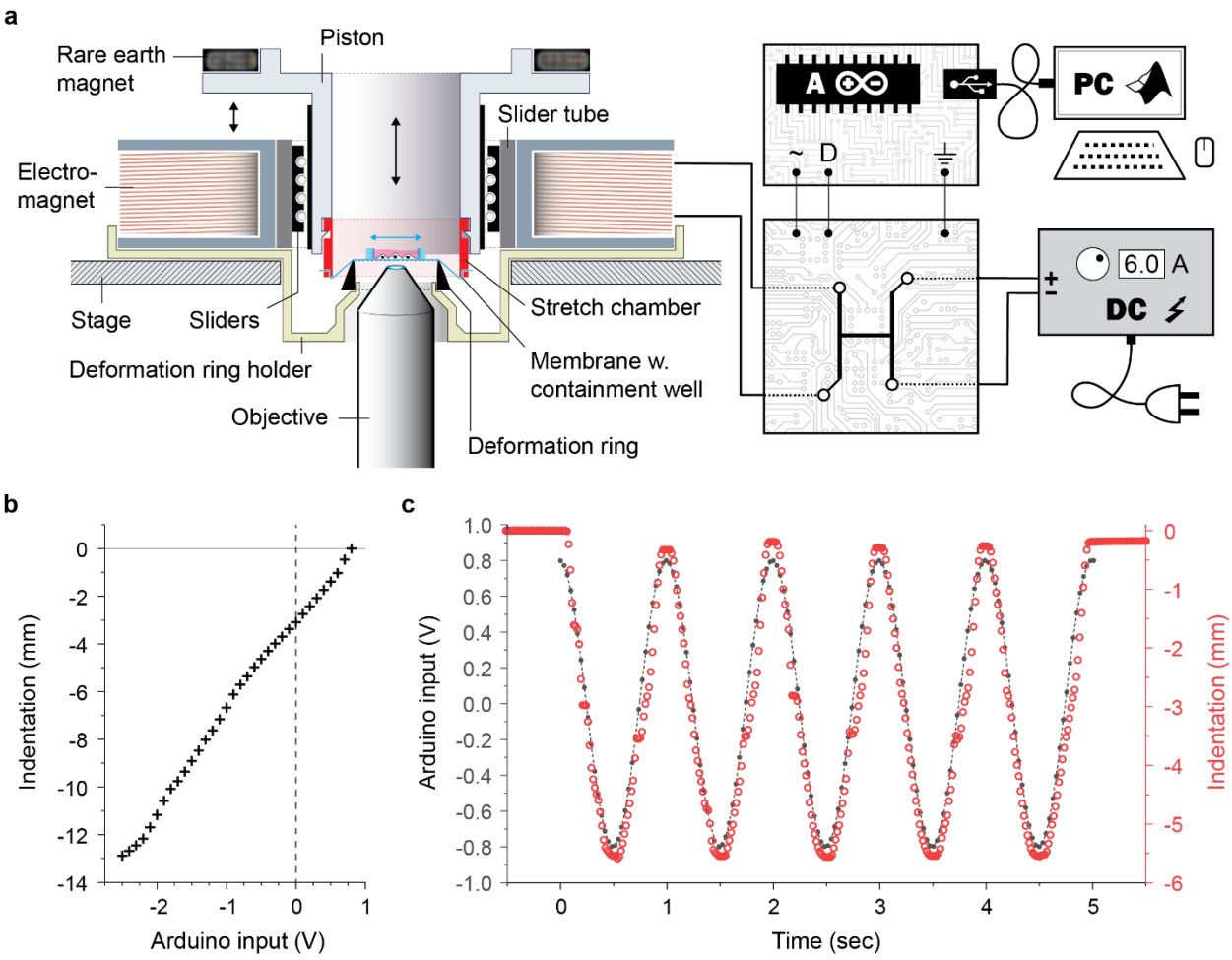

Figure 2.1. LiMex device allows for precise and repeatable membrane stretch via electromagnetic force. a) A cross-sectional illustration of the stretch device and its control circuit is shown. A suspended piston containing a permanent magnet moves vertically through an electromagnetic coil. Downward motion of the piston stretches a silicon membrane over a deformation ring which holds the stretched membrane at a constant distance over a microscope objective. See Extended Figure 3.1b for real images of the device. To control the electromagnet, an H-bridge is used to modulate intensity and direction of a constant current (6 A) from a DC power source through low voltage signals using an Arduino microprocessor. On the Arduino, a PWM pin (~, power-wave-modulation, 0-5 V) is used to control the intensity and a digital pin (D, 0/1) is used to control the direction of the current. A USB interface enables control of the Arduino inputs via MATLAB. **b)** A distance measurement laser was used to investigate piston movement, and thereby membrane indentation, in response to electromagnetic force as represented by Arduino input voltages. Electromagnetic force could be used for the precise membrane stretch. **c)** A sigmoidal function was programmed in MATLAB to generate Arduino inputs from +0.8 to -0.8 V at a frequency of 1 Hz and piston indentation was recorded over 5 cycles. Electromagnetic force could be used for precise and repeatable membrane indentation.

To calibrate the LiMex device, membranes were coated with fluorescent beads. During membrane stretch, bead displacements were recorded on a microscope to calculate the resulting strain using traction force microscopy[34] (**Figure 2.2a**). Since the piston has a weight that stretches the membrane in the absence of a magnetic field, the baseline Arduino input voltage that produced an electromagnetic field to keep the piston suspended without indenting the membrane was determined to be +0.8 V (**Extended Figure 2.2b**). For calibration, we recorded bead displacements in response to different Arduino inputs from +0.8 to -3.25 V. The resulting current vs. strain calibration curve fit best to a 3rd-order polynomial function due to a mild inflection around 0 V; however, a 2nd-order polynomial function fit almost equally well and was chosen for simplicity (**Figure 2.2b**). Plotting of membrane indentation vs. strain from associated Arduino inputs showed a linear relationship as would be expected from a linear elastic material such as silicone (**Figure 2.2c**). Analysis of repeated membrane stretch from +0.8 to -0.9 V, corresponding to 10% strain, showed reliable strain application within 0.5% with no indication of declining or increasing trends within 11 repeats (**Figure 2.2d**). Next, we performed live cell imaging of cells during cyclic stretch routines to validate the utility of our device.

2.2.2. Nuclei of MSF Show Dichotomous Responses to Low and High Strain Levels

To test the device, we investigated the dynamic behavior of cell nuclei from mouse embryonic skin fibroblasts (MSF) from H2b-eGFP harboring mice in response to equiaxial stretch. For that, MSFs were seeded onto fibronectin-coated stretch chambers and mechanically stimulated for 30 min with a sigmoidal stretch routine (1 Hz) with peak strains of 5%, 10% or 20%. The stretch routine was followed by 30 min of no stimulation (rest) to determine reversibility of any

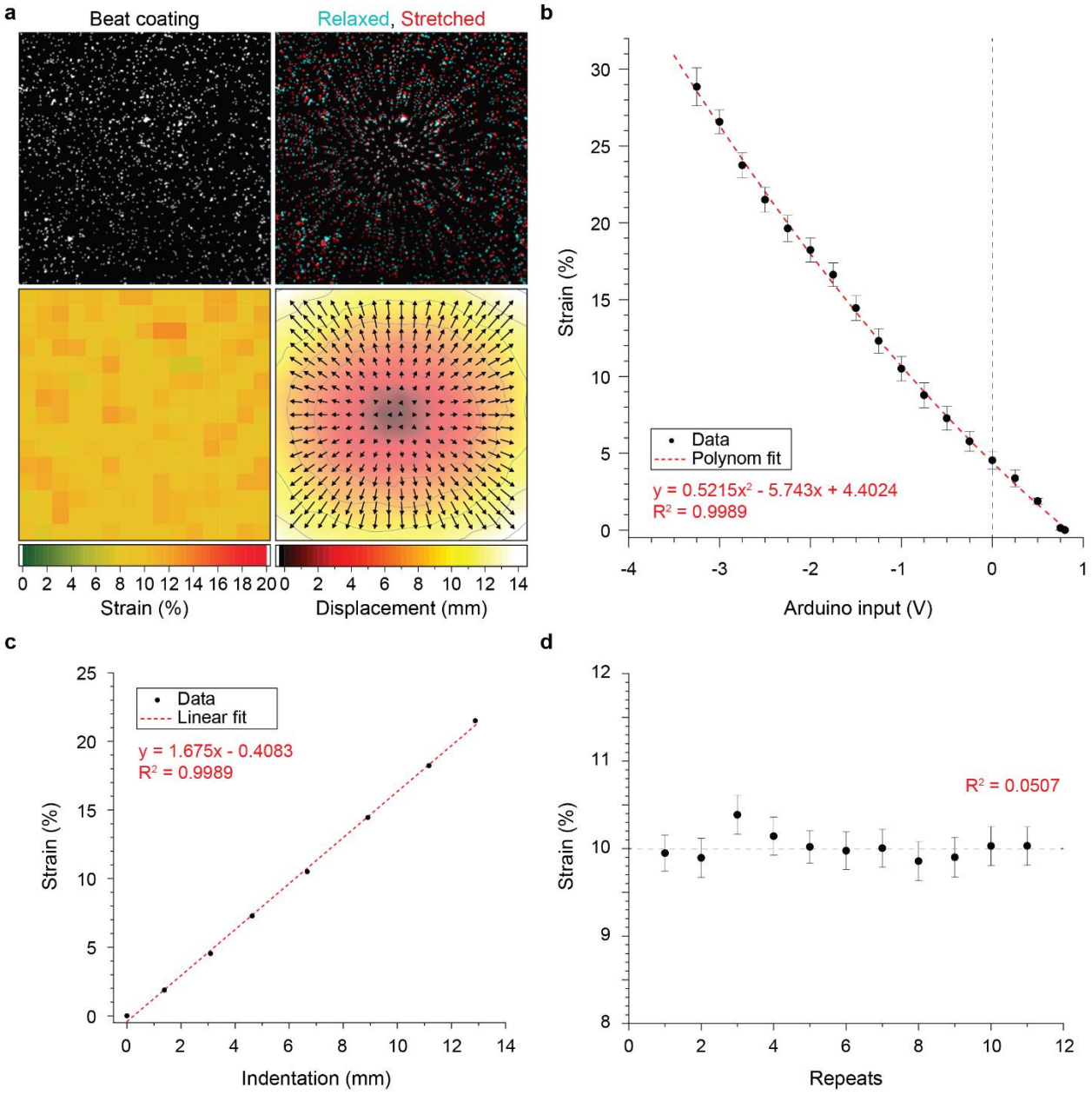

Figure 2.2. LiMex device calibration and performance using particle tracking. Membrane containment wells were coated with 2 µm sized fluorescent beads. Images were acquired at baseline (relaxed, Arduino input=+0.8 V, see Extended Figure 2.2b) and during stretch to calculate membrane strain from bead displacements, using particle tracking, in response to different Arduino input voltages. **a**) Example of recorded bead displacements and resulting strain map for an Arduino input of -0.9 V. **b)** Calibration curve as determined through bead displacements. The acquired data fit a 2nd-order polynomial function; SD; n=3. **c**) Plotting calculated membrane strains over measured membrane indentations from Figure 2.1b showed a linear relationship. **d**) Measurements of consecutive membrane indentation for an Arduino input of -0.9 V showed repeatable application of strain within 0.5%.

observed responses. In addition to unstretched control cells (0%), cells were also subjected to a magnetic field corresponding to the 20% stretch routine (MAG) under static conditions (no stretch) to assess effects of the magnetic field alone. Image stacks of nuclei were acquired via H2b-eGFP (**Figure 2.3a**). Unstretched control cells (0%) showed a continuous but slight decline in nuclear area during the 1 h experiment (**Figure 2.3b**). In contrast, area of nuclei decreased rapidly (< 2 min) in response to high strains of 20%, continued decreasing during the 30 min of stretch and increased again during the 30 min rest period. Nuclei subjected to 10% cyclic strain also showed a decrease in area but to a lesser extent and more delayed compared to the 20% strain routine. Surprisingly, at 5% strain, nuclear area increased during stretch and stayed elevated during rest compared to control cells.

Changes in skewness and kurtosis of chromatin intensity histograms could further be used to analyze chromatin condensation as indicated by a shift towards higher intensities (positive skewness) and narrowing of the histogram peak (positive kurtosis)[35]. Similar to nuclear area, H2b histograms of MSF nuclei subjected to 20% cyclic strain showed a rapid increase in both skewness and kurtosis during the stretch interval, followed by a mild decline during the rest period. Nuclei subjected to 5% cyclic strain showed a decrease in skewness and kurtosis during the stretch and rest period (**Figure 2.3c**). Changes in nuclear area as well as H2b histogram skewness and kurtosis of MSFs subjected to the magnetic field alone (MAG) closely matched that of unstretched control cells (0%) in absence of a magnetic field, suggesting that the magnetic field had no influence on the observed cell behavior.

To test whether chromatin dyes are suitable to investigate mechanosensitive behavior of nuclei, MSFs were subjected to a 20% strain routine after staining with Hoechst (**Extended Figure 2.3**). Stained nuclei showed a similar dynamic of area decline during stretch, but no

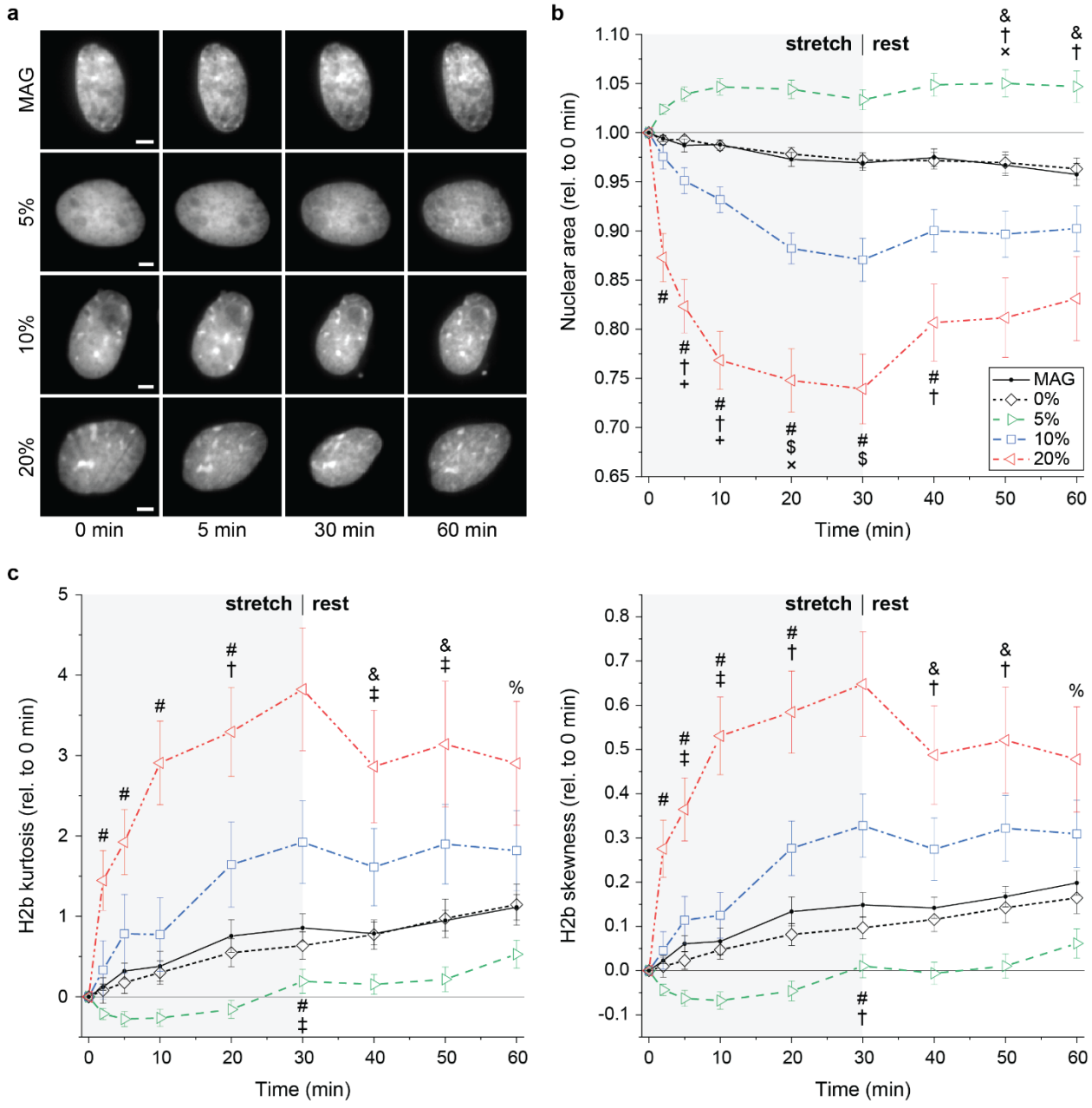

Figure 2.3. MSF nuclei show opposing changes in nuclear area and chromatin condensation during low strain and high strain cyclic stretch. Mouse embryonic skin fibroblasts were exposed to 30 min of sigmoidal stretch with peak strains of 0%, 5%, 10% or 20%, followed by 30 min of no stimulation (rest), during which image stacks of nuclei were recorded. Control cells were exposed to the magnetic field alone without stretch (MAG). **a)** Images of nuclei recorded via H2b-eGFP; scales=5 µm. **b)** Relative changes in nuclear area (relative to 0 min) during stretch routines. Nuclear areas decreased in response to high strains (10%, 20%), but increased for low strain (5%), while exposure to the magnetic field alone (MAG) showed no difference compared to unstretched cells (0%). **c)** Difference in H2b

histogram kurtosis and skewness (compared to 0 min) during stretch routines. Kurtosis and skewness increased under high strain routines (10%, 20%) while they decreased for low strain (5%), indicating elevated or subsided chromatin condensation, respectively; SEM; n>24 from 4 exp.; ANOVA: # ($p<0.01$) for 20% vs. all, $ ($p<0.01$) for 10% vs. all, † ($p<0.01$) or ‡ ($p<0.05$) for 5% vs. 10%, & ($p<0.01$) or % ($p<0.05$) for 20% vs. MAG, 0% and 5%, + ($p<0.05$) for 5% vs. MAG, × ($p<0.05$) for 5% vs. MAG and 0%.

recovery during the rest period, compared to unstained nuclei. Additionally, measures of chromatin condensation were reduced during stretch, overall suggesting that the use of chromatin dyes can alter nuclear responses to stretch. In summary, these results showed that the nuclei of MSFs do not respond proportionally to increasing levels of strain as we observed a decrease in nuclear area and increased chromatin condensation for high strains in contrast to an increase in nuclear area and decrease in chromatin condensation for low strains. Depending on the strain level, responses occurred rapidly after starting the application of strain, which emphasizes the need for live imaging capabilities to capture these effects.

2.2.3. Nuclear Responses of MSFs to Low, but Not High Cyclic Strain, are Sensitive to Calcium While Actin is Essential for Both

We observed a dichotomous change in nuclear area and chromatin condensation of MSF nuclei in response to high and low cyclic strain. Next, we wanted to investigate whether there was a difference in signaling between low and high strain stimulation. It has been shown that chromatin condensation in response to uniaxial cyclic stretch is abrogated after inhibition of calcium signaling[17]. Treatment of MSFs with BAPTA (BP), to sequester extracellular calcium, or KN-62 (KN), to inhibit intracellular calmodulin signaling, abrogated the increase in nuclear area and decrease in chromatin condensation observed for non-treated (NT) and vehicle control cells (VH) during 5% cyclic strain routines (**Figure 2.4**). Conversely, calcium inhibition only minorly

effected the decrease in nuclear area and increase in chromatin condensation during 20% cyclic strain routines. Interestingly, both BAPTA and KN-62 treatments interfered with the slight decrease in nuclear area and increase in chromatin condensation observed during static magnetic field-only routines (MAG).

Further, the actin skeleton has been shown to be crucial for mechanosensitive signaling and is thought to be an important structure for forwarding mechanical cues to the nucleus[18,21–23,26]. Treatment of MSFs with the actin depolymerization drug cytochalasin D (cyto D, CD) resulted in a similar abrogation of nuclear area increase in response to 5% cyclic strain but showed more elevated chromatin condensation compared to calcium inhibition (**Figure 2.4**). Interestingly, cyto D treatment completely prevented nuclear shrinkage during 20% strain routines and nuclei showed even less chromatin condensation compared to 5%. In contrast to calcium inhibition, cyto D treated MSF nuclei showed no difference during static magnetic field-only routines compared to non-treated and vehicle control cells. Together, this data suggested that calcium signaling plays a role during low strain, but not high strain stimulation, while an intact actin skeleton was crucial for nuclear responses to any magnitude of stretch.

2.2.4. Actin Depolymerization Increases DNA Damage After Low and High Cyclic Strain

The calcium-independent shrinkage of nuclear areas suggested that there is a different mechanism for cell behavior under high strain compared to low strain loading. Cyclic stretch has been shown to cause DNA damage[36,37]. To test whether actin-mediated nuclear shrinkage under high strain loads might be an protective mechanism to prevent DNA damage, we stained MSFs for serine-139 phosphorylation of γH2a.x (p-γH2a.x), an indicator of DNA double strand breaks[38] and filamentous actin (F-actin) after 30 min of cyclic stretch. F-actin intensities above the nucleus (perinuclear F-actin) increased with strain magnitudes, being only slightly higher after 5% and

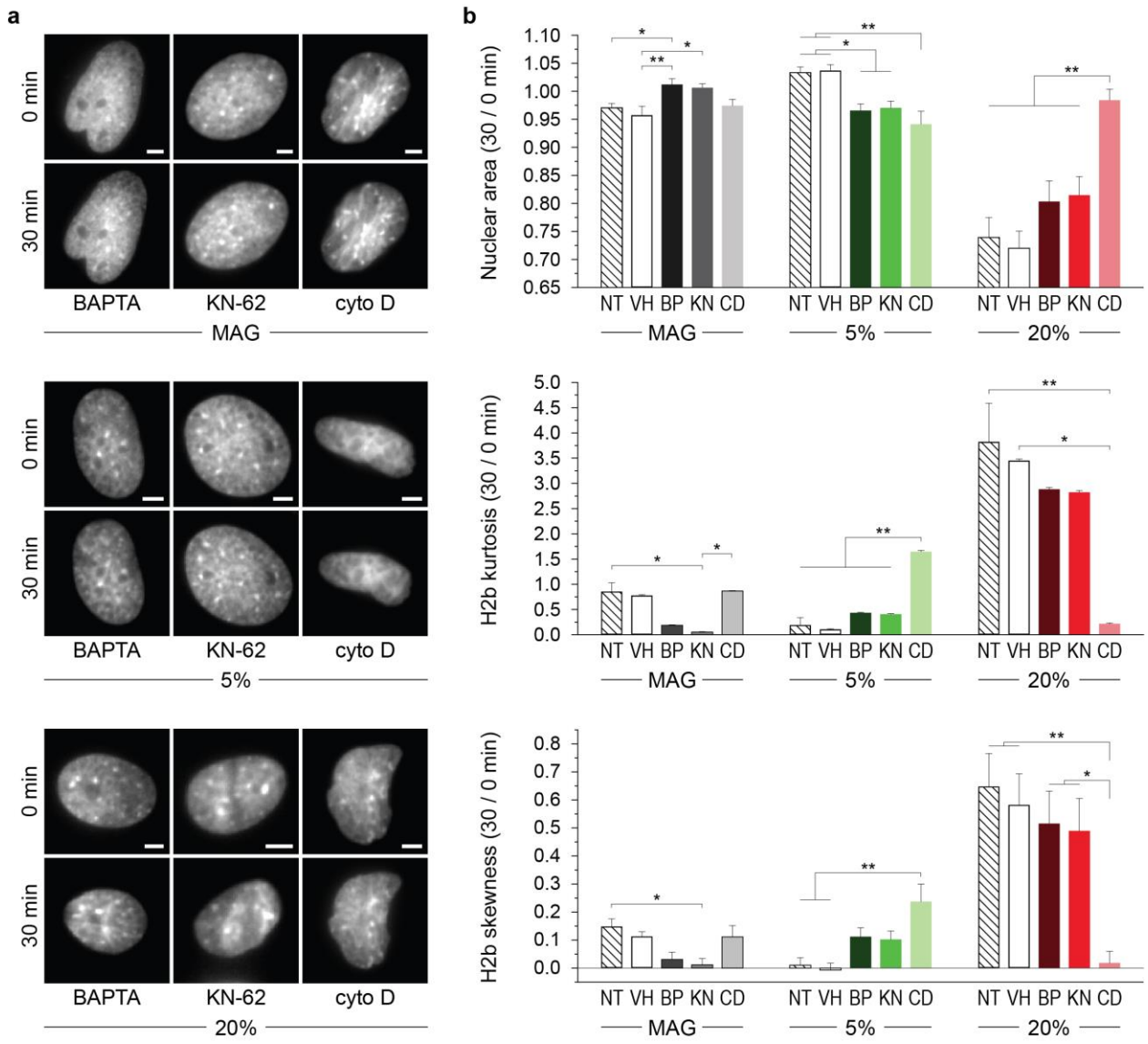

Figure 2.4. The actin skeleton, but not calcium signaling, is required for nuclear responses to high strain cyclic stretch. Mouse embryonic skin fibroblasts were treated with BAPTA, KN-62 or cyto D before being exposed to 30 min of sigmoidal stretch with peak strains of 5% or 20%, or 0% under the influence of the magnetic field alone (MAG), during which image stacks of nuclei were recorded. **a)** Images of nuclei recorded via H2b-eGFP before (0 min) or after (30 min) cyclic stretch routines; scales=5 µm. **b)** Cyto D treatment (CD) inhibited changes in nuclear area and chromatin condensation in response to 5% and 20% cyclic stretch compared to non-treated (NT) or vehicle (VH) control cells. BAPTA (BP) or KN-62 (KN) treatment abrogated the increase in nuclear area and decrease in chromatin condensation after 5% cyclic stretch but had no effect after 20% cyclic stretch; NT control same as Figure 2.3; SEM; n≥15 from 3 exp.; ANOVA: * $p<0.05$, ** $p<0.01$.

twice as high after 20% cyclic strain compared to unstretched (0%) and magnetic field-only control cells (MAG, **Figure 2.5a-b**). The number of p-γH2a.x foci per nucleus also increased with increasing levels of strain. Surprisingly, DNA damage was higher under static conditions (0%, MAG) compared to 5% and showed a similar extent of damage as after 20% cyclic stretch.

Similar to nuclear responses in area and chromatin condensation, inhibition of calcium signaling via BAPTA or KN-62 treatment abrogated the increase in perinuclear F-actin intensities after 5% cyclic stretch, but not after 20% cyclic stretch, compared to non-treated (NT) or vehicle (VH) control cells (**Figure 2.5c-d, Extended Figure 2.4a**). Interestingly, inhibition of calcium signaling increased DNA damage only in static magnetic-field routines but showed no difference for cells after 5% or 20% cyclic stretch. In contrast, actin depolymerization via cyto D treatment distinctly increased the number of p-γH2a.x foci per nucleus after 5% and 20% stretch routines but had no effect on cells exposed to magnetic-field only routines. Cyto D treatment also showed no effect on perinuclear F-actin intensities after magnetic field-only routines. However, while the observed increase in F-actin intensities after 20% cyclic stretch was abrogated in cyto D treated MSFs (as would be expected after actin depolymerization), F-actin intensities were increased after 5% cyclic stretch, likely due to an accumulation of small actin filaments at the nuclear periphery (**Extended Figure 2.4a**). Imaging of nuclei in a relaxed or stretch condition after 30 min of 20% cyclic strain showed that nuclear strain transfer was higher in cyto D treated cells compared to non-treated cells (**Extended Figure 2.4b**). Overall, this data showed that perinuclear F-actin increased with increasing levels of strain and actin depolymerization resulted in elevated occurrences of double strand breaks during high and low cyclic stretch, suggesting that the actin skeleton might play a protective role for the nucleus during high strain loads.

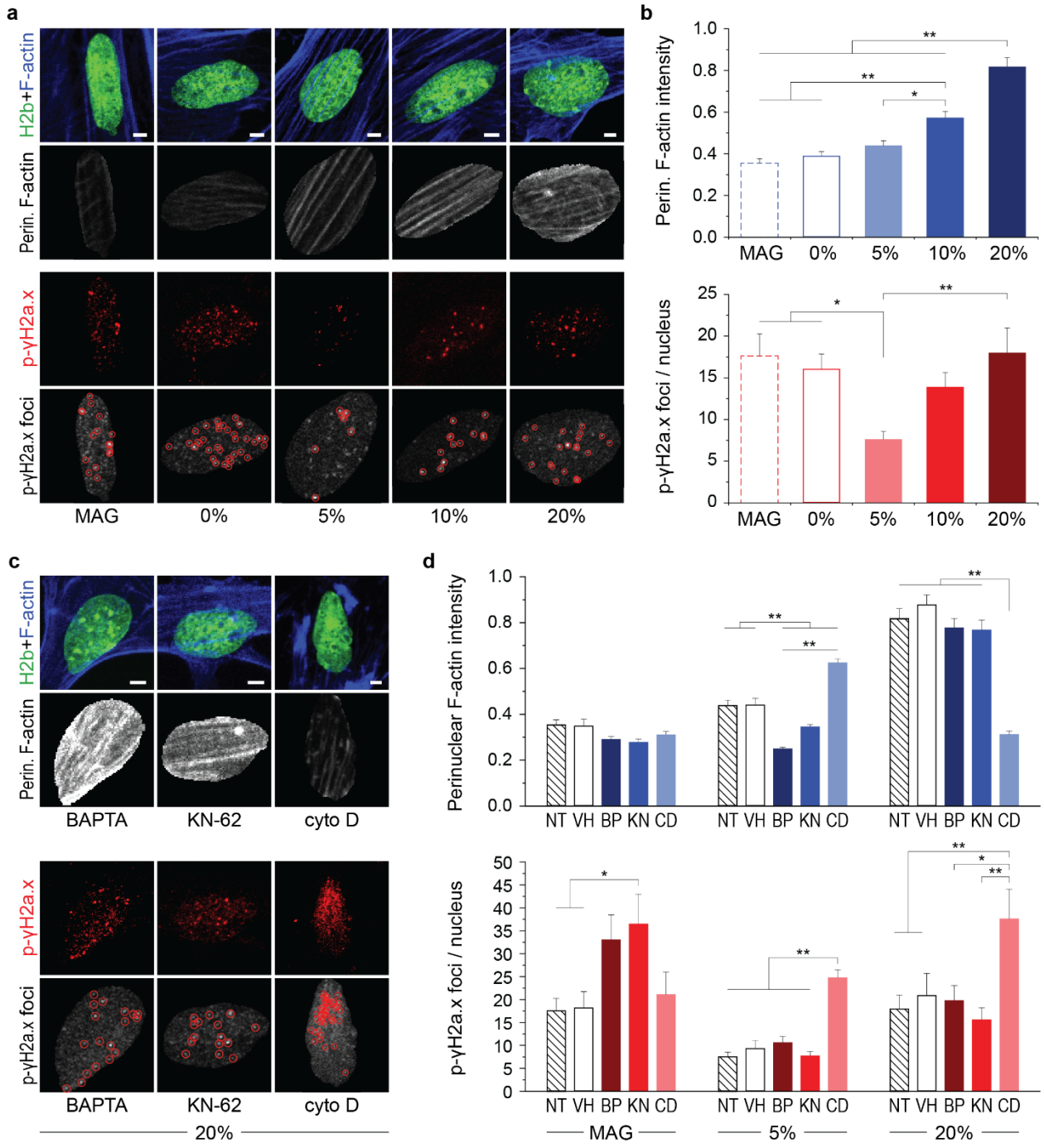

Figure 2.5. Perinuclear F-actin increases with strain magnitude, and actin depolymerization leads to increased DNA damage after low and high strain cyclic stretch. Mouse embryonic skin fibroblasts were exposed to 30 min sigmoidal stretch routines with peak strains of 0%, 5% or 20%, or under the influence of the magnetic field alone (MAG), after which cells were stained for γH2a.x phosphorylation (p-γH2a.x), as an indicator of DNA double strand breaks, and F-actin. **a)** Stained images of nuclei after stretch routines. A custom

MATLAB code was used to analyze perinuclear F-actin intensities, using H2b-eGFP as a mask, and to identify p-γH2a.x foci as indicated by red circles. **b)** Perinuclear F-actin intensities and number of p-γH2a.x foci increased with strain magnitude; however, highest levels of DNA damage were observed for static control cells. **c, d)** MSFs were treated with BAPTA (BP), KN-62 (KN) or cyto D (CD) prior to stretch routines. Inhibition of calcium signaling via BAPTA and KN-62 treatment abrogated increases in perinuclear F-actin intensities in response to 5%, but not 20%, cyclic stretch. Actin depolymerization altered F-actin intensities and showed increased number of p-γH2a.x foci after both 5% and 20% cyclic stretch, while DNA damage was only increased for static magnetic-field only control cells after inhibition of calcium signaling; see Extended Figure 2.4a for MAG and 5% images; SEM; n≥150 from 3 exp.; ANOVA: * $p<0.05$, ** $p<0.01$; all scales=5 μm.

2.2.5. Live Imaging of Actin Dynamics Revealed Opposing Patterns of Reorganization During Low and High Cyclic Strain

Inhibition of actin polymerization abrogated nuclear responses to high and low strain routines, and increased DNA damage with increasing levels of strain. To further investigate the role of actin skeleton during stretch-induced changes in cell behavior, we transfected MSFs with a fluorescent F-actin probe (mRuby-Lifeact-7) and acquired image stacks of F-actin during 30 min of 5% or 20% cyclic stretch followed by 30 min of rest. Analysis of 2 μm thick profile line projections along the minor axis (perpendicular to F-actin filaments) of two example cells suggested that Lifeact intensities shifted towards the cell border after 30 min of 5% stretch, while they shifted towards the nucleus after 20% (**Figure 2.6a-b**). To verify these findings in multiple cells (n=6), profile line projections were grouped into bins along their relative distance to the nuclear center, with bins 1-5 representing Lifeact intensities from the nuclear center to the nuclear periphery and bins 6-10 representing intensities from the cytoplasmic site of the nuclear border to the cells border. After 30 min of cyclic stretch, Lifeact intensities were elevated above the nuclear interior (bin 1-4) in cells exposed to both low (5%) and high (20%) levels of strain (**Figure 2.6c**).

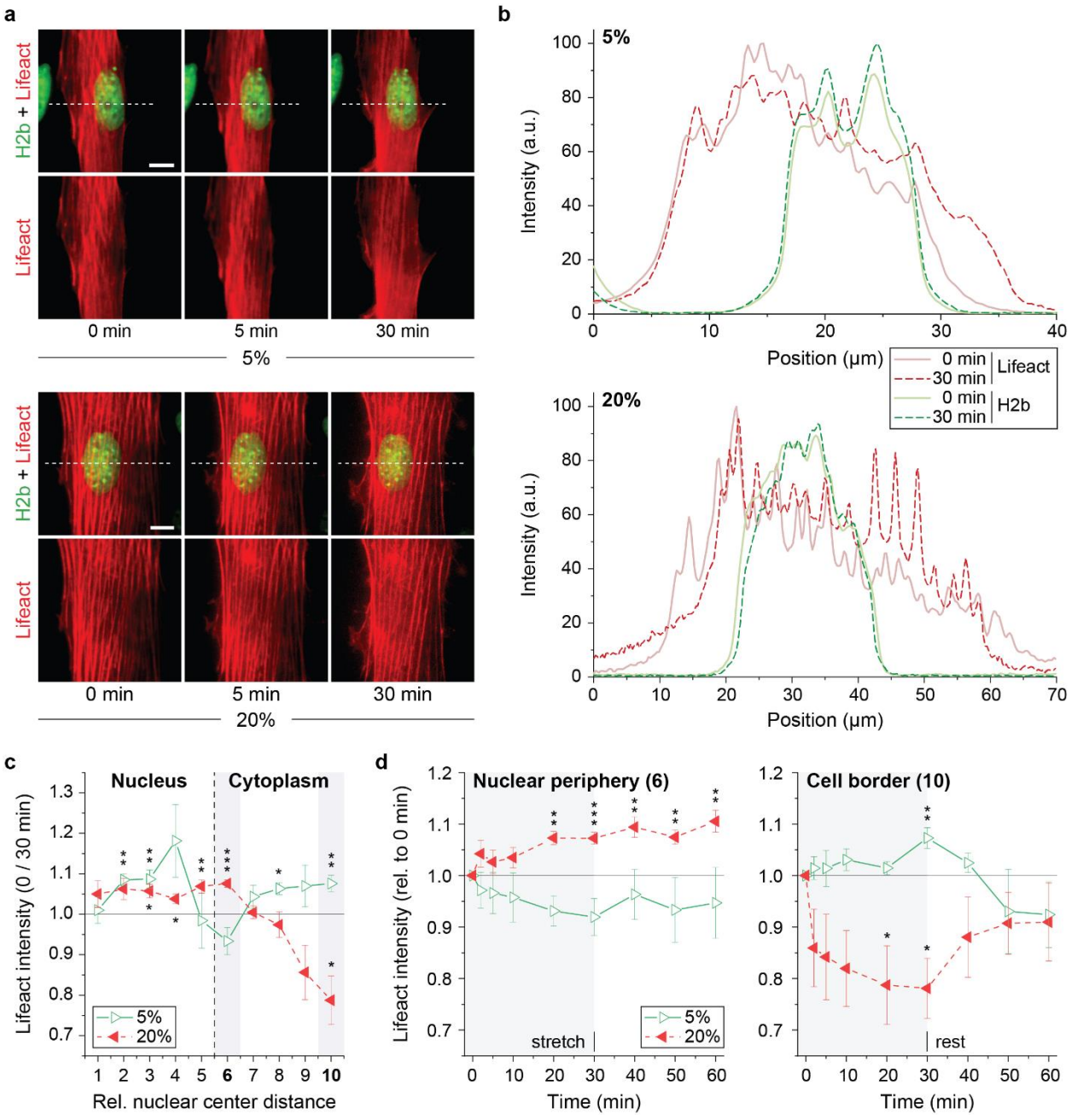

Figure 2.6. Lifeact imaging reveals opposing changes of actin reorganization at the cell and nuclear border during low strain and high strain cyclic stretch. Mouse embryonic skin fibroblasts were transfected with mRuby-Lifeact-7. The day after, cells were exposed to 30 min of 5% or 20% sigmoidal stretch, followed by 30 min of no stimulation (rest), during which image stacks were recorded. **a)** Images of actin (Lifeact) or nuclei (H2b) recorded during the stretch routine. White doted lines represent the center location of profile lines in (b); scales=10 µm. **b)** Projections of actin (Lifeact) and nuclear (H2b) profile lines, as indicated in (a), of two example cells before (0 min) or after (30 min) exposure to either 5% or 20% cyclic

stretch. **c)** Changes in Lifeact intensities after 30 min of stretch were binned into relative location to compare changes in different cells: Bins 1-5 represent intensities from the nuclear center to the inner nuclear border and 6-10 from the nuclear periphery to the cell border. Lifeact intensities shifted from the cell border to the nuclear periphery after 20% cyclic stretch while this trend was inversed after 5% cyclic stretch; SEM; n=6; T-test (vs. 0 min): * $p<0.05$, ** $p<0.01$, *** $p<0.001$. **d)** Changes in Lifeact intensities at the nuclear periphery (bin 6) and cell border (bin 10) over time. Actin reorganization shows dynamics similar to that of nuclear responses; SEM; n=6; T-test (vs. 0 min): * $p<0.05$, ** $p<0.01$, *** $p<0.001$.

However, Lifeact intensities were decreased at the nuclear border (bin 6) and increased towards the cell border (bin 10) in cells after 5% of cyclic stretch, while intensities were increased at the nuclear border and decreased at the cell border after 20% of cyclic stretch.

Analysis of Lifeact intensities over time showed a steady decrease or incline of intensities at the nuclear border during the 30 min of stretch in response to low or high strain routines, respectively (**Figure 2.6c**). Intensities stayed declined or elevated during rest at the nuclear border. At the cell border, Lifeact intensities declined rapidly in response to 20% strain, continued decreasing during the stretch period and raised again during the 30 min of rest, albeit staying lower compared to 0 min. This change in Lifeact intensity was noticeably similar to the dynamics of nuclear area shrinkage after high strain cyclic stretch, suggesting that F-actin rearrangement might mediate the nuclear response through physical interaction. During 5% cyclic stretch, Lifeact intensities slowly increased at the cell border and declined to reduced levels of intensity, compared to 0 min, during rest. Moreover, we observed one cell which showed actin filament disruption and strong nuclear collapse shortly after the start of a 20% routine (**Extended Figure 2.5**). These observations were more pronounces after the rest period, indicating that the cell died through either necrosis or apoptosis. This further supported the notion that high strain exposure can be a serious challenge to cellular survival. Together, these results showed that actin filaments reorganize at the

nuclear border and cell border with opposing patterns between low and high strain loads, and similar to nuclear responses.

2.3. DISCUSSION

In this study, we present a new device concept, called LiMex, to image cells at high magnification during mechanical stimulation. The device was constructed using mainly 3D printed parts and operated through electromagnetic force and. Using this device, we could apply precise and repeatable strain onto a thin silicone membrane. The aspect of 3D printing makes the device easy to replicate, but also enables the adjustment of the design to fit different microscope stages. Live cell experiments with mouse embryonic skin fibroblasts showed that nuclei had opposing responses to low strain or high strain cyclic stretch routines, as they showed chromatin decondensation and nuclear area increase during low strain, and chromatin condensation and nuclear area decrease during high strain application. Previous studies have shown that cyclic uniaxial stretch (3-15%) induces chromatin condensation and nuclear elongation in the direction of stretch in mesenchymal stem cells (MSC)[17,18]. Another study found that cyclic force application using a magnetic needle resulted in chromatin decondensation[23]. Both groups reported changes in chromatin compaction to be very rapid (second scale) upon stimulation, similar to our findings here. However, to our knowledge, no study has reported dichotomous mechanosensitive behavior of nuclei. Pioneering studies in mechanosensation have shown that MSC differentiate in accordance with the stiffness of their environment[1] (becoming osteogenic on stiff, myogenic on medium, and neurogenic on soft substrates) which indicated that cells differentiate between intensities of mechanical cues. Still, the underlying mechanosensitive mechanisms, and whether differences in strain magnitudes are processed through either one pathway in a dose-response

manner or are the result of different pathways interacting, is not clear. Here we showed that nuclear responses to low strain cyclic stretch were dependent on calcium signaling, while high strain responses were not, which provided evidence that different pathways are involved in strain magnitude processing.

2.3.1. Role and Mechanism of Divergent Nuclear Responses

Based on our observation of divergent nuclear responses, it is reasonable to assume that certain ranges of strain magnitudes might represent different modes of operation that are associated with specific challenges for the cell. For example, low strain cyclic stretch might mimic baseline physical activity while high strain cyclic stretch might be associated with extreme activity or trauma. Increased mechanical stress been shown to cause DNA damage[36,37] and trigger apoptosis[19,37]. The observed rapid nuclear contraction during high strain loads might therefore be a mechanism to protect from strain-induced DNA damage. In this study, we also observed an increase of DNA double strand breaks with increased levels of strains. Interestingly, the number of double strand break foci was as high in unstretched control cells as after high levels (20%) of cyclic stretch, suggesting that skin fibroblasts cells perform better under dynamic compared to static conditions. It is likely that skin fibroblasts, and other types of cells, have an optimal performance under low mechanical stimulation since that reflects the conditions they evolved in inside motile organisms. This might have grave implication considering that close to all cell are cultured on rigid static plastic or glass and more work needs to be done to validate and understand this phenomenon.

We further observed that the actin skeleton was essential for any nuclear response to stretch. Other studies have reported that stretch induced changes in chromatin organization[18,23,26] or gene expression[21,22] were abrogated after disruption of the actin skeleton. One particular study

found that the nuclear shape is controlled by a perinuclear actin cap above and around the nucleus[39]. In this study, we observed that perinuclear F-actin increased monotonically with strain magnitude and would therefore not explain the divergent nuclear response observed for different strains. However, closer investigation of dynamic F-actin reorganization in live cells showed that F-actin shifted away from the nuclear periphery to the cell border during low strain cyclic stretch and vice versa during high strain cyclic stretch. The dynamic change in actin reorganization was also rapid, particularly during high strain routines, and resembled that of nuclear responses. Together, this suggested that changes in nuclear area might be mediated by physical interactions with the actin skeleton. It would be interesting to further investigate whether changes in chromatin compaction are a passive result due nuclear area change or if they are mediated through the interaction actin filaments with the nucleus, e.g. through the LINC complex.

The occurrence of double strand breaks was increased during stretch after actin skeleton disruption. Hence, mechanical confinement of the nucleus through F-actin encapsulation might present a main mechanism to protect DNA during high strains loads by reducing the transfer of strain into the nucleus. We also observed that, after cyclic strain routines, strain transferred from the membrane to the nucleus was higher in cells treated with the actin depolymerizing drug, cyto D, which further supported this hypothesis. However, nuclear strain transfer prior to cyclic strain application could not be accurately assessed due to the rapid decline in nuclear area of cells held in a stretched position (see methods for details). Therefore, the question whether actin reorganization towards the nuclear periphery reduces nuclear strain transfer remains open.

2.3.2. Potential Influence of Magnetic Fields on Cell Behavior

A disadvantage of our LiMex device is the potential influence of magnetic fields, used to operate the device, on cell behavior. The rare earth magnet was positioned away from the

containment well at the opposite side of the piston and had a magnetic field strength of 7 mT at the location of the well (>5 cm from the pole). The distance of the magnet from the well changed only slightly (<1 cm) during stretch and can be considered static (±0.1 mT). In contrast, the electromagnetic coil produces an oscillating field during cyclic stretch with a maximum field strength of about 25.4 mT at the level of the membrane (**Extended Figure 2.6**) for 20% strain routines (1.0 mT for 5% and -9.3 mT at baseline). Studies showed that long-term exposure (1-5 days) to static 6 mT magnetic fields can have a significant but moderate effect on cell survival and cell morphology for some of the cell lines investigated[40,41]. Reviews on the effects of static magnetic fields concluded that effects on cell survival and proliferation were absent or minor regardless of the field strength used[42,43]. However, it should be noted that static magnetic fields can increase the effect of apoptosis-inducing drugs[40–43] which have been related to field-induced changes in calcium uptake[44,45]. This could also pose a possible explanation for the increase in DNA damage in BAPTA or KN-62 treated cells observed in this study. Investigation of the effect of oscillating electromagnetic fields (1-20 mT) showed moderate effects on cancer proliferation over the duration of 5 or 7 days[46,47]. These studies use 50 Hz oscillations, which are considered low frequency but are still distinctly higher than the 1 Hz used here. Research in chick embryos showed that oscillating fields influenced development only upwards of 16 Hz independent of the field strength used[48]. Overall, studies on static and oscillatory magnetic fields observed only minor changes in cell behavior after long time (days) exposure. In this study, we found no difference in nuclear responses between unstretched control cells exposed to magnetic field routines or cells in the absence of a magnetic field during the 1 h experimental routine. Special caution should be given for the use of pharmacological agents, especially when they negatively affect cell viability.

2.4. METHODS

2.4.1 LiMex Device Fabrication

Our custom-built device was designed to acquire high-magnification images of cells during the application of equiaxial strain while also avoiding the use of expensive materials (**Extended Table 2.1**) or complex designs. Two types of 3D printers were used to print a majority of the components: Objet30 (Computer Aided Technology) using the material VeroClear (OBJ-04055, Computer Aided Technology) and the uPrint SE Plus (311-20200, Computer Aided Technology, Inc) using ABS+. Designs for the device components were created as CAD files (**Extended Figure 2.1a)** using SolidWorks (Dassault Systèmes SolidWorks, v. 2018). All parts were printed at the Integrated Teaching and Learning Laboratory (ITLL) at the University of Colorado Boulder.

The main body consisted of four parts: a deformation ring holder, an electromagnet case, a slider tube and a piston (**Figure 1a**, **Extended Figure 1b**), which were printed using the uPrint SE Plus. The deformation ring holder was designed to fit into the circular notch of the manual stage of a Nikon Eclipse Ti Microscope (by interlocking with two metal wings that otherwise hold the aluminum sample tray) and contained an adapter that encased the microscope objective and held the deformation ring. Within the encasement, the objective had a moving range of approximately 8 mm in each direction. The deformation ring was machined from Delrin® Acetal Resin (8572K27, McMaster-Carr) to provide a friction-reduced interface with the silicone membrane. The slider tube fit tightly into the electromagnetic coil and contained 3 slider rails (NS-01-27, Igus) for friction-reduced vertical movement of the piston, which in turn contained 3 matching slider carriages (NW-02-27, Igus). A rare earth magnet (R3525, SuperMagnetMan) was attached to the top of the piston to transmit force from the electromagnet below.

The stretch chamber consisted of three parts: a main chamber, a membrane ring and holding clips (**Extended Figure 2.1c**), which were printed using the Objet30. The stretch chamber was assembled by placing a 60×60 mm silicon elastomer membrane (gloss 0.005", Specialty Manufacturing Inc.) straight onto the elevated inner edge of the main chamber, spanning and fixing the membrane with the membrane ring. The membrane ring was secured laterally with three holding clips. To culture cells, a compliant silicon containment ring was fused to the silicon membrane prior to assembly. Containment rings (d_{out}=16 mm, d_{in}=11 mm, h=5 mm, A_{in}=100 mm^2) were made from polydimethylsiloxane (PDMS, Sylgard®184, Dow Corning) using a 1:40 mixing ratio to produce soft rings with low mechanical resistance. Circular plastic molds were coated with 3,3,3-Trifluoropropyl-trichlorosilane (452807, Sigma) for 1 h under vacuum after which PDMS was poured into molds and cured over night at 80°C. The contact areas between the silicone membranes and the silicone containment rings were ozone-activated for 60 s via corona arc-discharge (BD-20, Electro-Technic Products Inc.) after which rings were pressed onto the membranes, weighted down with a 100g weigh to maintain close contact and incubated again overnight at 80°C to facilitate bonding. Bonded membranes were sterilized with 70% Ethanol, dried, and stretch chambers were assembled.

2.4.2. LiMex Device Control

To operate the stretch device, a simple control circuit was designed in which an Arduino microcontroller (DEV-13975, SparkFun Electronics) modulated the magnitude and direction of a constant 6 A current from a DC power source (9129B, BK Precision) to the coil via a H-bridge (RB-Cyt-132, RobotShop). Two signals from the Arduino to the H-bridge controlled the current flow: A PWM pin (power-wave-modulation) sending low voltage from 0-5 V controlled the current intensity (**Extended Figure 2.2a**) and a digital pin (either 0 or 1) controlled the direction

of the current to allow lifting of the piston in the relaxed state or attracting the piston downwards to intendent the engaged membrane. Arduino inputs were controlled via MATLAB (Mathworks, v. 2018b) via a USB interface and the Arduino Support from MATLAB package and a custom written code was used to operate the device.

2.4.3. LiMex Device Calibration

To measure piston movement and associated membrane indentation in response to electromagnetic fields, a laser distance sensor (Keyence LJ-G5001P) was pointed vertically at the top of the piston and changes in vertical movement were recorded via the Keyence LJ-Navigator software (Keyence, v. 1.7.0.0). Particle tracking[34] was used to determine the amount of strain applied to the membrane in response to electromagnetic fields. For strain measurements, containment wells were coated with 2 µm blue fluorescent beads (F8824, Life Technologies) and images were recorded before and after membrane indentation on an inverted epi-fluorescence microscope (Ti-Eclipse, Nikon) with a 60× water immersion objective (0.26 µm/pix) and an EMCCD camera (iXonEM+, Andor). Bead displacements were determined via the Particle Image Velocimetry (PIV) plugin on ImageJ (NIH, v. 1.50e) and strains were calculated from bead displacements using a custom written MATLAB code (Mathworks, v. 2018b). To determine to baseline Arduino input voltage to keep the piston floating over the deformation ring against its own weight, the piston was placed in a position in which the membrane would not touch the deformation ring and membrane strains during stepwise reduction of the magnetic field were determined. The baseline Arduino input voltage was determined as the input before distinct changes in membrane strain could be observed (**Extended Figure 2.2b**). Electromagnetic fields produced by the coil (**Extended Figure 2.6**) were modelled using COMSOLE (v. 5.2.0.166).

2.4.4. Mouse Embryonic Skin Fibroblast Isolation, Culture and Pharmacological Treatments

B6.Cg-Tg (HIST1H2BB/EGFP) 1Pa/J mice (Stock No: 006069) were obtained from Jackson Laboratory. All animal procedures were performed following Institutional Animal Care & Use Committee approval. Skin from embryonic mice was harvested 18.5 days post conception. Skin was minced, washed with HBSS and incubated in 35 mm dishes in shallow medium (~0.5 ml) to avoid floating of the tissue for four days during which fibroblasts extruded from the tissue. After four days, remaining tissue was removed (picked out with a pipette) and extruded cells in the dish were detached using TrypLE (Gibco) and expanded in culture for another two days before being seeded into stretch chambers for experiments. The inner well of assembled stretch chambers was ozone-activated for 30 s via corona arc-discharge (BD-20, Electro-Technic Products Inc.) and coated with 50 µg/ml bovine plasma fibronectin (F1141, Sigma) in a total volume of 250 µl overnight at 37°C. MSFs were seeded into stretch chambers at a density of 80,000 cells/cm^2 one day before experiments. MSF were extruded and cultured in DMEM (ATCC) containing 10% fetal bovine serum (Gibco), 1% penicillin-streptomycin (Gibco) and 25 mM HEPES (Gibco) at 37°C and 5% CO_2. To inhibit calcium signaling, MSFs were incubated with 50 µM BAPTA (A4926, Sigma) or 10 µM KN-62 (I2142, Sigma) 1 h prior to cyclic strain experiments. To disrupt actin polymerization, MSFs were incubated with 2 µM cytochalasin D (C8273, Sigma) 30 min prior to experiments. Vehicle controls were incubated with 0.001% DMSO (276855, Sigma) 1 h prior to experiments. To test the use of chromatin dyes, cells were stained with Hoechst (NucBlue™ Live ReadyProbes™, Life Technologies) 30 min prior to experiments.

2.4.5. Live Imaging and Analysis of Nuclear Behavior During Stretch Routines

The stretch device was mounted on an inverted epi-fluorescence microscope (Ti-Eclipse, Nikon) with a 60× water immersion objective (0.26 µm/pix) and an EMCCD camera (iXonEM+, Andor). Using MATLAB, a sigmoidal control signal (1 Hz) was sent to the Arduino controller,

resulting in a sigmoidal stretch routine of the membrane (**Figure 2.1c**), with peak strains set to 5% (-0.1 V), 10% (-0.9 V) and 20% (-2.25 V) as determined by the calibration curve. Cells were cyclically stretched for 30 min followed by 30 min of rest (no stretch but the baseline magnetic field keep the piston levitating at 0%) during which 2 µm z-stacks (0.5 µm steps) of nuclei were acquired. Unstretched control cells (0%) were seeded into stretch chambers but kept stationary on the microscope without any magnetic field applied. Unstretched magnetic control cells (MAG) were placed stationary inside the coil without the piston and a magnetic field corresponding to a 20% sigmoidal stretch routine was applied. A custom MATLAB code was written that tracked nuclear outlines and H2b histograms during an image series from which changes in nuclear area, H2b skewness and H2b kurtosis were calculated.

To analyze the amount of strain transferred from the membrane to the nucleus after cyclic stretch routines, image stacks of nuclei were acquired under relaxed or stretched conditions and bulk nuclear strain was calculated from the change in nuclear area using the same MATLAB script as above. Note: nuclear strain transfer could not be accurately analyzed prior to stretch routines due to the fast response in area decline. MATLAB code is available from the corresponding author upon request.

2.4.6. Perinuclear F-actin and p-γH2a.x Staining and Analysis

MSFs were fixed in 4% ice-cold PFA for 10min, permeabilized with 1% Triton-X100 in PBS for 15 min and blocked with 10%NGS, 1% BSA in 0.1% PBT (0.1% Tween-20 in PBS) for 60 min. Primary incubation of Phospho-Histone H2A.X Ser139 (Cell Signaling, 9718S) was performed at 4°C overnight in 0.1% PBT containing 1% BSA at 1:400. Secondary incubation of Goat anti-Rabbit IgG-AF546 (Life Technologies) was performed in primary incubation buffer for 45 min at 22°C at a dilution of 1:500. F-actin was counterstained with Phalloidin-CF405 (Biotium)

for 30 min at a dilution of 1:30. Staining was performed in containment wells. After staining, membranes were cut out of the containment well, using a circular punch, and mounted cell-side up onto #1.0 glass slides with ProLong™ Diamond Antifade Mountant (Life Technologies). Image stacks (5 µm, 1 µm step) of multiple nuclei in a 318×318 µm area were acquired on a Nikon A1R confocal microscope using a 40× oil immersion objective (0.31 µm/pix). A custom MATLAB code was written that identified nuclei and determined perinuclear F-actin intensities and p-γH2a.x foci in projected image stacks. To account for variations in staining and imaging (same imaging settings were used), fluorescence channels were histogram normalized. Perinuclear F-actin intensities were calculated as the sum of normalized Phalloidin intensities within a nuclear border. DNA damage foci were determined by detecting 2D peaks in the normalized p-γH2a.x channel using the MATLAB script FastPeakFind (v. 1.7) previously programmed by Adi Natan. MATLAB code is available from the corresponding author upon request.

2.4.7. Lifeact Transfection and Analysis of Actin Dynamics

MSFs were transfected with mRuby-Lifeact-7 using Lipofectamine 3000 (Life Technologies) 18 h after seeding into stretch chambers; mRuby-Lifeact-7 was a gift from Michael Davidson (#54560, Addgene). One day after transfection, 2 µm image stacks (0.5 µm steps) of Actin (Lifeact) and Nuclei (H2b) were acquired during cyclic stretch and the following period of rest. Profile lines were generated with the Plot Profile function in ImageJ (NIH, v. 1.50e) using an 8 pixel (=2.1 µm) thick line. Binned profile analysis was performed using a custom MATLAB code that tracked cell and nuclear outlines during an image series using the Lifeact or H2b fluorescence channel, respectively. Image stacks were rotated to align actin filaments in the horizontal direction and projections of 8 pixel thick vertical profile lines that crossed through the nuclear center were extracted for further analysis. During each time step, profile line positions

were fixed with respect to the nuclear center. Using the position of the cell and nuclear boundary, profile lines were binned with 5 bins representing Lifeact intensities from the nuclear center to the inner nuclear border and another 5 bins representing intensities from the nuclear periphery to the cell border. Corresponding bins from each half of the cell were averaged. MATLAB code is available from the corresponding author upon request.

2.4.8. Statistical Analysis

One-way ANOVA with Tukey's Honestly Significant Difference post hoc test or two-tailed T-test analysis was performed to evaluate statistical significance using JMP Pro12 software (SAS Institute). Displayed error (SD=standard deviation, SEM=standard error of the mean), number of individual data points (n), number of independent experiments (exp., if different from n) as well as significances and statistical tests that were used are indicated in the figure captions.

2.5. ACKNOWLEDGEMENTS

We want to thank the Integrated Teaching and Learning Laboratory (ITLL) at the University of Colorado Boulder for help and advice with 3D printing. This work was supported in part by NIH grants R01 AR063712 and R21 AR066230, and NSF grant CMMI CAREER 1349735.

2.6. EXTENDED DATA

Extended Table 2.1. Component list of the LiMex stretch device. Pricing for the device depends on materials costs and 3D printing, including cost of printing material, density of the print, and facility charges. Parts were printed with the Objet30 3D prints (Ob) or uPrint SE Plus (uP) as indicated.

Component	***Material***	***Vendor***	***Quantity***
Main Chamber (Ob)	VeroClear	Computer Aided Technology	1
Membrane Ring (Ob)	VeroClear	Computer Aided Technology	1
Holding Clips (Ob)	VeroClear	Computer Aided Technology	3
Piston (uP)	ABS+	Computer Aided Technology	1
Deformation Ring Holder (uP)	ABS+	Computer Aided Technology	1
Electromagnet Case (uP)	ABS+	Computer Aided Technology	1
Slider Tube (uP)	ABS+	Computer Aided Technology	1
Deformation Ring	Delrin	Computer Aided Technology	1
Electromagnetic Coil	Cooper Wire	NA	10 m
Permanent Rare Earth Magnet	Neodymium	SuperMagnetMan	1
Slider Rails	Aluminum	Igus	3
Slider Carriages	NA	Igus	3
Arduino Microcontroller	NA	SparkFun Electronics	1
H-Bridge	NA	RB-Cyt-132, RobotShop	1

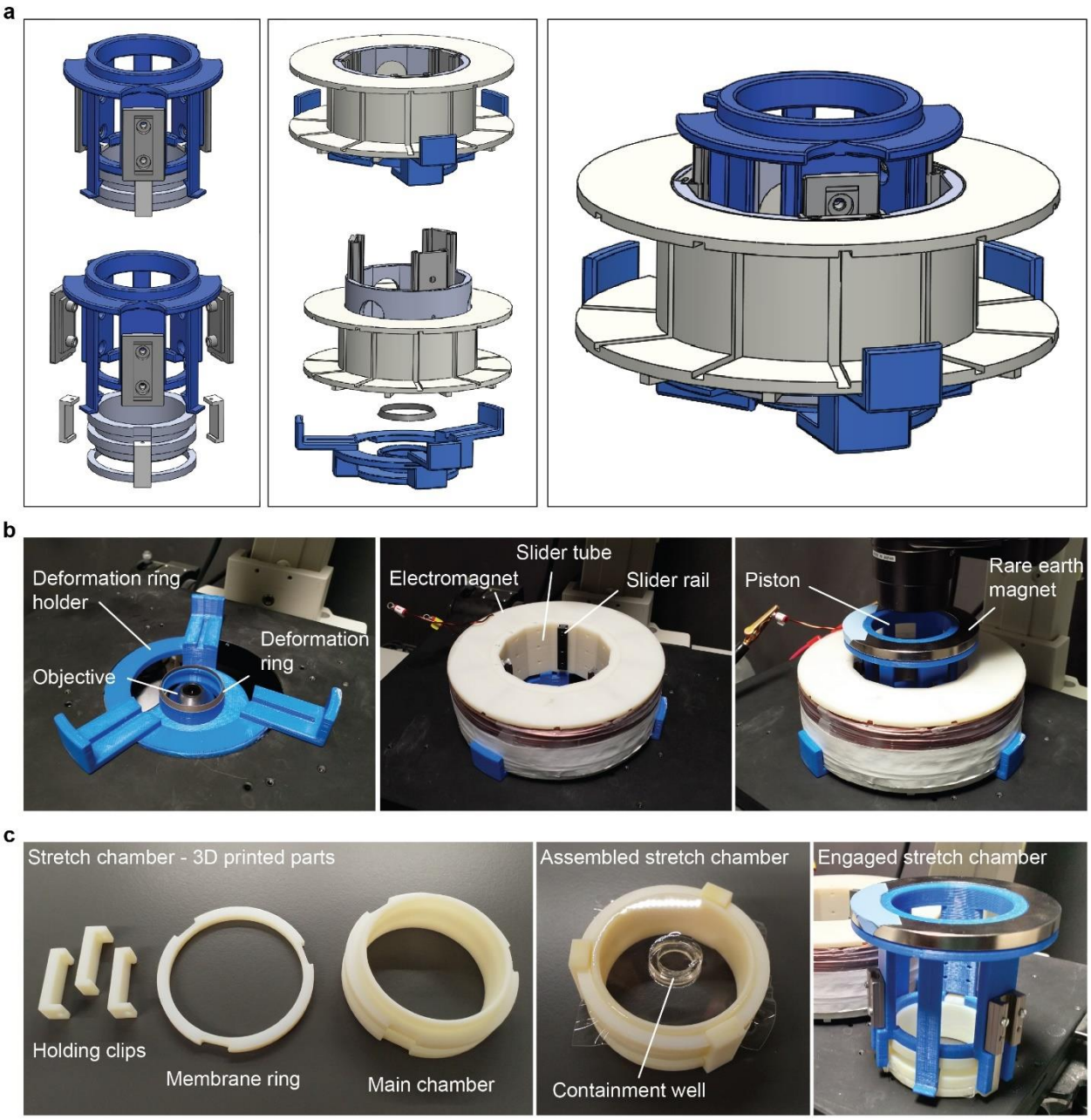

Extended Figure. 2.1. CAD sketches and real images of LiMex components and assembly. **a)** SolidWorks CAD drawings of the 3D printed stretch device components shown assembled or as blow-up. Drawings also show slider rails and carriages (in gray), which were purchased. **b)** The deformation ring holder is fixed into the manual stage of a Nikon Eclipse Ti Microscope by interlocking with two metal wings in the circular notch that otherwise holds an aluminum tray. The slider tube pushed tightly into the inner hole of the electromagnetic coil. Together, the slider tube and electromagnetic coil are placed on top of the deformation ring holder. The piston attached to a rare earth magnet is then placed into the slider tube via the friction-reduced

slider interface. **c)** The stretch chamber consisted of three parts which after assembly would fix a thin silicone membrane in place. A compliant silicon containment ring was fused to the silicon membrane prior to assembly to culture cells. The assembled stretch chamber can then be engaged into the piston and is held securely in place through bendable side pins that lock into the side grooves of the main chamber.

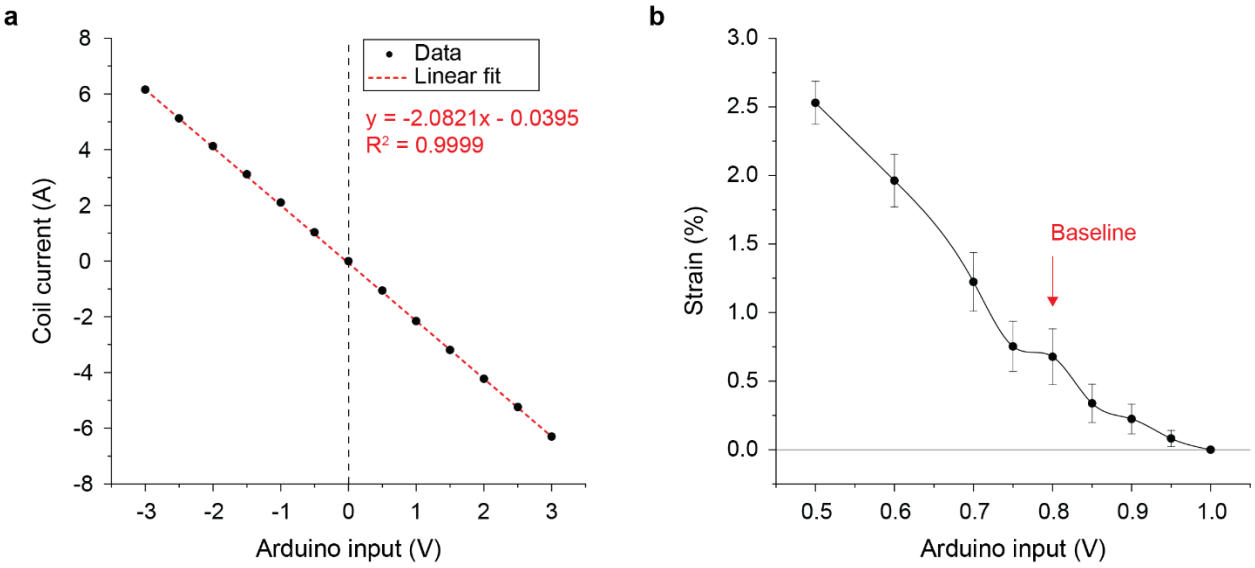

Extended Figure 2.2. Current control via Arduino input voltages and determination of baseline Arduino input voltage. a) Correspondence of Arduino input voltages to the amount of current received by the electromagnet coil was measured using a multimeter. **b)** The baseline Arduino input voltage is the input at which the membrane contacts the deformation ring without indention. Membrane containment wells were coated with 2 µm sized fluorescent beads and membrane strains were calculated using particle tracking. To determine the baseline, the membrane was suspended above the deformation ring and the Arduino input voltage was stepwise lowered (+1.0 to +0.5 V) while measuring the strain applied to the membrane via bead displacements. The baseline Arduino input voltage was determined to be +0.8 V as the input before distinct increases in membrane strain could be measured.

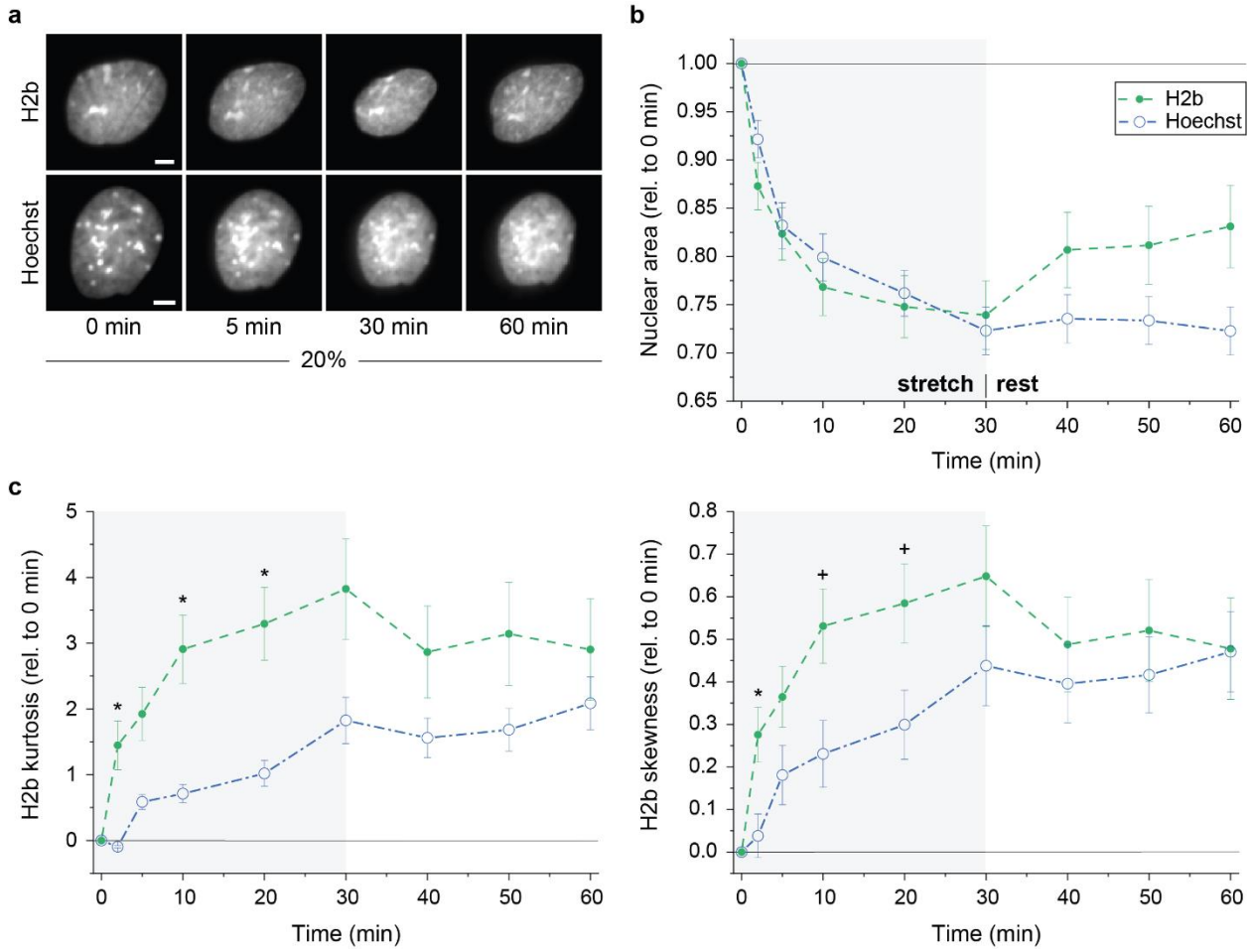

Extended Figure 2.3. Use of chromatin dyes changes nuclear response to high strain cyclic stretch in MSFs. Mouse embryonic skin fibroblasts were exposed to 20% cyclic strain for 30 min followed by 30 min of no stimulation (rest) during which image stacks of nuclei were recorded. To test the influence of chromatin dyes, cells were stained with Hoechst 33342 prior to experiments. **a)** Images of nuclei recorded via H2b-eGFP or Hoechst staining; scales=5 µm. **b, c)** Relative changes in nuclear area (relative to 0 min) and differences in H2b histogram kurtosis and skewness (compared to 0 min) during stretch routines between DAPI stained or unstained control cells (H2b). Hoechst stained cells showed reduced chromatin condensation during stretch and no regain in nuclear areas during rest; SEM; H2b same as Figure 2.3; Hoechst n=10 from 2 exp.; T-test: + $p<0.1$, * $p<0.05$.

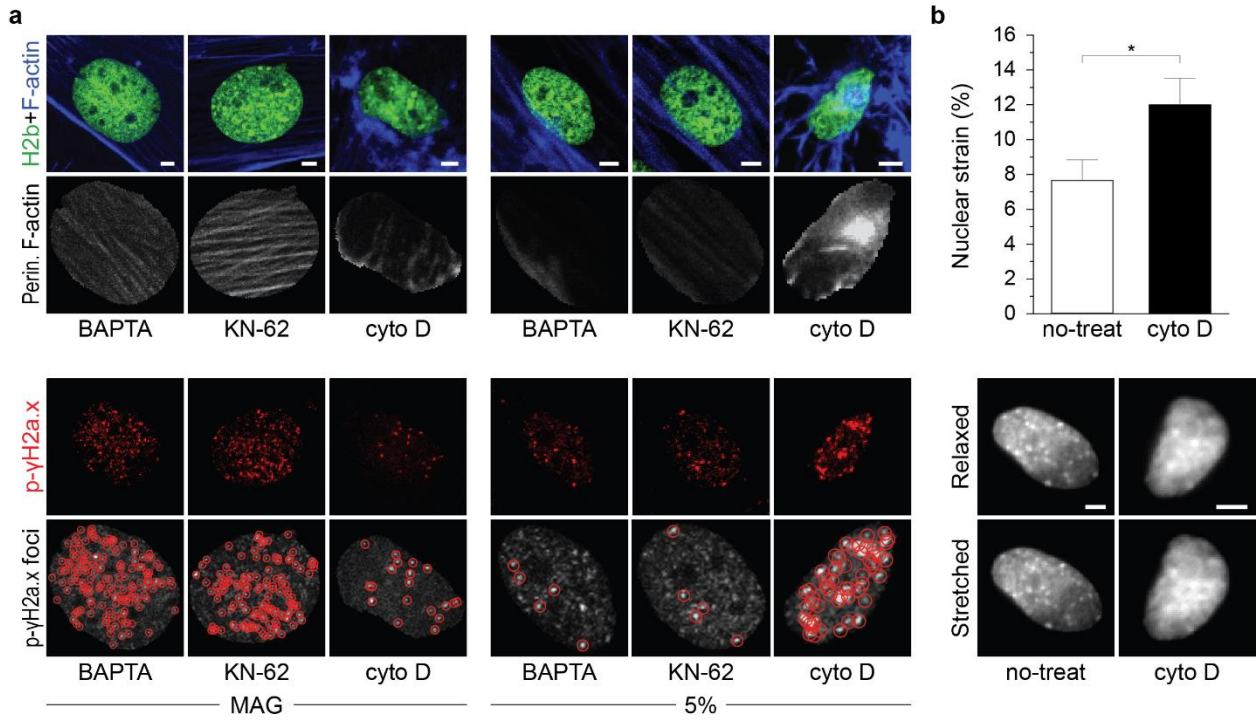

Extended Figure 2.4. Cyto D treated MSFs show higher nuclear strain transfer during stretch. Mouse embryonic skin fibroblasts were exposed to 30 min sigmoidal stretch routines after which cells were stained for γH2a.x phosphorylation (p-γH2a.x), indicating DNA double strand breaks, and F-actin. **a)** Additional immunostaining data for 5% cyclic stretch and magnetic field only (MAG) routines corresponding the Figure 2.5. **b)** After 20% cyclic stretch, images of nuclei were recorded under relaxed or stretched conditions to determine strain transfer from the membrane to nuclei. Cells treated with cyto D prior to experiments showed higher nuclear strains compared to untreated (no-treat) control cells; SEM; n=28 from 4 exp.; T-test: * $p<0.05$; all scales=5 µm.

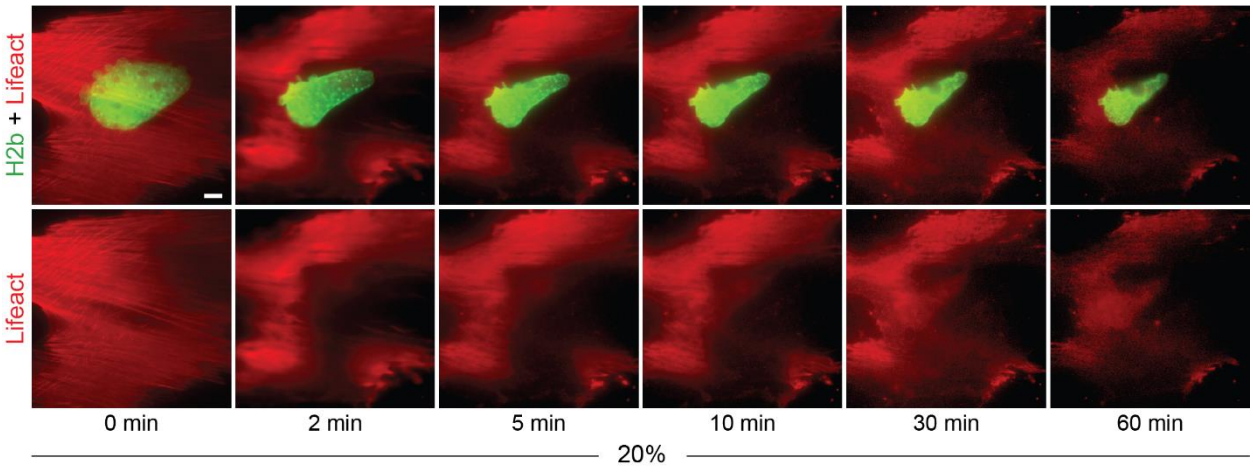

Extended Figure 2.5. Lifeact imaging of a cell undergoing cell death during high strain cyclic stretch. Mouse embryonic skin fibroblasts were transfected with mRuby-Lifeact-7 and, 24 h after, cells were exposed to 30 min of 20% sigmoidal stretch, followed by 30 min of no stimulation (rest). Image stacks of actin (Lifeact) or nuclei (H2b) were recorded during the stretch routine. Image series shows a cell undergoing apoptosis shortly after start of the high strain routine; scale=10 µm.

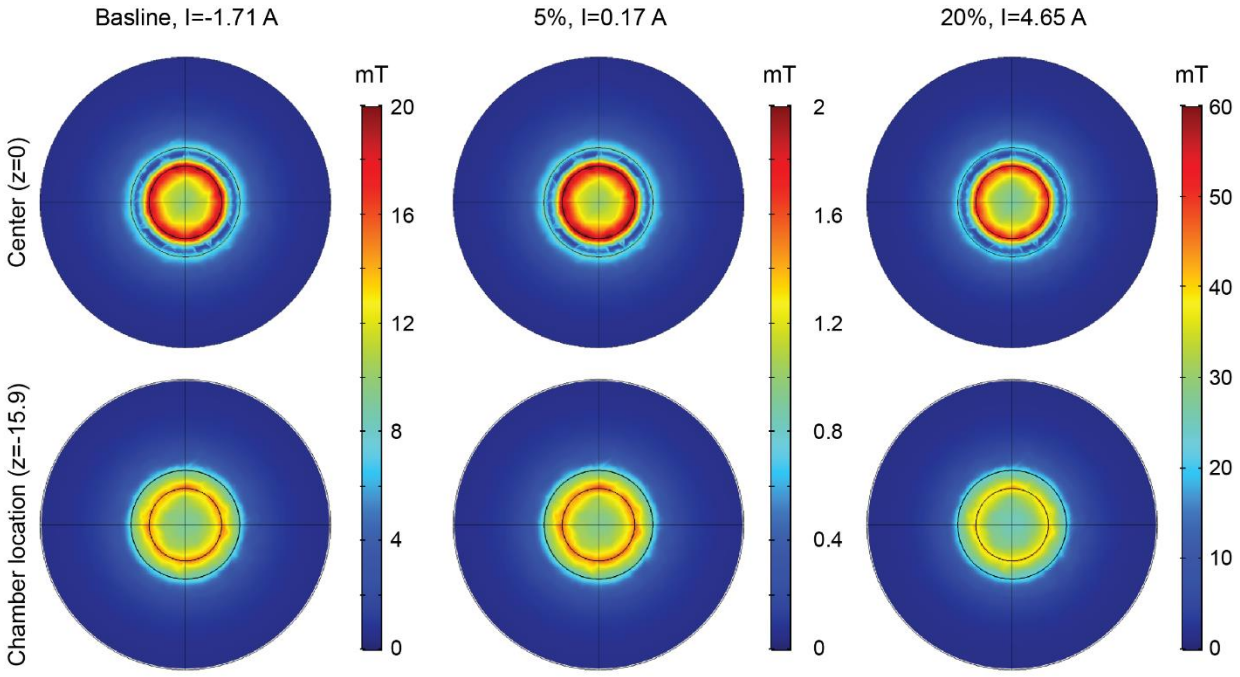

Extended Figure 2.6. COMSOLE-modeling of electromagnetic fields. Shown is top view of magnetic fields produced by the electromagnetic coil during peak strains corresponding to 5% or 20% strain routines, or during rest (baseline). Two different z-planes are presented: at the center of the coil (*z*=0 mm) and at the location of the membrane close to the bottom of the coil (*z*=15.9 mm). Amount of current used to produce the field are as indicated at the top.

2.7. REFERENCES

1. Engler, A. J., Sen, S., Sweeney, H. L. & Discher, D. E. Matrix elasticity directs stem cell lineage specification. *Cell* **126**, 677–89 (2006).
2. Engler, A. J. *et al.* Embryonic cardiomyocytes beat best on a matrix with heart-like elasticity: scar-like rigidity inhibits beating. *J. Cell Sci.* **121**, 3794–802 (2008).
3. Pasqualini, F. S. *et al.* Traction force microscopy of engineered cardiac tissues. *PLoS One* **13**, e0194706 (2018).
4. Hemphill, M. A., Dauth, S., Yu, C. J., Dabiri, B. E. & Parker, K. K. Traumatic brain injury and the neuronal microenvironment: a potential role for neuropathological mechanotransduction. *Neuron* **85**, 1177–92 (2015).
5. del Real, A. *et al.* Differential analysis of genome-wide methylation and gene expression in mesenchymal stem cells of patients with fractures and osteoarthritis. *Epigenetics* **12**, 113–122 (2017).
6. Thienpont, B. *et al.* The H3K9 dimethyltransferases EHMT1/2 protect against pathological cardiac hypertrophy. *J. Clin. Invest.* **127**, 335–348 (2017).
7. Zhang, Q. J. *et al.* The histone trimethyllysine demethylase JMJD2A promotes cardiac hypertrophy in response to hypertrophic stimuli in mice. *J. Clin. Invest.* **121**, 2447–2456 (2011).
8. Carter, D. R. *et al.* The mechanobiology of articular cartilage development and degeneration. *Clin. Orthop. Relat. Res.* **427**, S69-77 (2004).
9. Jaalouk, D. E. & Lammerding, J. Mechanotransduction gone awry. *Nat. Rev. Mol. Cell Biol.* **10**, 63–73 (2009).

10. Manilal, S., Nguyen, T. M., Sewry, C. A. & Morris, G. E. The Emery-Dreifuss muscular dystrophy protein, emerin, is a nuclear membrane protein. *Hum. Mol. Genet.* **5**, 801–808 (1996).

11. Lampi, M. C. & Reinhart-King, C. A. Targeting extracellular matrix stiffness to attenuate disease: From molecular mechanisms to clinical trials. *Sci. Transl. Med.* **10**, eaao0475 (2018).

12. Huh, D., Torisawa, Y., Hamilton, G. A., Kim, H. J. & Ingber, D. E. Microengineered physiological biomimicry: organs-on-chips. *Lab Chip* **12**, 2156–64 (2012).

13. Rosellini, E. *et al.* Protein/polysaccharide-based scaffolds mimicking native extracellular matrix for cardiac tissue engineering applications. *J. Biomed. Mater. Res. Part A* **106**, 769–781 (2018).

14. Crisp, M. *et al.* Coupling of the nucleus and cytoplasm: Role of the LINC complex. *J. Cell Biol.* **172**, 41–53 (2006).

15. Aureille, J., Belaadi, N. & Guilluy, C. Mechanotransduction via the nuclear envelope: a distant reflection of the cell surface. *Curr. Opin. Cell Biol.* **44**, 59–67 (2017).

16. Lee, H. *et al.* Cytoskeletal prestress regulates nuclear shape and stiffness in cardiac myocytes. *Exp. Biol. Med. (Maywood).* **240**, 1543–54 (2015).

17. Heo, S. J. *et al.* Biophysical regulation of chromatin architecture instills a mechanical memory in mesenchymal stem cells. *Sci. Rep.* **5**, 16895 (2015).

18. Heo, S.-J. *et al.* Differentiation alters stem cell nuclear architecture, mechanics, and mechano-sensitivity. *Elife* **5**, (2016).

19. Liu, J. *et al.* Caspase-3-mediated cyclic stretch-induced myoblast apoptosis via a Fas/FasL-independent signaling pathway during myogenesis. *J. Cell. Biochem.* **107**, 834–

44 (2009).

20. Guilluy, C. *et al.* Isolated nuclei adapt to force and reveal a mechanotransduction pathway in the nucleus. *Nat. Cell Biol.* **16**, 376–381 (2014).

21. Tajik, A. *et al.* Transcription upregulation via force-induced direct stretching of chromatin. *Nat. Mater.* (2016). doi:10.1038/nmat4729

22. Uzer, G. *et al.* Cell mechanosensitivity to extremely low-magnitude signals is enabled by a LINCed nucleus. *Stem Cells* **33**, 2063–2076 (2015).

23. Iyer, K. V., Pulford, S., Mogilner, A. & Shivashankar, G. V. Mechanical activation of cells induces chromatin remodeling preceding MKL nuclear transport. *Biophys. J.* **103**, 1416–1428 (2012).

24. Ghosh, S. *et al.* Deformation Microscopy for Dynamic Intracellular and Intranuclear Mapping of Mechanics with High Spatiotemporal Resolution. *Cell Rep.* **27**, 1607-1620.e4 (2019).

25. Seelbinder, B. *et al.* The nucleus mediates mechanosensitive reorganization of epigenetically marked chromatin during cardiac maturation and pathology. *BioRXiv* (2018). doi:10.1101/455600

26. Le, H. Q. *et al.* Mechanical regulation of transcription controls Polycomb-mediated gene silencing during lineage commitment. *Nat. Cell Biol.* **18**, 864–875 (2016).

27. Bartalena, G. *et al.* A novel method for assessing adherent single-cell stiffness in tension: design and testing of a substrate-based live cell functional imaging device. *Biomed. Microdevices* **13**, 291–301 (2011).

28. Harshad, K. *et al.* An electromagnetic cell-stretching device for mechanotransduction studies of olfactory ensheathing cells. *Biomed. Microdevices* **18**, 1–10 (2016).

29. Toume, S., Gefen, A. & Weihs, D. Printable low-cost, sustained and dynamic cell stretching apparatus. *J. Biomech.* **49**, 1336–1339 (2016).

30. Deguchi, S., Kudo, S., Matsui, T. S., Huang, W. & Sato, M. Piezoelectric actuator-based cell microstretch device with real-time imaging capability. *AIP Adv.* **5**, 1–6 (2015).

31. Huang, L., Mathieu, P. S. & Helmke, B. P. A Stretching Device for High-Resolution Live-Cell Imaging. *Ann. Biomed. Eng.* **38**, 1728–1740 (2010).

32. Shao, Y. *et al.* Uniaxial cell stretching device for live-cell imaging of mechanosensitive cellular functions. *Rev. Sci. Instrum.* **84**, 1–8 (2013).

33. Chalut, K. J. *et al.* Chromatin decondensation and nuclear softening accompany Nanog downregulation in embryonic stem cells. *Biophys. J.* **103**, 2060–70 (2012).

34. Martiel, J.-L. *et al.* Measurement of cell traction forces with ImageJ. *Methods Cell Biol.* **125**, 269–87 (2015).

35. Herbomel, G. *et al.* Wavelet transform analysis of chromatin texture changes during heat shock. *J. Microsc.* **262**, 295–305 (2016).

36. Upadhyay, D., Correa-Meyer, E., Sznajder, J. I. & Kamp, D. W. FGF-10 prevents mechanical stretch-induced alveolar epithelial cell DNA damage via MAPK activation. *Am. J. Physiol. Lung Cell. Mol. Physiol.* **284**, L350-9 (2003).

37. Mayr, M., Hu, Y., Hainaut, H. & Xu, Q. Mechanical stress-induced DNA damage and rac-p38MAPK signal pathways mediate p53-dependent apoptosis in vascular smooth muscle cells. *FASEB J.* **16**, 1423–5 (2002).

38. Rogakou, E. P., Pilch, D. R., Orr, A. H., Ivanova, V. S. & Bonner, W. M. DNA Double-stranded Breaks Induce Histone H2AX Phosphorylation on Serine 139. *J. Biol. Chem.* **273**, 5858–5868 (1998).

39. Khatau, S. B. *et al.* A perinuclear actin cap regulates nuclear shape. *Proc. Natl. Acad. Sci.* **106**, 19017–19022 (2009).

40. Tenuzzo, B. *et al.* Biological effects of 6 mT static magnetic fields: a comparative study in different cell types. *Bioelectromagnetics* **27**, 560–77 (2006).

41. Chionna, A. *et al.* Cell shape and plasma membrane alterations after static magnetic fields exposure. *Eur. J. Histochem.* **47**, 299–308 (2003).

42. Miyakoshi, J. Effects of static magnetic fields at the cellular level. *Prog. Biophys. Mol. Biol.* **87**, 213–223 (2005).

43. Ghodbane, S., Lahbib, A., Sakly, M. & Abdelmelek, H. Bioeffects of static magnetic fields: oxidative stress, genotoxic effects, and cancer studies. *Biomed Res. Int.* **2013**, 602987 (2013).

44. Fanelli, C. *et al.* Magnetic fields increase cell survival by inhibiting apoptosis via modulation of Ca2+ influx. *FASEB J.* **13**, 95–102 (1999).

45. Panagopoulos, D. J., Karabarbounis, A. & Margaritis, L. H. Mechanism for action of electromagnetic fields on cells. *Biochem. Biophys. Res. Commun.* **298**, 95–102 (2002).

46. Huang, L., Dong, L., Chen, Y., Qi, H. & Xiao, D. Effects of sinusoidal magnetic field observed on cell proliferation, ion concentration, and osmolarity in two human cancer cell lines. *Electromagn. Biol. Med.* **25**, 113–26 (2006).

47. Pirozzoli, M. C. *et al.* Effects of 50 Hz electromagnetic field exposure on apoptosis and differentiation in a neuroblastoma cell line. *Bioelectromagnetics* **24**, 510–516 (2003).

48. Juutilainen, J. & Saali, K. Development of chick embryos in 1 Hz to 100 kHz magnetic fields. *Radiat. Environ. Biophys.* **25**, 135–40 (1986).

CHAPTER 3

INTRA-NUCLEAR TENSILE STRAIN MEDIATES REORGANIZATION OF EPIGENETICALLY MARKED CHROMATIN DURING CARDIAC DEVELOPMENT AND DISEASE

ABSTRACT

Environmental mechanical cues are critical to guide cell fate. Forces transmit to the nucleus through the Linker of Nucleo- and Cytoskeleton (LINC) complex and are thought to influence the organization of chromatin that is related to cell differentiation; however, the underlying mechanisms are unclear. Here, we investigated chromatin reorganization during murine cardiac development and found that cardiomyocytes establish a distinct architecture characterized by relocation of H3K9me3-modified chromatin from the nuclear interior to the periphery and co-localization to myofibrils. This effect was abrogated in stiff environments that inhibited cardiomyocyte contractility, or after LINC complex disruption, and resulted in the relocation of H3K27me3-modified chromatin instead. By generating high-resolution intra-nuclear strain maps during cardiomyocyte contraction, we discovered that the reorganization of H3K9me3-marked chromatin is influenced by tensile, but not compressive, nuclear strains. Our findings highlight a new role for nuclear mechanosensation in guiding cell fate through chromatin reorganization in response to environmental cues.

3.1. INTRODUCTION

Mechanics of cell microenvironments play an important role in directing cell differentiation during development[1] and maintaining tissue health during adulthood[2]. Changes in mechanical properties due to acute trauma, chronic conditions, or genetic predispositions lead to cellular degeneration and result in a range of pathologies[3], including cardiac hypertrophy[4,5]. Further, regenerative medicine aims to engineer suitable microenvironments to guide cell fates for enhanced tissue regeneration. However, little is known about the underlying mechanisms that facilitate cell differentiation in response to environmental cues.

The nucleus is thought to be an essential mechanosensitive organelle[6–10] as it is tightly connected to all parts of the cytoskeleton through LINC (Linker of Nucleo- and Cytoskeleton) complexes[11] comprised of proteins that span the inner (SUNs) and outer (nesprins) nuclear membranes[12,13]. Studies on isolated nuclei demonstrated that the nucleus alone can respond to stretch; however, only when engaged via LINC complexes[14]. Mutations in LINC complex and nuclear envelope proteins are also related to developmental disorders[15], particularly in mechanically active tissues such as cardiac and skeletal muscle[16,17]. In addition, there is a direct relation between nuclear architecture and cell differentiation. Chromatin organization changes from an unstructured organization in the zygote to a cell type-specific organization during development[18–22]. The 4D Nucleome Project aims to generate spatial maps of human and mouse genomes to better understand this relationship[23]. Since the nucleus makes up a large portion of the cell, type-specific nuclear morphology can also have direct implications for cellular functions as has been described for plasma cells[24], neutrophil granulocytes[25], T-cells[26] and photoreceptor cells[27]. Together, this suggests that biophysical signals from the cell environment might guide cell

behavior through spatial rearrangement of chromatin; however, no study has investigated the effect of nuclear strains on chromatin organization.

To bridge this gap, we investigated the reorganization of chromatin during cardiomyocyte (CM) development and pathology in mice. CMs show poor contractility and inhibited differentiation on substrates that are stiffer than their native environment[28–30]. Due to their well-investigated behavior in response to substrate stiffness and contraction-mediated deformation of nuclei, CMs provided a good model to investigate the relation between micro-environment, cell differentiation, and chromatin organization, as well as the potential role of nuclear mechanosensation in these processes. We documented the establishment of a distinct nuclear architecture during development and found evidence that tensile nuclear strains, transferred from myofibrils via LINC complexes, guided the reorganization of H3K9me3-modified chromatin to establish this architecture. Reduction of nuclear strains in stiff environments or disruption of LINC complexes inhibited the formation of the CM nuclear architecture and lead to the rearrangement of H3K27me3-modified chromatin instead. To find direct evidence for a link between nuclear deformation and chromatin reorganization in CMs, we used a recently developed method called *deformation microscopy*[31,32] to generate high resolution intra-nuclear strain maps from microscopy-based image series recorded during CM contractions and devised a workflow to map these strains back to chromatin regions with different epigenetic modifications. Overall our findings suggest a new role for nuclear mechanosensation in CMs in which the nucleus integrates mechanical signals from the environment through the reorganization of epigenetically marked chromatin to guide and stabilize cell differentiation.

3.2. RESULTS

3.2.1. CMs Adopt a Distinct Nuclear Architecture During Development

To study the relationships between functional microenvironments, nuclear morphology, and chromatin organization, we used adult H2b-eGFP mice to analyze nuclear architectures in primary cells of tissues with different stiffness properties and that undergo a broad range of mechanical challenges (**Figure 3.1a**)[33]. While all cell types showed distinct nuclear architectures, nuclei of CMs had an elongated morphology with chromatin accumulated at the nuclear periphery and inner cavities that appeared almost void of chromatin. In contrast, cardiofibroblasts (CF), which shared a similar mechanical environment and had an elongated nuclear morphology, showed a homogeneous distribution of chromatin throughout the nucleus. Analysis of late stage (E)18.5 embryonic hearts revealed that the nuclear architecture observed in adult CMs was not present in embryonic CMs (**Figure 3.1b**), suggesting that the adult nuclear phenotype forms postnatally when a sudden increase in cardiac activity triggers CM maturation.

To analyze the formation of the adult nuclear phenotype in CMs during development, we isolated embryonic cardiac cells from (E)18.5 mouse hearts by using an optimized mixture of ECM-specific peptidases (see methods for details) to achieve high cell yields and high viability compared to existing tryptic methods[34]. Isolated cells were plated on soft (13 kPa) silicone substrates (polydimethylsiloxane, PDMS), coated with basement membrane proteins, to mimic the mechanical environment of adult hearts[28,29,35]. The resulting cardiac co-culture contained a high percentage (61%) of embryonic CMs, assessed by the formation of myofibrils, even without enrichment of CMs through pre-plating (**Extended Figure 3.1**). Embryonic CMs grew in connected clusters, started coordinated contractions within 24 hours of plating, and remained at a high ratio over a four-day culture period (**Figure 3.2a**). After two days in culture, nuclear

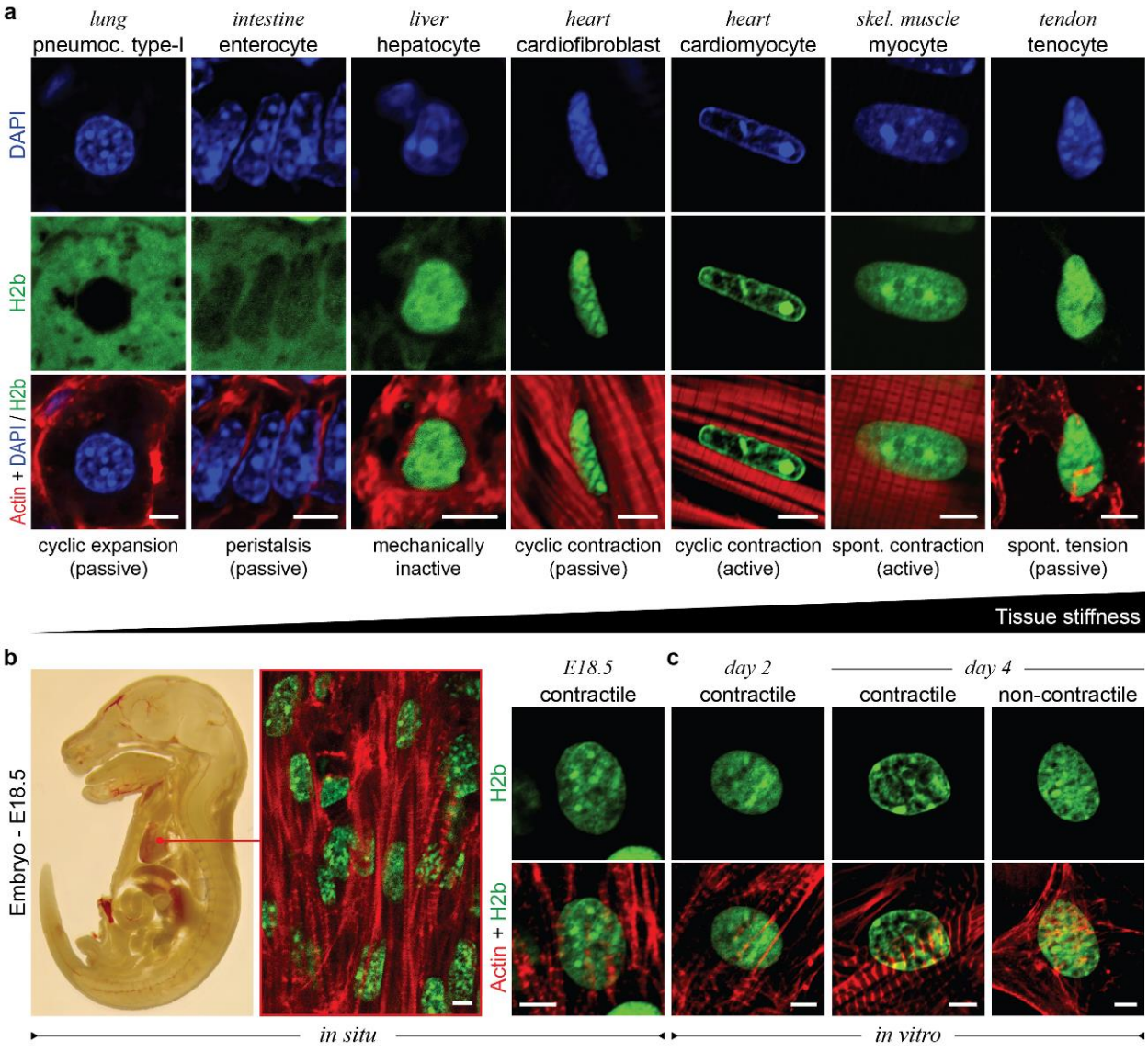

Figure 3.1. Cardiomyocytes adopt a distinct nuclear architecture with high amounts of peripheral chromatin during development. a) Tissues with diverse mechanical characteristics were harvested from adult H2b-eGFP mice and stained for actin. DAPI was used as DNA counterstain for soft tissues with weak H2b-eGFP fluorescence. Adult CMs had an elongated nucleus with a high ratio of peripheral chromatin compared to other cell types. **b)** Embryos from H2b-eGFP mice were harvested at embryonic day (E)18.5, sectioned and stained for actin. Left: whole embryo mid-section. Middle: close-up of embryonic cardiac tissue from mid-section. Right: close-up of an embryonic CM nucleus, which showed a diffuse nuclear organization unlike adult CMs. **c)** Embryonic cardiac cells were isolated from (E)18.5 H2b-eGFP mice hearts and plated on soft (13 kPa) PDMS substrates for two or four days. Embryonic CMs with contractile myofibrils showed a change in nuclear organization at day four. All scales=5 µm.

phenotypes of CMs still appeared diffuse with no distinctive accumulation of heterochromatin at the nuclear envelope (**Figure 3.1c**). However, after four days, embryonic CMs exhibited intranuclear cavities devoid of chromatin and an overall shift of chromatin towards the nuclear periphery like adult CMs. Interestingly, non-contractile CFs present in the culture continued to display a diffuse nuclear architecture more similar to adult CFs. These findings provided further support for a link between chromatin organization and cell differentiation and suggest that CMs form a cell type-specific nuclear architecture during development.

3.2.2. Substrate Stiffness Affects Histone and Epigenetic Enzyme Expression in Embryonic Cardiac Cells In Vitro

To better understand the relationship between CM-specific nuclear architecture and CM differentiation, we next screened for changes in gene expression related to chromatin remodeling in an *in vitro* model of cardiac dedifferentiation. Embryonic CMs show reduced contractility and dedifferentiate in environments that are stiffer than native cardiac tissue (12 ± 4 kPa)[28–30]. We verified these results by analyzing the ratio of contractile CMs to non-contractile CFs, assessed by the formation of contractile myofibrils, of embryonic cardiac cells plated on stiff (140 kPa) PDMS compared to soft (13 kPa) PDMS (**Extended Figure 3.1**). While the percentage of contractile CMs was similar between soft and stiff substrates after two days in culture (61% vs. 57%) it was decreased by more than half on stiff substrates on day four (58% vs. 25%, **Figure 3.2a**).

To analyze changes in the expression of genes associated to chromatin organization, we performed a comparative RNAseq analysis between cardiac cells plated on soft or stiff PDMS for four days. Of 114 annotated mouse histone genes[36], we found 82 were expressed in our culture (**Extended Table 3.1**), of which 67 were more than 30% downregulated on stiff substrates (**Figure 3.2b**). The expression of replication-dependent canonical histones was particularly reduced across

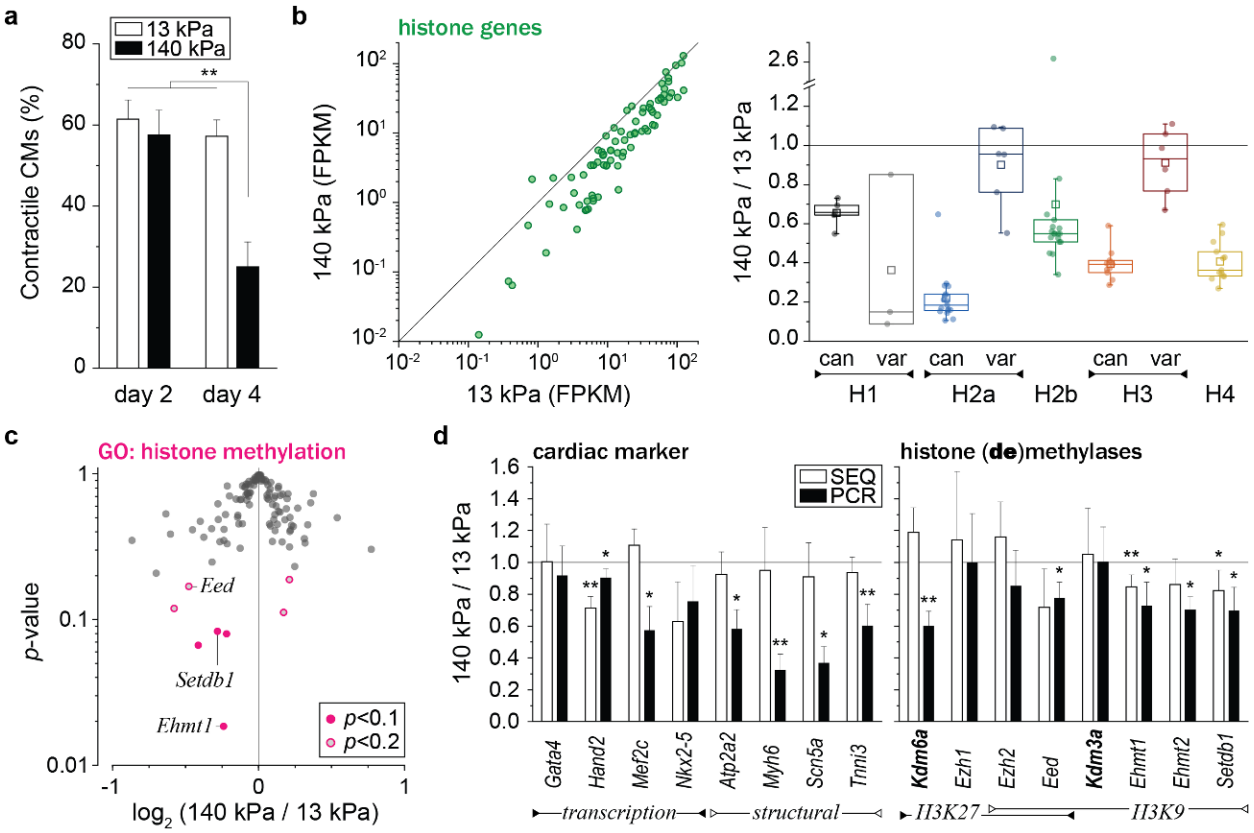

Figure 3.2. Substrate stiffness affects gene expression of histones and histone modifying enzymes in embryonic cardiac cultures. Cells were isolated from (E)18.5 H2b-eGFP embryo hearts and cultured on soft (13 kPa) or stiff (140 kPa) PDMS. **a)** After two and four days, cultures were stained for actin (Extended Figure 3.1) and the ratio of CMs with contractile myofibrils to non-contractile CFs was determined. The percentage of contractile CMs was significantly reduced after four days on stiff substrates compared to soft; SEM, n=9 from 3 exp., 2W-ANOVA: ** $p<0.01$. **b)** Total RNA was collected after four days of culture. RNAseq analysis revealed that most of the 82 expressed histone genes were downregulated on stiff PDMS. Canonical histones (can) were consistently downregulated for all histone families while non-canonical histone variants (var) showed varying levels of expression changes between substrates; n=4; FPKM: Fragments Per Kilobase of transcript per Million mapped reads. **c)** Volcano plot of genes associated with the gene ontology term *histone methylation* (GO:0016571) as determined by RNAseq. Indicated are genes coding for H3K9 methylases, which were amongst the most significantly altered (Extended Table 3.2). **d)** PCR validation of RNAseq (SEQ) data verified downregulation of H3K9 methylating genes and showed that cardiac transcription and structural marker were decreased on stiff substrates. H3K9 demethylase *Kdm3a* and H3K27-specific methylase *Ezh1* showed no change while H3K27 demethylase *Kdm6a* was downregulated, indicating inverse methylation activity between H3K9 and H3K27 for cardiac cells on stiff substrates; SD; n=4; T-test: * $p<0.05$, ** $p<0.01$.

all histone families which indicated that cardiac cell proliferation was inhibited on stiff substrates as reported previously[30]. However, we also observed downregulation of H1, H2a and H3 histone variants that replace canonical histones independent of replication and play a regulatory role in cell differentiation. H1[37] and H2a[38] variants have been implicated in the reprogramming of pluripotent stem cells and H3 variants have shown to play a role in neuronal development[39] and cardiac hypertrophy[40]. This change of histone variant expression in stiff environments provided further evidence for a link between CM differentiation and chromatin organization.

Moreover, pathway analysis identified several signal transduction pathways involved in cell differentiation and cardiac signaling (**Extended Table 3.2**). Functional network grouping showed that pathways related to cell-ECM interactions were associated to MAPK (**Extended Figure 3.2a**), an important pathway for cardiac development[41] as well as epigenetic regulation[42], which has been shown to influence chromatin positioning[43]. Gene ontology (GO) term enrichment analysis of differentially expressed ($p<0.2$) genes with the parent GO term *histone modification* (GO:0016570) revealed the child GO terms *histone methylation* (GO:0016571) and *histone acetylation* (GO:0016573) as significantly enriched (p=1.30E-9, p=5.50E-6). Closer investigation revealed that genes coding for the H3K9 methylases (aka methyltransferases) *Ehmt1*, *Setdb1* and *Eed* were among the most downregulated for cells cultured on stiff substrates (**Figure 3.2c, Extended Table 3.3**). Methylation of H3K9 is associated with strong gene repression and chromatin condensation[44] and has been shown to be crucial during cardiac development[45] and maintenance[4]. RT-qPCR analysis validated the downregulation of H3K9 methylases, as well as downregulation of cardiac transcription factors and structural markers, while no change in gene expression was observed for the H3K9 demethylase *Kdm3a* (**Figure 3.2d**) on stiff substrates compared to soft. *Eed* and *Ezh2* are also associated with the methylation of H3K27, in addition to

H3K9 (**Extended Table 3.3**). Similar to H3K9, methylation of H3K27 is associated with gene repression and heterochromatin formation[44]; however, it has an opposing function during cardiac development and needs to be repressed for cardiac differentiation[46]. In accordance, PCR data showed that H3K27 demethylase *Kdm6a* was downregulated while H3K27-specific methylase *Ezh1* remained unchanged on stiff PDMS. Overall, gene expression analysis validated the inhibitory effect of stiff environments on CM differentiation and showed that the expression of histone variants and epigenetic enzymes, particularly those involved in H3K9 and H3K27 methylation, were altered in stiff environments.

3.2.3. H3K9 and H3K27 Trimethylated Chromatin Shows Opposing Patterns of Reorganization Between Embryonic CMs and CFs During In Vitro Cultures

Similar to the nuclear organization in adult CMs, we observed an enrichment of chromatin at the nuclear border as well as a reduction in chromatin at the nuclear center when embryonic CMs were cultured for four days *in vitro* on soft (13 kPa) PDMS. We quantified overall chromatin enrichment by analyzing H2b-eGFP intensity over the relative distance to the nuclear center (0=center, 1=periphery) to verify this initial observation. A peripheral enrichment score was calculated as the ratio of the average intensity of the peripheral bin (0.85-0.95) divided by the center bin (0.05-0.15). Embryonic CMs, as identified via the formation of contractile myofibrils (**Figure 3.3a**, **Extended Figure 3.3a**), showed only minor accumulation of chromatin after two days in culture (**Figure 3.3b-d**). However, after four days, chromatin was significantly enriched at the nuclear border (1.17 to 1.76). In contrast, we observed a decrease in peripheral chromatin enrichment from day two compared to day four in non-contractile CFs (1.09 to 0.98).

Gene expression analysis of cardiac cultures on stiff substrates associated to CM dedifferentiation revealed specific changes in the expression of enzymes involved in histone H3

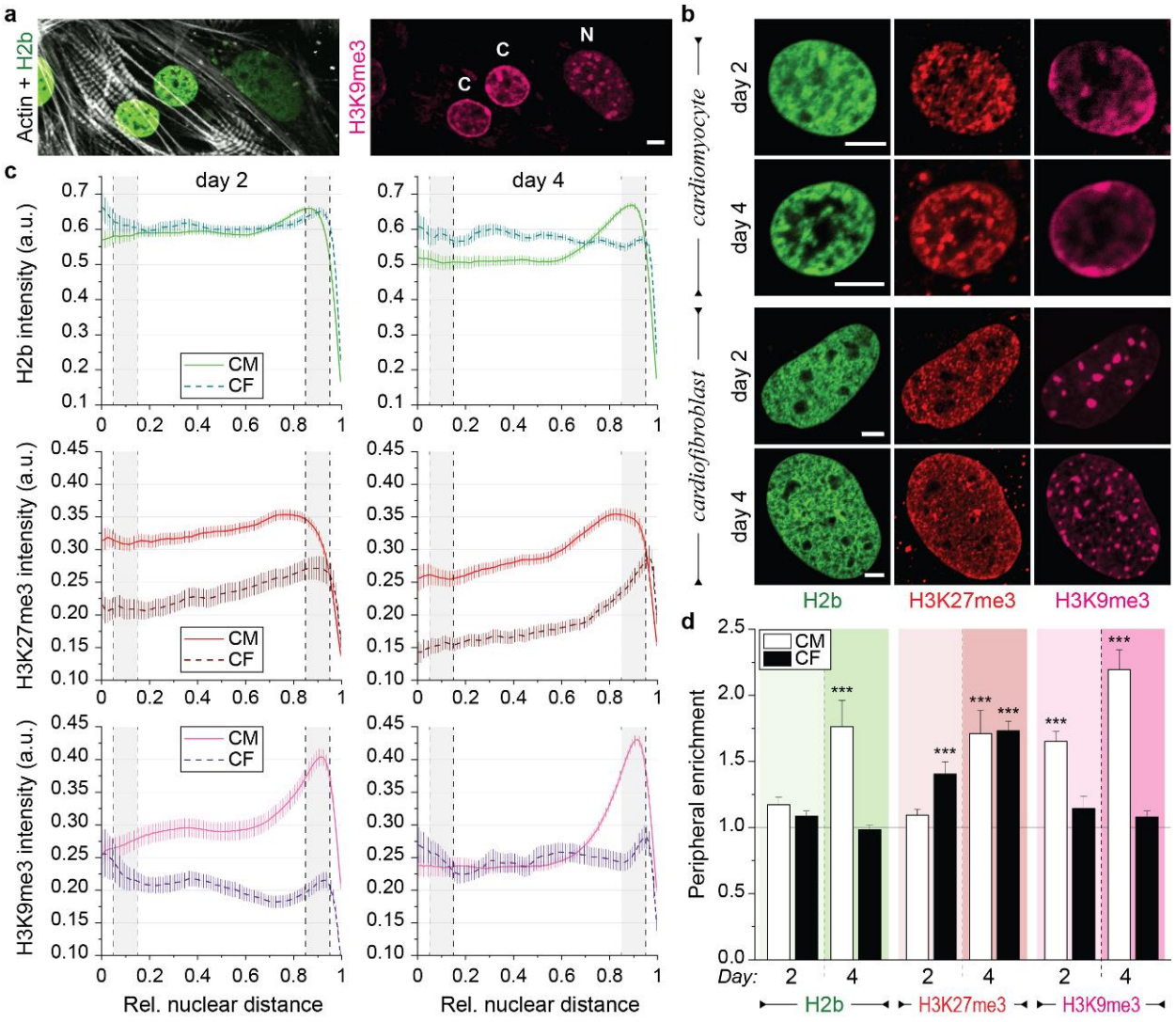

Figure 3.3. Contractile CMs and non-contractile CFs show opposing enrichment of H3K9 and H3K27 trimethylated chromatin *in vitro*. Embryonic cardiac cells were isolated from (E)18.5 H2b-eGFP embryo hearts and cultured on soft (13 kPa) PDMS substrates. **a)** After two days in culture, contractile CMs (C) with distinctly expressed myofibrils showed peripheral accumulation of H3K9me3-modified chromatin while non-contractile CFs (N) with actin fibers had a homogenous distribution of H3K9me3 clusters throughout the nucleus (see also Extended Figure 3.3a). **b)** Cells were stained for H3K27me3 and H3K9me3 (and actin, see Extended Figure 3.3b) and images of nuclei from CMs or CFs were acquired at day two or four of culture. **c)** Stained nuclei were analyzed for peripheral enrichment of overall chromatin (H2b) or epigenetically marked chromatin using a custom MATLAB code. Fluorescence intensity of each chromatin channel was analyzed with respect to its relative distance to the nuclear center (0=center, 1=periphery). Gray areas indicate the center bin (0.05-0.15) and the peripheral bin (0.85-0.95) used to calculate enrichment scores. SEM; n>60 from 5 exp. **d)** For each marker in

each nucleus, an enrichment score was calculated as the quotient of intensity of the peripheral bin divided by the center bin. CMs, but not CFs, showed a shift of overall chromatin towards the nuclear border at day four. This was preceded by enrichment of H3K9me3-marked chromatin at both day two and four in CMs, while CFs showed enrichment of H3K27me3-modified chromatin instead; SEM; n>60 from 5exp.; T-test (HM=1): *** p<0.001. All scales=5 µm.

methylation. Immunostaining of cardiac cultures showed that H3K9 trimethylated (H3K9me3) chromatin accumulated at the nuclear border in CMs while there was a homogenous distribution of H3K9me3 clusters throughout the nucleus of CFs (**Figure 3.3a**, **Extended Figure 3.3b**). Further quantification showed that H3K9me3-modified chromatin was significantly enriched at the nuclear border in CMs, but not in CFs on day two. This trend continued as we observed an increase in enrichment in CMs (1.65 to 2.20) compared to a slight decrease in CFs (1.14 to 1.08, **Figure 3.3d**). In turn, CFs showed increasing enrichment of H3K27me3-marked chromatin from days two to four (1.41 to 1.73). In CMs, peripheral enrichment of H3K27me3 occurred only on day four in conjunction with, and to the same extent as, overall chromatin. Furthermore, patterns of H3K27 methylation closely matched that of overall chromatin in CMs (**Figure 3.3b**), suggesting that enrichment of H3K27me3-marked chromatin mainly resulted from overall chromatin rearrangement in CMs. In contrast, enrichment of H3K27me3 occurred in the absence of peripheral enrichment of overall chromatin in CFs. These results validated the contrary roles of H3K9 and H3K27 methylation in cardiac development, as embryonic CMs and CFs showed opposing patterns of enrichment over time. Furthermore, our results suggest that the trimethylation of H3K9 may play a role in guiding the observed chromatin reorganization during CM development, because the accumulation of H3K9me3-marked chromatin at the nuclear periphery preceded the accumulation of overall chromatin.

3.2.4. Chromatin Reorganization is Abrogated in Stiffened Environments in Embryonic CMs In Vitro and Adult CMs In Vivo

H3K9me3-marked chromatin was enriched at the nuclear border of CMs whereas H3K27me3 was enriched at the border of CFs during our four-day *in vitro* culture model. To further investigate whether H3K9me3-associated chromatin reorganization is related to CM differentiation *in vitro*, we analyzed peripheral chromatin enrichment in embryonic CMs plated on soft (13 kPa) PDMS, stiff (140 kPa) PDMS, or tissue culture plastic (TCP, >1 GPa). Surprisingly, CMs plated on TCP showed a higher overall chromatin enrichment at the nuclear periphery compared to cells on either PDMS substrates (**Figure 3.4a-c**) on day two. However, on day four peripheral enrichment on stiff substrates declined and CMs on soft PDMS showed a higher peripheral accumulation of overall chromatin compared to both stiff PDMS and TCP (1.76 vs. 1.12 and 1.12). In accordance, H3K9me3-marked chromatin was equally enriched for CMs on any substrate on day two, whereas on day four enrichment was higher on soft PDMS compared to both stiffer substrates and was higher for stiff PDMS compared to TCP (2.20 vs. 1.87 vs. 1.25). While there was no difference in enrichment on day two, CMs on soft PDMS had higher H3K9me3 intensities at any distance compared to cells on stiffer substrates (**Figure 3.4b**) in accordance with decreased expression of H3K9 methyltransferases observed on stiff PDMS (**Figure 3.2c**). H3K27me3-marked chromatin was slightly more enriched for CMs on stiff PDMS on day two compared to cells on soft PDMS. After four days, overall enrichment of H3K27me3-modified chromatin increased for all conditions and was highest in cells plated on the soft substrates; however, H3K27me3 enrichment was higher compared to overall chromatin on stiff substrates similar to observations in non-contractile CFs. Substrate stiffness moderately affected chromatin organization in CFs with peripheral enrichment being low for overall and H3K9me3-marked

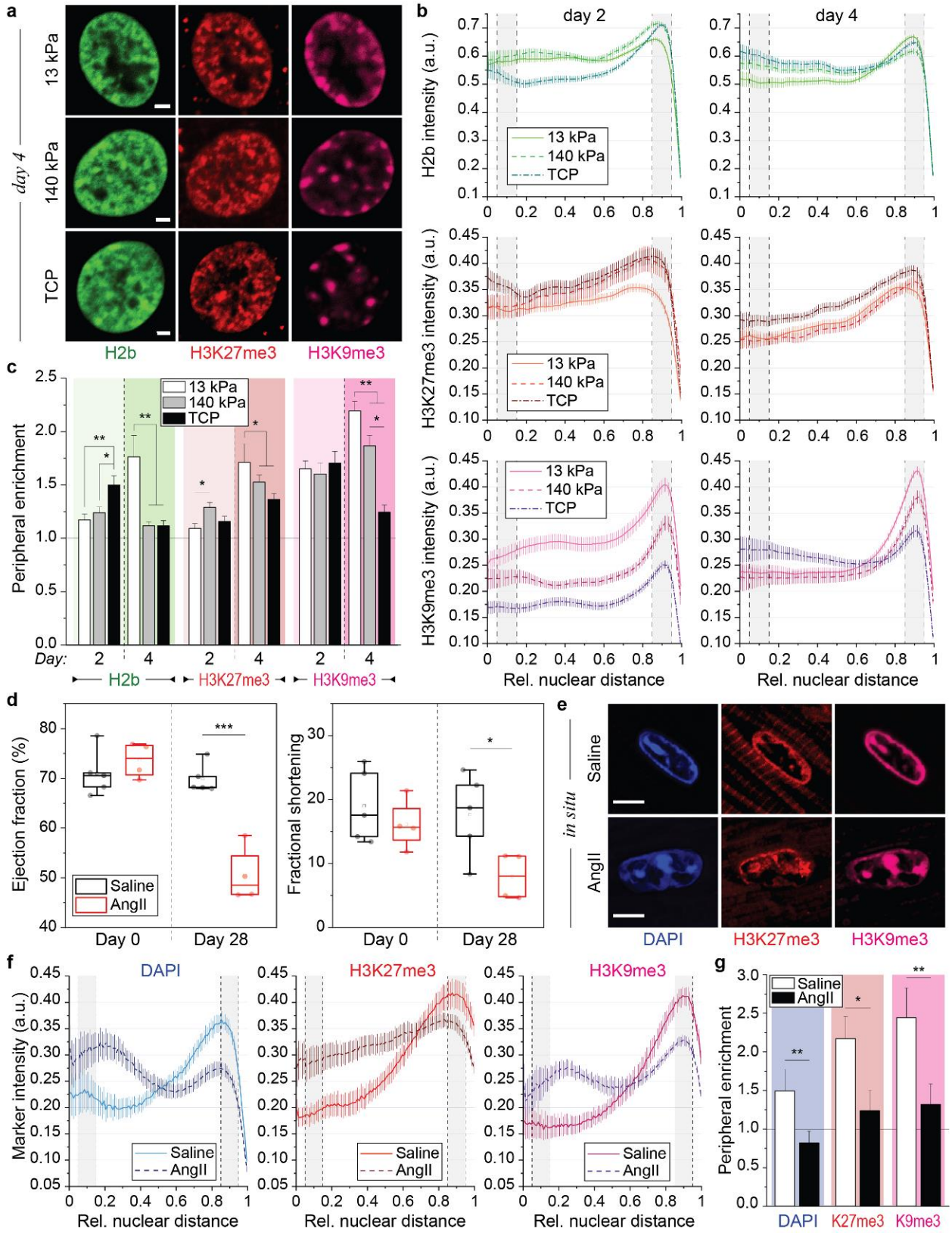
a
day 4
13 kPa
140 kPa
TCP
H2b
H3K27me3
H3K9me3
b
day 2
day 4
H2b intensity (a.u.)
H3K27me3 intensity (a.u.)
H3K9me3 intensity (a.u.)
13 kPa
140 kPa
TCP
Rel. nuclear distance
c
Peripheral enrichment
13 kPa
140 kPa
TCP
Day:
H2b
H3K27me3
H3K9me3
d
Ejection fraction (%)
Fractional shortening
Saline
AngII
Day 0
Day 28
e
in situ
Saline
AngII
DAPI
H3K27me3
H3K9me3
f
Marker intensity (a.u.)
DAPI
H3K27me3
H3K9me3
Saline
AngII
Rel. nuclear distance
g
Peripheral enrichment
Saline
AngII
DAPI
K27me3
K9me3

Figure 3.4. Chromatin reorganization is inhibited in embryonic CMs cultured on stiff substrates in vitro and abrogated in adult CMs during hypertrophy *in vivo*. a) Embryonic cardiac cells were isolated from (E)18.5 H2b-eGFP embryo hearts and cultured on either soft (13 kPa) PDMS, stiff (140 kPa) PDMS or TCP for two or four days after which nuclei were stained for H3K27me3 and H3K9me3 as well as actin to distinguish CMs from CFs. **b)** CM nuclei were evaluated for peripheral enrichment of overall chromatin (H2b) or epigenetically marked chromatin using a custom MATLAB code that analyzed marker intensity with respect to its relative distance to the nuclear center (0=center, 1=periphery). Gray areas indicate center and peripheral bin; SEM; n≥60 from 5 exp. **c)** Enrichment scores for each chromatin marker were calculated as the quotient of intensity of the peripheral bin (0.85-0.95) divided by the center bin (0.05-0.15). Enrichment of overall and H3K9me3-marked chromatin was abrogated on day four in nuclei of cells plated on stiff PDMS and TCP compared to soft PDMS. Note: 13 kPa data same as CM data in Figure 3.3d; SEM; n≥60 from 5 exp.; 1W-ANOVA: * $p<0.05$, ** $p<0.01$, *** $p<0.001$. **d)** Mice treated with angiotensin II (AngII, n=4), to induce cardiac hypertrophy, showed reduced ejection fraction and fractional shortening after 28 days of treatment compared to day 0, while saline receiving control mice (n=5) showed no difference; T-test: * $p<0.05$, *** $p<0.001$. **e)** After 28 days, hearts were harvested and stained for H3K27me3 and H3K9me3. DAPI was used as DNA counterstain. **f, g)** Immunostained cardiac sections of hypertrophic (AngII) or control mice (Saline) were analyzed for peripheral enrichment of overall chromatin (DAPI) or epigenetically marked chromatin using a custom MATLAB code and enrichment scores were calculated. Enrichment of overall and methylated chromatin was abrogated in cardiac nuclei of hypertrophic mice while control mice showed a mature cardiac phenotype; SEM; n≥40 from 4 (AngII) or 5 (saline) exp.; T-test: * $p<0.05$, ** $p<0.01$. All scales=5 μm.

chromatin and high for H3K27me3-modified chromatin throughout the four-day culture period (**Extended Figure 3.4a-c**), suggesting that CMs are more sensitive to substrate stiffness with regard to chromatin reorganization.

Hypertrophy leads to an increase in cardiac stiffness and CM dedifferentiation[4,5]. To validate our findings *in vivo*, we analyzed CM nuclei in mice that received angiotensin II (AngII) for 28 days to induce hypertrophy. Control mice received saline over the same period. Reduction in ejection fraction and fractional shortening during the treatment period confirmed cardiac

performance decline in mice receiving AngII, but not saline (**Figure 3.4d**). CM nuclei of hypertrophic mice showed reduced enrichment of overall (DAPI, 0.82 vs. 1.49), H3K27me3 (1.24 vs. 2.17) and H3K9me3-marked chromatin (1.32 vs. 2.44, **Figure 3.4e-g**, **Extended Figure 3.4d**) similar to CM nuclei cultured on stiff substrates *in vitro*. Together these results further supported a link between H3K9 trimethylation and chromatin reorganization during CM differentiation and suggested that mechanical environments play an important role to establish and retain the nuclear phenotype of adult CMs.

3.2.5. LINC Complex Disruption Inhibits Reorganization of H3K9 Methylated Chromatin in Embryonic CMs, but Does Not Regulate Histone (De)Methylase Expression

We observed enrichment of H3K9me3-marked chromatin in contractile CMs, but not in non-contractile CFs. This enrichment was inhibited in stiffened environments that lead to a reduction in CM contractility[28]. In accordance, analysis of nuclear deformation recorded during CM contraction showed that bulk linear strain and translational movement of nuclei were reduced in cells plated on stiff PDMS and TCP over the four-day culture period (**Extended Figure 3.5a**). CM nuclei are connected to the Z-disks of myofibrils via LINC complexes[13], which are crucial for nuclear mechanotransduction[14] and cardiac development[13,16,17]. To further investigate the link between nuclear deformation and chromatin reorganization, we disrupted LINC complexes in embryonic CMs by overexpressing a truncated nesprin-3 protein that contained the transmembrane and KASH (Klarsicht, ANC-1, Syne Homology) domain (Δsyne-K3) but lacked cytoskeleton binding domains (**Figure 3.5a**). Because KASH domains are highly conserved between species and nesprins, this construct competes with all nesprin isoforms for SUN connections[47–49]. The control vector expressed a protein that was identical to Δsyne-K3 but lacked the KASH domain

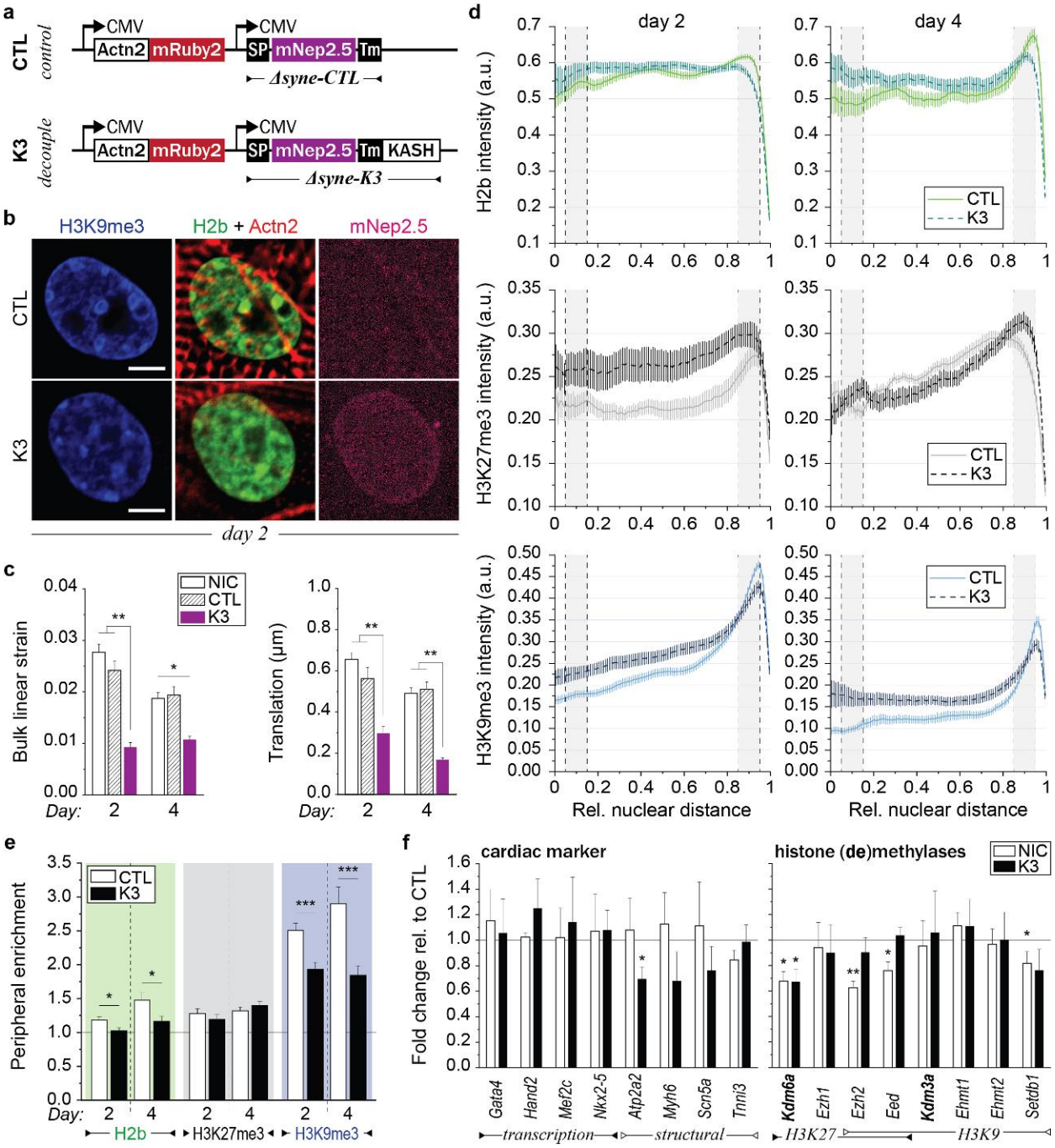

Figure 3.5. LINC complex disruption abrogates rearrangement of H3K9 methylated chromatin in CMs but does not affect epigenetic enzyme expression. Embryonic cardiac cells were isolated from (E)18.5 H2b-eGFP embryo hearts and cultured on soft (13 kPa) PDMS substrates. **a)** Illustration of adenoviral vectors for LINC complex disruption. The decoupling vector (K3) expressed a truncated nesprin-3 composed of the transmembrane (TM) and the KASH domain tagged with mNeptune2.5 (mNep2.5) to track nuclear membrane integration.

The control vector (CTL) lacked the KASH domain necessary for binding to SUN within LINC complexes. Fluorescently tagged α-actinin 2 (*Actn2*) was expressed to identify infected CMs. **b)** Cells were infected with either vector on day one and stained for H3K9me3 (or H3K27me3, see Extended Figure 3.5c) on day two (shown) or day four. The truncated nesprin construct integrated successfully into the outer nuclear membrane of infected CMs (mNep2.5) while no distinct localization was observed for the control vector. Myofibril formation was disrupted in decoupled CMs, particularly around the nucleus, which indicated successful decoupling of nuclei from the cytoskeleton (see also Extended Figure 3.5d); scale=5 µm. **c)** Image series of nuclei during CM contractions were recorded on day two (24h post infection) and day four and bulk linear strain and translational movement of nuclei were determined. Decoupled nuclei (K3, n=32) showed lower bulk linear strain and translational movement compared to cells infected with the control vector (CTL, n=32) or non-infected control cells (NIC, n=67); SEM; from 4 exp.; 1W-ANOVA: * $p<0.05$, ** $p>0.01$. **d, e)** Infected cells were stained for H3K9me3 or H3K27me3 on day two or four and peripheral enrichment of chromatin was analyzed using a custom MATLAB code. Decoupled cells (K3) showed abolished enrichment of overall and H3K9me3-marked chromatin compared to infected control cells (CTL) while H3K27me3-marked chromatin was similarly enriched; SEM; n=35 from 3 exp.; T-test: * $p<0.05$, *** $p<0.001$. **f)** Gene expression analysis of decoupled (K3) or non-infected control cells (NIC) compared to infected control cells (CTL). Expression of structural, but not transcriptional, cardiac genes was reduced in decoupled cells, while expression of histone methylating and demethylating genes remained largely unchanged except for a decrease of *Kdm6a*; SD; n=4; T-test: * $p<0.05$, ** $p<0.01$.

needed for LINC complex integration (Δsyne-CTL). Both vectors also expressed fluorescently tagged α-actinin 2 to identify infected cells.

Cardiac cultures were plated on soft (13 kPa) PDMS and infected on day one of culture. CMs that successfully integrated Δsyne-K3 at the nuclear border 24 hours after infection (day 2) had disorganized sarcomere fibers, particularly around the nucleus (**Figure 3.5b, Extended Figure 3.5b**), diminished localization of nesprin-1 at the nuclear periphery (**Extended Figure 3.5b**), and decreased nuclear bulk linear strain and translational movement during contraction (**Figure 3.5c**), all of which indicated successful LINC complex disruption. Enrichment towards

the nuclear border was significantly impaired for overall (H2b) and H3K9me3-modified chromatin in decoupled CMs compared to control cells, while H3K27me3 showed no distinct difference in enrichment (**Figure 3.5b-e and Extended Figure 3.5c**). Notably, overall H3K9me3 intensities were similar between decoupled and control cells, while H3K27me3 intensities were slightly elevated after decoupling (**Figure 3.5e**) similar to results on stiff substrates. RT-qPCR analysis revealed that gene expression of H3K9 and H3K27 histone (de)methylases was largely unchanged in decoupled cells, except for the downregulation of H3K27 demethylase *Kdm6a* (**Figure 3.5f**), suggesting that LINC-associated nuclear mechanosensitive pathways do not regulate the expression of epigenetic mediators. Expression in non-infected control cells (NIC) was altered compared to infected control cells, indicating that adenovirus transfection affected the expression of epigenetic enzymes as previously reported[50]. In addition to epigenetic modifiers, decoupling also did not affect the expression of cardiac-specific transcription factors while structural cardiac markers were partially downregulated. Together these results showed that the disruption of LINC complex connections from the cytoskeleton to the nucleus inhibited the reorganization of H3K9me3-modified chromatin in CMs but did not affect the expression of cell-fate mediators such as transcription factors or epigenetic enzymes.

3.2.6. H3K9 Trimethylated Chromatin Is Co-Localized with Myofibrils in Embryonic CMs

We observed that the reorganization of H3K9me3-modified chromatin towards the nuclear periphery was inhibited for CMs in stiff environments and after LINC complex disruption, both of which reduced nuclear deformation, which suggested a potential mechanosensitive feedback between myofibrils and the nucleus. Analyzing the shortening of myofibrils of CTL infected CMs via α-actinin 2-mRuby2 expression further validated that CM contractility was abrogated on stiff (140 kPa) compared to soft (13 kPa) PDMS as overall sarcomere (S) and A-band (A) shortening

were reduced by more than half (-0.171 vs. -0.077 µm, -0.185 vs. -0.060 µm), and Z-disks (Z) went from extending to shortening (0.015 vs. -0.032 µm; **Figure 3.6a-c**). In accordance with abrogated Z-disk extension, stretch-induced tyrosine-410 phosphorylation of p130Cas[51], a mechanosensitive focal adhesion protein[52] found within Z-disk lattice in CMs[53], was reduced on stiff PDMS as well (**Extended Figure 3.2b**). Contractility was also abrogated in decoupled CMs infected with K3, albeit to a lesser extent than CMs on stiff PDMS (**Figure 3.6c**), which highlighted the role of LINC complexes in myofibril formation as recently reported[54].

To further inquire whether there is a direct association of H3K9me3-marked chromatin with myofibrils, we quantified the relative overlap of different chromatin markers with myofibrils in CMs cultured for four days on soft (13 kPa) PDMS. In addition to H3K9me3 and actin, cells were stained for serine-2 phosphorylated RNA-polymerase II (RPIIS2) as a control (**Figure 3.6d**) since actively transcribed chromatin[55] is expected to be exclusive with suppressed H3K9me3-modified chromatin. Z-stacks of stained CMs were acquired and basal Z-slices, where myofibrils were primarily located in our *in vitro* cultures (**Extended Figure 3.4a**), were analyzed for marker overlap. A marker co-localization score was calculated by determining the percentage of overlapping pixels between two binarized marker channels normalized over their independent probability to overlap, with a score of 1 representing marker co-localization by chance (see Methods for details). H3K9me3-marked chromatin showed a higher than chance association with actin containing I-bands (1.28) while overall (H2b) and actively transcribed chromatin had lower than chance co-localization scores (0.74 and 0.85, **Figure 3.6e**). The low association with overall chromatin is likely an effect of actin pushing chromatin out of the *z*-plane (**Extended Figure 3.6a**). As expected, transcribed chromatin areas had a high coincidence score for overall chromatin but a

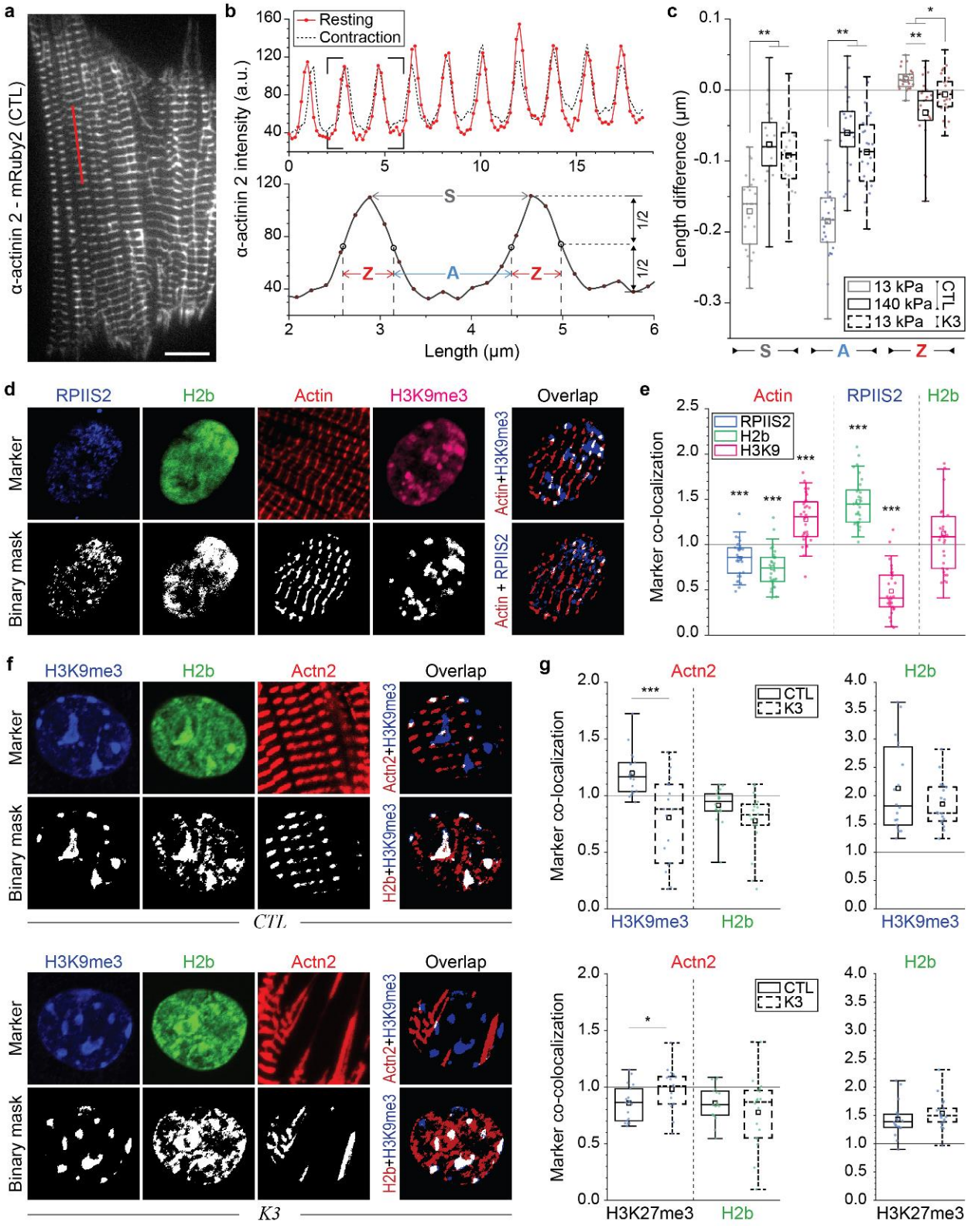
a
α-actinin 2 - mRuby2 (CTL)
b
Resting
Contraction
α-actinin 2 intensity (a.u.)
S
Z
A
1/2
Length (µm)
c
Length difference (µm)
13 kPa
140 kPa
13 kPa
CTL
K3
S
A
Z
d
RPIIS2
H2b
Actin
H3K9me3
Overlap
Marker
Binary mask
Actin+H3K9me3
Actin + RPIIS2
e
Actin
RPIIS2
H2b
RPIIS2
H2b
H3K9
Marker co-localization
f
H3K9me3
H2b
Actn2
Overlap
Marker
Binary mask
Actn2+H3K9me3
H2b+H3K9me3
CTL
K3
g
Actn2
H2b
CTL
K3
Marker co-localization
H3K9me3
H2b
H3K27me3

Figure 3.6. Co-localization of H3K9me3-marked chromatin with myofibrils is abrogated in CMs after LINC complex disruption. Embryonic cardiac cells were isolated from (E)18.5 H2b-eGFP embryo hearts. **a)** CMs were infected with the adenoviral decoupling vector K3 or control vector CTL (shown) on day one and image series of myofibril contraction were recorded on day four via fluorescently tagged α-actinin 2; scale=10 µm. **b)** Top: α-actinin 2 intensity profile, as indicated by a red line in a), before (resting) and during contraction. Bottom: Close-up of two intensity peaks. Analysis of intensity profiles was used to determine the difference in length of overall sarcomeres (S), A-bands (A) and Z-disks (Z) during contraction. **c)** Control infected CMs on stiff PDMS (140 kPa, CTL) and decoupled CMs on soft PDMS (13 kPa, K3) showed inhibited contraction as overall sarcomere and A-band shortening as well as Z-disk extension was abrogated compared to control infected CMs on soft PDMS (13 kPa, CTL); n=25 from 5 exp.; 1W-ANOVA: * $p<0.05$, ** $p<0.01$. **d, e)** After four days in culture on soft PDMS, CMs were stained for regions of active transcription (RPIIS2), sarcomeric I-bands (actin) and H3K9me3. Marker channels were binarized and a co-localization score was calculated for each marker pair as the percentage of overlapping pixels divided by their independent probability to overlap (1=chance). H3K9me3-marked chromatin showed above chance associating with actin while regions of active transcription and overall chromatin did not; n=30 from 3 exp.; T-test (HM=1): *** $p<0.001$. **f, g)** CMs on soft PDMS were infected with K3 or CTL on day one and stained for H3K9me3 (shown) or H3K27me3 (Extended Figure 3.6b) on day four to analyze marker overlap. Co-localization of H3K9me3 with α-actinin 2 containing Z-disks (Actn2) was abrogated after LINC complex disruption while co-localization of H3K27me3 was increased; n=18 from 3 exp.; T-test: * $p<0.05$, *** $p<0.001$.

low score for H3K9me3 (1.48 vs. 0.49) while the association of overall chromatin with H3K9me3 did not significantly deviate from chance (1.12, p=0.165).

To further analyze marker co-localization after LINC complex disruption, we infected cardiac cells with the decoupling vector K3, or control vector CTL, on day one and stained for H3K9me3 or H3K27me3 on day four (**Figure 3.6f-i**, **Extended Figure 3.6b**). We observed an above chance coincidence score for H3K9me3-marked chromatin with the Z-disk protein α-actinin 2 (Actn2), which was significantly decreased below chance after decoupling (1.20 vs. 0.81). In

contrast, coincidence scores of H3K27me3 with Actn2 were slightly increased after decoupling (0.86 vs. 0.98), again highlighting the inverse relationship between H3K9me3 and H3K27me3 modifications in CM development. No significant difference in overlap of overall chromatin and Actn2 was observed in either decoupled or control cells; however, both infected groups showed an increased association of H3K9me3 with overall chromatin compared to uninfected cells, again suggesting a potential influence of adenoviral infections on epigenetic regulation. Overall, these findings provided evidence that H3K9me3-marked chromatin is associated with myofibrils in CMs, but only when connected to the nucleus via LINC complexes, further consolidating a link between nuclear mechanosensation and chromatin reorganization.

3.2.7. H3K9 Trimethylated Chromatin Domains are Localized to Intranuclear Subregions with Elevated Tensile Strains During CM Contractions

Our results suggested a link between myofibril-mediated nuclear deformation and peripheral enrichment of H3K9 trimethylated chromatin as well as an association of H3K9me3 with myofibrils. Analysis of CM nuclei during contractions further confirmed this association as dense, H3K9me3-rich heterochromatin clusters had higher translational movement compared to the overall nucleus (**Extended Figure 3.6c**), To investigate the link between nuclear strain and chromatin reorganization in CMs, we performed an in-depth analysis of the strain occupancy for different chromatin types during CM contraction. For that we utilized a recently published method, termed *deformation microscopy*[31,32], which generates high-resolution spatial strain maps from an undeformed template and a deformed target image (**Figure 3.7a**). Image series of nuclear deformations were recorded in contracting CMs on day two after which cells were fixed, stained, and co-registered to chromatin markers. CMs recorded for live imaging were relocated, imaged and the common H2b-GFP channel was used to register intranuclear strain maps with chromatin

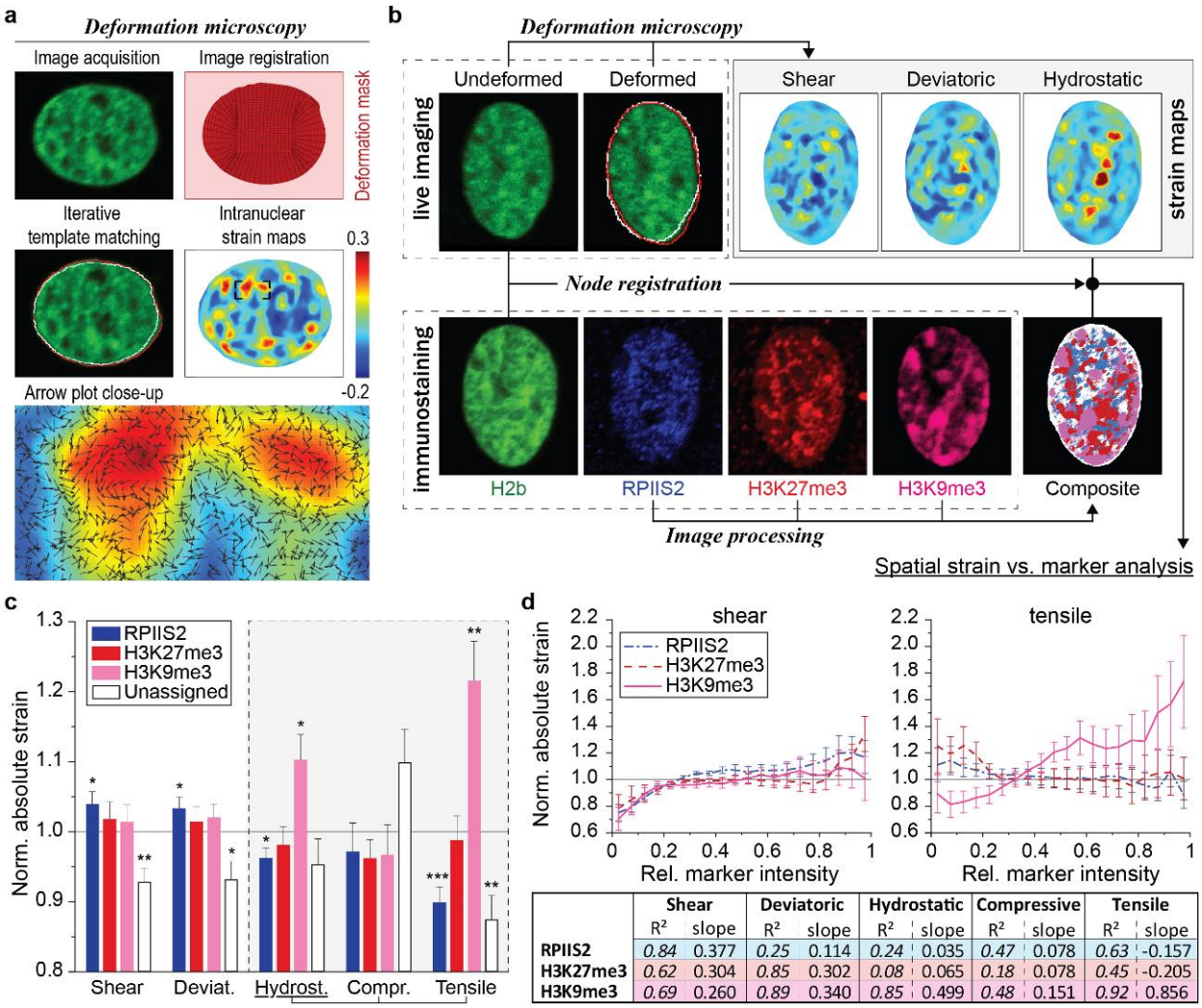

	Shear		Deviatoric		Hydrostatic		Compressive		Tensile	
	R^2	slope	R^2	slope	R^2	slope	R^2	slope	R^2	slope
RPIIS2	*0.84*	0.377	*0.25*	0.114	*0.24*	0.035	*0.47*	0.078	*0.63*	-0.157
H3K27me3	*0.62*	0.304	*0.85*	0.302	*0.08*	0.065	*0.18*	0.078	*0.45*	-0.205
H3K9me3	*0.69*	0.260	*0.89*	0.340	*0.85*	0.499	*0.48*	0.151	*0.92*	0.856

Figure 3.7. H3K9me3-marked chromatin is localized to intranuclear regions with elevated tensile strains during CM contractions. a) Illustration of *deformation microscopy* to generate high-resolution strain maps from image data. Image series of H2b-eGFP CM nuclei were acquired during contraction. Frames of undeformed nuclei during diastolic resting (white outline) were iteratively registered and warped to match nuclear image frames during peak contraction (red outline). Arrow plot shows a close-up of the resulting intranuclear strain map for hydrostatic strains. **b)** Flowchart of spatial strain vs. marker analysis using *deformation microscopy*. Image series of CM nuclei were recorded on day two to calculate intranuclear strain maps. After, CMs were stained for H3K9me3, H3K27me3 or actively transcribed chromatin (RPIIS2), relocated and imaged again. Spatial nodes between both datasets were registered via the common H2b channel and strain occupancy for each marker was analyzed. **c)** Composite analysis of nuclear strains over chromatin assigned to one marker or none of the markers (unassigned, white areas in composite image in b). Strains were normalized to the average of each nucleus. H3K9me3-marked chromatin showed above average association with

tensile hydrostatic strain; SEM; n=20 from 5 exp.; T-test (HM=1): * $p<0.05$, ** $p<0.01$, *** $p<0.001$. **d)** Continuous analysis of intranuclear strains over chromatin marker intensities. Top: Strain vs. intensity plot for shear and tensile hydrostatic strain (see Extended Figure 3.7 for other strains). Bottom: Linear regression summary of strain vs. intensity plots. Highest R^2 and steepest slope were observed for tensile hydrostatic strains over H3K9me3 intensities; SEM.

marker maps to calculate strain values for individual chromatin markers or no marker (unassigned, **Figure 3.7b**). Strain values were normalized to the average strain of each nucleus to enable comparison between cells.

H3K9me3-marked chromatin areas experienced above average absolute hydrostatic (changes in volume) strain magnitudes (1.103), but not shear or deviatoric strains (1.014 and 1.021, **Figure 3.7c**). Interestingly, subdividing hydrostatic strain values into tensile (positive) and compressive (negative) revealed that this trend arose from tensile strains alone (1.216) as no significant difference was observed for compressive hydrostatic strains (0.967) between any of the investigated chromatin features. In contrast, transcribed chromatin regions (RPIIS2) showed lower absolute hydrostatic strain (0.962), a trend that was again augmented for tensile hydrostatic strain (0.899), while no significant difference was observed for H3K27me3 for any of the strains investigated ($p>0.177$). Linear regression analysis of chromatin marker intensities over intranuclear strains further showed the highest degree of correlation ($R^2=0.923$) and the highest slope for tensile strains over H3K9me3-intensities (**Figure 3.7d**, **Extended Figure 3.7a**). Analysis of intranuclear strains over the distance to the nucleus center showed that strains generally declined towards the periphery, excluding the possibility that H3K9me3-marked chromatin and hydrostatic strains simply coincide at the nuclear border (**Extended Figure 3.7b**).

Moreover, analysis of marker intensities over their angle with respect to the nuclear center revealed that H3K9me3 localization peaked within ±30° in the direction of nuclear translation; however, only in nuclei with a tensile loading mode (**Extended Figure 3.8**). In contrast, nuclei with a shortened major axis during contraction showed diminished H3K9me3 occupancy at the angle of nuclear translation while H3K27me3 and RPIIS2 showed no observable trend for any loading mode. Together, these findings provided further support for a link between the reorganization of epigenetically modified chromatin and contraction-mediated nuclear deformation in CMs and connects previous observations of the interactions between environment (substrate stiffness), cell differentiation and cell-type specific nuclear architecture into a new model of nuclear mechanosensation (**Figure 3.8**).

3.3. DISCUSSION

We showed that CMs establish a cell-type specific nuclear architecture during development that is characterized by a relocation of chromatin from the interior to the nuclear periphery. Our findings suggest that tensile strains transferred from myofibrils to the nucleus via LINC complex connections guide the rearrangement of epigenetically suppressed chromatin to the nuclear periphery. Stiff environments, which inhibited contraction and decreased nuclear deformation, or disruption of LINC complexes, profoundly disturbed the establishment of this architecture in embryonic stages or its maintenance in adults. We additionally observed opposing trends for the relocation of H3K9me3 and H3K27me3-modified chromatin as peripheral enrichment of H3K9me3 proceeded that of overall chromatin in embryonic CMs while early relocation of H3K27me3 was indicative for the formation of a non-contractile fibroblast cell-type. Taken together, our results provide further support for a link between nuclear architecture and cell

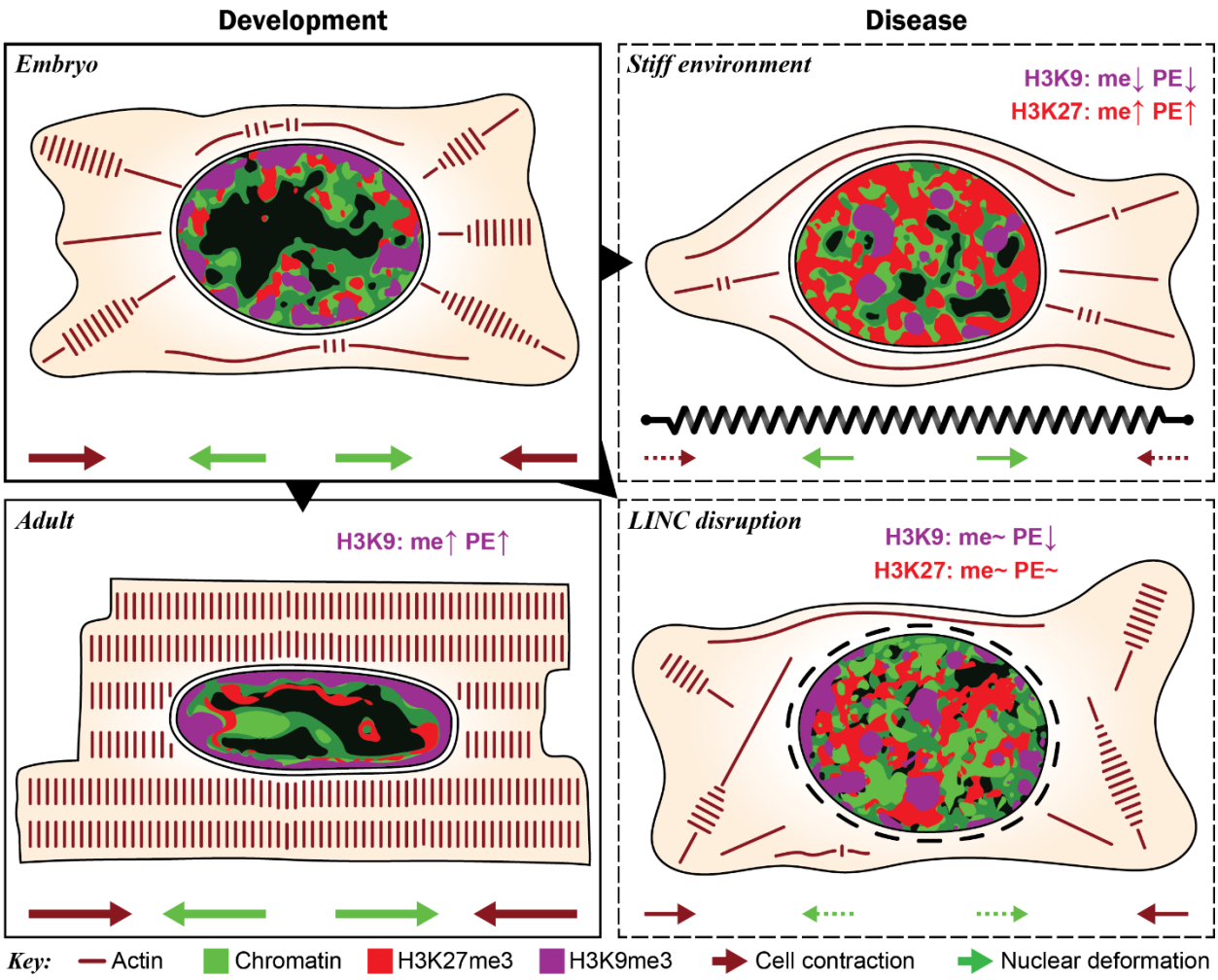

Figure 3.8. Summary of chromatin reorganization and epigenetic regulation during cardiac development and disease. During development, myofibril-mediated cell contraction and subsequent nuclear deformation of embryonic CMs leads to increased H3K9 trimethylation (me) and peripheral enrichment (PE) of H3K9me3-modified chromatin. This presumably stabilizes cardiac gene expression by anchoring suppressed non-cardiac genes to the periphery to prevent reactivation. Stiffening of the cardiac micro-environments inhibits cell contraction and nuclear deformation resulting in increased trimethylation and peripheral enrichment of H3K27 instead of H3K9. Abrogation of nuclear strain transfer through disruption of LINC complexes inhibited chromatin reorganization while regulation of methylation remained largely unchanged, suggesting that nuclear mechanosensation primarily affects chromatin reorganization.

differentiation and suggest that environmental cues can influence cell fate by affecting epigenetic regulation and reorganization of epigenetically modified chromatin (**Figure 3.8**). This work therefore connects previously observed nexuses between substrate properties, cell fate, and nuclear mechanics into one conceptual framework that highlights the role for nuclear mechanosensitive pathways in guiding and stabilizing cell fate determination through spatial chromatin organization. Our data from LINC complex disruption experiments indicated that epigenetic regulation is mediated independently of nuclear strains, hence the interplay between cells and their environment is likely to be a more complex interaction between nuclear and cellular mechanosensors.

3.3.1. Potential Roles of Chromatin Organization in CMs

The observed reorganization of H3K9me3-marked chromatin during CM differentiation might function to stabilize differential gene expression by segregating repressed non-cardiac genes to areas of low activity, like the nuclear envelope[56], to prevent accidental reactivation. In this study, RNAseq and PCR gene expression analysis revealed that H3K9 methylases *Ehmt1*, *Ehmt2*, *Setdb1*, and *Eed* were particularly downregulated on stiff substrates together with cardiac differentiation markers. Recent studies have also shown that the expression of *Ehmt1/2* was decreased in the heart of hypertrophic rats and that the reactivation of cardiac fetal genes such as *Myh7*, *Nppa*, and *Nppb* was associated with the loss of H3K9 methylations at those genes[4]. Furthermore, inhibition of *Ehmt1/2* was sufficient to induce hypertrophy while stabilization of *Ehmt1/2* expression counteracted effects of hypertrophy. Similarly, targeted deletion of H3K9 demethylase *Kdm4a* in the heart led to attenuated hypotrophy in mice[5]. Here we observed that H3K9me3-marked chromatin relocated back towards the nuclear center in mature CMs of hypertrophic mice, supporting the hypothesis that peripheral segregation of chromatin stabilizes its suppression. Interestingly, mechanical decoupling of CM nuclei through LINC complex disruption only

minorly affected the expression of H3K9 (de)methylating enzymes or cardiac transcription factors. It is likely that CMs integrate mechanical signals from different pathways to achieve reliable and robust cell differentiation. One such candidate, identified here via RNAseq and validated through western blot analysis, was p130Cas. This mechanosensitive focal adhesion protein[52] is found within the sarcomeric Z-disk lattice in CMs[53], hence making it a suitable candidate to sense substrate stiffness and influence epigenetic regulation via Rap1 and MAPK signaling (**Extended Figure 3.2**). One study also showed that p130Cas knockout mice die *in utero* due to abnormal heart growth, further linking p130Cas to cardiac development[57].

In addition to stabilizing cardiac gene transcription, the CM nuclear architecture might also have a structural function as has been reported for other types of cells[24,25,58]. The particularly strong accumulation of heterochromatin at the nuclear border might play a protective role as heterochromatin has been shown to increase nuclear rigidity independent of lamins[59]. Chromatin void cavities could provide a protective environment for gene transcription in cells that must endure high and constant cyclic mechanical stresses. This is supported by our observation that nuclear areas of actively transcribed chromatin experienced lower (tensile) hydrostatic strains (**Figure 3.7**).

3.3.2. Potential Role of Nuclear Mechanosensation in CMs

The role of nuclear mechanotransduction has long been debated. While it has been shown that LINC complexes are involved in mechanosensitive gene regulation[60], no distinct mechanism has been reported so far. We provided evidence that nuclear strains transferred from myofibrils via LINC complexes guide the reorganization of H3K9me3-modified chromatin in CMs. In contrast, the formation of a non-contractile CFs was associated with the reorganization of H3K27me3-marked chromatin instead. Our data suggests that CMs may use nuclear deformation as a feedback

for differentiation by consolidating the suppression of H3K9me3-marked non-cardiac genes through peripheral segregation as described above. This mechanism would be beneficial during development as it ensures that only CMs with high contractility mature, while others become fibroblasts or undergo apoptosis. Neurons are known to use similar activity-based mechanisms during development in which their initial state of differentiation is reinforced through functional fidelity[61]. Further investigation will show whether this nuclear-feedback is used by other load-bearing cells as well.

3.3.3. Potential Mechanisms of Mechanosensitive Chromatin Reorganization

How nuclear strains could guide chromatin rearrangement is unclear, but it is likely to involve nuclear motor proteins. For example, nuclear myosin 1 (NM1) has been shown to be necessary for chromatin relocation in response to serum activation[62] and DNA damage[63]. After transport, nuclear envelope transmembrane proteins (NET) could anchor chromatin to the nuclear envelope. NETs have been shown to be tissue specific and might also recognize epigenetic modification of chromatin[20,64,65]. Nuclear motor proteins and NETS are poorly characterized, and more research is needed to understand their role in the nucleus.

The strict association of H3K9me3 with tensile, but not compressive, hydrostatic strains indicated the involvement of stretch-activation. It has been argued that LINC complexes are the nuclear analog to stretch-sensitive focal-adhesions at the cell membrane[66], and research on isolated nuclei has shown that LINC complexes are necessary for stretch-induced nuclear mechanotransduction[14]. Similarly, we found in this study that LINC complexes play a role for chromatin reorganization in CMs. Direct evidence for stretch-sensitivity of LINC complex components (nesprins and SUNs) is lacking; however, and it remains to be seen whether LINC complex or associated proteins (*e.g.* lamins) bear mechanosensitivity. Stretch-activation could

ultimately control motor-protein activity and/or the recruitment of NETs to guide chromatin reorganization using mechanisms similar to focal adhesions[66].

3.4. METHODS

3.4.1. Substrate Fabrication

To mimic native and stiffened mechanical environments of adult cardiac tissue[28,29,67], cell culture dishes were coated with soft or stiff polydimethylsiloxane (PDMS, Sylgard®527, Dow Corning) by using different mixing ratios (base:curing agent): 1:1 (E=12.7 ± 5.0 kPa) and 1:4 (E=139.7 ± 16.2 kPa). To enable live imaging at high magnification using a 100× objective, PDMS was deposited as thin layer (~100 μm) in gridded imaging dishes (μ-Dish 35 mm high Grid-500, ibidi). PDMS coated dishes were degassed under vacuum for 30 min, cured for 1h at 80°C, ozone-activated via corona arc-discharge (30s) and coated with reduced growth factor basement membrane matrix (Geltrex®, Gibco) for 1h at 37°C to provide attachment sites similar to the cardiac basement membrane. PDMS stiffness was determined via AFM using a spherical borosilicate glass tip (diameter=10 μm, stiffness=0.85 N/m), and Young's modulus E was calculated using a Hertz contact model[68].

3.4.2. Cardiac Cell Isolation and Culture

B6.Cg-Tg (HIST1H2BB/EGFP) 1Pa/J mice (Stock No: 006069) were obtained from Jackson Laboratory. All animal procedures were performed following Institutional Animal Care and Use Committee approval. Embryonic mice hearts were harvested 18.5 days post conception. Hearts were minced and incubated in a digestive mix for 30 min at 37°C. Digestive mix contained 2 mg/ml Papain (P4762, Sigma), 500 μg/ml Liberase TM (05401119001, Roche), 5 mM L-Cysteine (C6852, Sigma) and 10 μg/ml DNase-I (D4263, Sigma). Cardiac cells were isolated

through gentle trituration using a 1 ml pipette and cells were cultured on prepared substrates in DMEM-F12 Advanced (Gibco) containing 10% fetal bovine serum (Gibco), 1% penicillin-streptomycin (Gibco) and 25 mM HEPES (Gibco) at a density of 50,000 cells/cm^2. Samples were incubated at 37°C and 5% CO_2[69].

3.4.3. RNAseq Analysis

Total RNA was extracted from cardiac cultures after 4 days on either soft or stiff PDMS (n=4) using the AurumTM Total RNA Mini Kit (Bio-Rad Laboratories). Libraries were constructed by the Purdue Genomics Core Facilities according to standard protocols using TruSeq Stranded mRNA Library Prep Kit (Illumina). Samples were run on a HiSeq 2500 (Illumina) with 200 bp paired-end reads. The filtered Illumina reads were pre-processed and mapped by the Purdue Bioinformatics Core. Sequence quality was assessed using FastQC (v0.11.2) for all samples and quality trimming was done using FASTX toolkit (v0.0.13.2) to remove bases with less than Phred33 score of 30 and resulting reads of at least 50 bases were retained. The quality trimmed reads were mapped against the bowtie2-indexed reference genome downloaded from Ensembl using Tophat (v2.0.14) with default parameters. RNAseq data can be obtained from the GEO database (GSE109405).

Histone subfamily classifications were done using HistoneDB 2.0 (*https://www.ncbi.nlm.nih.gov/research/HistoneDB2.0/*). Pathways with enriched differential gene expression (p<0.2, FPKM>1) were screened using the KEGG database via the functional annotation tool DAVID (*https://david.ncifcrf.gov/*). Analyses of functionally grouped networks was performed using the ClueGO (v2.5.0) app on the Cytoscape (v3.6.0) software tool. Genes associated with the GO term *histone modification* (GO:0016570) were obtained from AmiGO 2

(*http://amigo.geneontology.org/amigo*) and differentially expressed genes ($p<0.2$) in this ontology were used to screen for child GO terms using AmiGO's term enrichment tool (v1.8).

3.4.4. RT-qPCR Analysis

Total RNA was extracted from cardiac cultures after 4 days on either soft or stiff PDMS (n=4) using the AurumTM Total RNA Mini Kit. RNA was reverse transcribed into cDNA via iScriptTM Reverse Transcription Supermix and real-time quantitative PCR was performed with SsoAdvancedTM Universal SYBR® Green Supermix in a CFX96 Touch™ thermocycler (all kits and devices from Bio-Rad Laboratories) using 10 ng of cDNA as input. Primers were custom designed using NCBI primer blast, cross-confirmed in Ensembl gene database and synthesized by IdtDNA. Primers span at least one exon-exon junction. Relative expression change was calculated using the ΔΔCt method. All data was normalized to the reference genes *Gapdh* and *ActB* as established in previous heart studies[70,71]. Primer sequences are listed in **Extended Table 4**.

3.4.5. Immunofluorescence Staining

Cells were fixed in 4% ice-cold PFA for 10min, permeabilized with 1% Triton-X100 in PBS for 15 min and blocked with 10%NGS, 1% BSA in 0.1% PBT (0.1% Tween-20 in PBS) for 60 min. Primary incubation was performed at 4°C overnight in 0.1% PBT containing 1% BSA. Secondary incubation was performed in primary incubation buffer for 45 min (RT) at a dilution of 1:500. Actin was counterstained with Phalloidin conjugated to either Texas Red-X for embryonic tissues and marker co-localization *in vitro* studies (Life Technologies), Alexa Flour 488 for cardiac sections of hypertrophic mice (Life Technologies) or CF405 for all other *in vitro* cultures (Biotium). Primary antibodies: H3K9me3 (ab8898, Abcam, 1:800), H3K27me3 (ab6002, Abcam, 1:200), RNA polymerase II CTD repeat YSPTSPS phospho S2 (ab24758, Abcam, 1:400) and nesprin-1 (ab24742, Abcam, 1:500).

3.4.6. Tissue Sectioning and Staining

After harvest, tissues were washed in PBS and fixed in 4% PFA at 4°C overnight. Tissue were washed again in PBS, embedded in 6% agarose and sectioned into 100 µm thin slices using a vibratome (VT1000 S, Leica). Tissue sections were further immunostained as described above.

3.4.7. Analysis of Chromatin Marker Occupancy

Image stacks of immunostained nuclei were recorded on a Nikon A1R confocal microscope using a 60× oil immersion objective. A custom MATLAB code was used to calculate the intensity of each chromatin marker with respect to distance of the nuclear border. Briefly, the H2b-eGFP image stack was used to determine the nuclear border and the nuclear center for each nucleus. For each pixel, the distance to the nuclear center was calculated and histogram-normalized image intensities for each marker channel were collected. Nuclear center distances were normalized to the maximum distance of each corresponding center trajectory resulting in a normalized center distance of 0 for the center and 1 for the nuclear periphery for any nuclear geometry. Normalized nuclear center distances were then binned in 0.01 steps (100 bins total) and marker intensities for pixels in the same bin were averaged for each nucleus. MATLAB code is available from the corresponding author upon request.

3.4.8. Hypertrophic Animal Model

Female, 12 weeks old C57BL/6J mice (Jackson Laboratory) were surgically implanted with a mini-osmotic pump (ALZET Model 2004, DURECT Corporation) to deliver either saline (n=5) or AngII (n=4) at a rate of 0.28 µL/h for 28 days. For the AngII group, the AngII powder was dissolved in saline to provide a 1000 ng/kg/min infusion rate. Mice were monitored at baseline and again on day 28 post-surgery using a high resolution, small animal ultrasound imaging system (Vevo2100 Imaging System, FUJIFILM VisualSonics) to assess cardiac size and function[72]. After

28 days, mice were euthanized, hearts harvested, and the left ventricles were cut along the transverse plane. Tissue sectioning and staining was performed as described above. All animal procedures were approved by the Institutional Animal Care and Use Committee.

3.4.9. Small Animal Ultrasound Imaging

A high resolution, small animal *in vivo* ultrasound imaging system was used to assess cardiac size and function at baseline and again on day 28 post-surgery. Briefly, anesthetized mice (1-3% isoflurane) were positioned supine on a heated stage. Body temperature was monitored using a rectal probe, while cardiac and respiratory rates were monitored using stage electrodes. Hair on the thoracic region was removed with depilatory cream and ultrasound gel was applied. A linear array transducer (MS550D) was used to view both the long and short axes of the heart. Two-dimensional cine loops in brightness mode (B-mode) and motion mode (M-mode) were collected. In addition, high temporal resolution cine loops were acquired using ECG-gated Kilohertz Visualization (EKV). These images were analyzed with Vevo2100 software (FUJIFILM VisualSonics) to determine ejection fraction and fractional shortening.

3.4.10. Adenovirus Generation and Transduction

Adenoviral vectors for LINC disruption experiments were generated as described before[73] using the AdEasy vector system. The decoupling and control construct were assembled via Gibson cloning using NEBuilder® HiFi DNA Assembly Master Mix (New England Biolabs). The decoupling construct contained the C-terminal end of the nesprin-3 gene (*Syne3*) including the transmembrane (Tm) and the KASH domain. The N-terminus was replaced by a far-red fluorescence protein (mNeptune2.5) for visualization and a signal peptide (SP, from *Tor1a*) for membrane integration. The control construct was identical to the decoupling construct but lacked the KASH domain. AdEasy plasmids were a gift from Leslie Leinwand. pcDNA3-mNeptune2.5

and pcDNA3-mRuby2 were a gift from Michael Lin (Addgene, #51310 and #40260)[74]. Embryonic cardiac cells were infected at day one with 100×MOI, as determined by plaque assay, and further analyzed at day two or day four as described above. Plasmid maps and stab cultures of adenoviral transfer plasmids can be obtained from Addgene (CTL: #122243 and K3: #122242).

3.4.11 Nuclear Bulk Linear Strain and Translation

CMs cultured on soft PDMS, stiff PDMS or TCP or infected with K3 or CTL on day one on soft PDMS and image series of nuclei (6.4 fps) were recorded during contraction on day two or four using an inverted epi-fluorescence microscope (Nikon Ti-Eclipse) with a 100× oil immersion objective (0.16 μm/pix) and an iXon^{EM}+ EMCCD camera (Andor). A custom MATLAB code was written that tracked nuclear outlines during image series. Bulk linear strain was calculated as the average of the differential length of major and minor axis while translation was determined via centroid tracking. For each nucleus, the results of four contraction cycles were averaged for one data point. MATLAB code is available from the corresponding author upon request.

3.4.12. Sarcomere Shortening Analysis

CMs cultured on soft or stiff PDMS were infected with K3 or CTL on day one and image series (6.4 fps) of myofibril contractions were recorded on day four using an inverted epi-fluorescence microscope (Nikon Ti-Eclipse) with a 100× oil immersion objective (0.16 μm/pix) and an EMCCD camera (iXon^{EM}+, Andor) via expression of α-actinin 2-mRuby2. A custom written MATLAB code was used to quantify the length of different sarcomere features before and during contraction from α-actinin 2 fluorescence intensity profiles stretching 15-20μm and containing 8-12 α-actinin 2-rich Z-disks (**Figure 3.6a**). Overall sarcomere lengths were determined as the distance between neighboring peaks. Data points between peaks were

interpolated (cubic) to achieve sub-pixel resolution and the mid-intensity between a maximum (peak) and a minimum (valley) was used to separate the Z-disks from A-bands for each segment (**Figure 3.6b**). Values along one intensity profile were averaged and the difference in length before and during contraction for each sarcomere feature was calculated. A total of 25 intensity profiles were analyzed for each substrate. MATLAB code is available from the corresponding author upon request.

3.4.13. Marker Co-Localization Analysis

Cardiac cultures were immunostained after four days on soft PDMS and image *z*-stacks were acquired on a Nikon A1R confocal microscope using a 60× oil immersion objective. *In vitro*, myofibrils primarily intersected with nuclei on the basal side (**Extended Figure 3.6**). A custom MATLAB code was used to calculate marker co-localization scores for basal nuclear z-slices. For that, marker channels were binarized (0 or 1) using accumulated histogram thresholding with cut-off values of 90% for actin and α-actinin 2, 95% for H2b, and 85% for H3K9me3 and H3K27me3 to achieve equal representation of true pixels (=1) amongst channels. A marker co-localization score for any marker pair was calculated as the percentage of overlapping pixels (number of pixels that are true for both channels divided by total number of pixels in the nucleus) divided by the probability that positive pixels overlap by chance (independent probability): co-localization score = $p(A \cap B) / [p(A) \times p(B)]$ with A {marker channel 1=true} and B {marker channel 2=true}. MATLAB code is available from the corresponding author upon request.

3.4.14. Spatial Intranuclear Strain vs. Chromatin Marker Analysis

After two days on soft PDMS, image series (7.2 fps) of nuclear deformation during CM contractions were recorded on a Nikon A1R confocal microscope using a 60× oil immersion objective (0.14 μm/pix) via the expression of H2b-eGFP. Nuclear frames during diastolic rest and

during peak contraction were used as template and target, respectively, to generate high-resolution intranuclear strain maps via *deformation microscop*y developed previously[31,32]. The location of each cell was recorded through the use of gridded imaging dishes (µ-Dish 35 mm high Grid-500, ibidi). After live imaging, cells were fixed, immunostained for chromatin markers, relocated and image color stacks were recorded again on a confocal microscope. To compensate for changes in nuclear morphology during fixation, intranuclear strain maps and chromatin marker maps were aligned via the registration function of the *deformation microscopy* algorithm using the common H2b channel in both datasets and marker channels were interpolated (cubic) to match strain resolution.

A custom written MATLAB code was used to analyze nuclear strains over chromatin marker intensities. For non-continuous analysis (**Figure 3.7c**), marker channels were binarized using accumulative histogram thresholding with a cut-off value of 75% and strain values for true marker pixels were averaged. A composite map was generated by assigning pixels to the marker with the highest normalized intensity value, if multiple channels were true, or labeled as unassigned if no channel was true.

For angular analysis, the angle of each pixel with respect to the nuclear center was obtained with the angle of nuclear translation during contraction set to 0°. Nuclear translation angle was determined as the angle of the trajectory that connected the nuclear centers before (resting) and during CM contraction (**Extended Figure 3.8**). Pixels were binned in 1° steps and marker intensities for each channel were averaged for each bin. Areas represent SEM between cells. MATLAB codes are available from the corresponding author upon request.

3.4.15. Western Blot Analysis

After four days on soft or stiff PDMS substrates, cardiac cells were lysed in tris-triton buffer containing a protease/phosphatase inhibitor mix (Sigma). Protein concentrations were determined using Bradford Assay Kit 1 (Bio-Rad) and 30µg of protein were loaded onto 8% SDS-Page Gels (Thermo Scientific), transferred to PVDF membranes (EMD Millipore) and immunodetected using an ECL substrate kit (Life Technologies) and a PXi imaging system (Syngene). Densitometric quantification was performed using ImageJ (v1.50e). Primary antibodies: p130Cas (13846, Cell Signaling), phospho-p130Cas Tyr410 (4011, Cell Signaling) and Gapdh (5174, Cell Signaling).

3.4.16. Statistical Analysis

One-way (1W) or two-way (2W) ANOVA with Tukey's Honestly Significant Difference post hoc test or two-tailed t-test analysis was performed to evaluate statistical significance using JMP Pro12 software (SAS Institute). Displayed error (SD=standard deviation, SEM=standard error of the mean), number of individual data points (n), number of independent experiments (exp., if different from n), hypothetical population mean (HM, for single sample t-test), significances and statistical tests used are indicated in the figure captions. Boxplots are shown with all data points overlaid, a square representing the mean and whiskers indicating the data span under the exclusion of outliers (coefficient=3).

3.5. ACKNOWLEDGEMENTS

We are grateful to Leslie Leinwand and Stephen J. Langer for providing materials and technical assistance for the generation of adenoviruses. We also thank Michael Rafuse for technical assistance regarding tissue sectioning. This work was supported in part by grants to C.P.N.: NIH R01 AR063712, NIH R21 AR066230, and NSF CMMI CAREER 1349735.

3.6. EXTENDED DATA

3.6.1. EXTENDED TABLES

Extended Table 3.1. Expression of histone variants in cardiac cultures on cultured on soft or stiff substrates. Embryonic cardiac cells were plated on soft (13 kPa) or stiff (140 kPa) PDMS for four days after which total RNA was harvested to perform RNAseq analysis. Averaged expression (FPKM: Fragments Per Kilobase of transcript per Million mapped reads) for each substrate group, as well as fold changes and p-values between substrates, of previously annotated mouse histone variants[36] are shown; * indicates canonical (generic) H1 variants.

Gene	Ensembl ID	Family	Variant	FPKM 13 kPa	FPKM 140 kPa	Fold Change	*p*-Value
Hist1h1a	ENSMUSG00000049539	H1	H1.1*	32.92	22.83	0.694	0.595
Hist1h1c	ENSMUSG00000036181	H1	H1.2*	75.57	55.23	0.731	0.413
Hist1h1d	ENSMUSG00000052565	H1	H1.3*	65.25	35.79	0.549	0.350
Hist1h1e	ENSMUSG00000051627	H1	H1.4*	66.10	43.53	0.658	0.386
Hist1h1b	ENSMUSG00000058773	H1	H1.5*	41.15	26.51	0.644	0.531
H1f0	ENSMUSG00000096210	H1	H1.0	60.85	51.81	0.851	0.015
H1fx	ENSMUSG00000044927	H1	H1.X	0.14	0.01	0.088	0.239
Gm6970	ENSMUSG00000091230	H1	H1.11	0.43	0.06	0.150	0.306
Hist1h1t	ENSMUSG00000036211	H1	TS H1.6	0	0.80	-	-
H1fnt	ENSMUSG00000048077	H1	TS H1.7	0	0	-	-
H1foo	ENSMUSG00000042279	H1	OO H1.8	0	0	-	-
Hils1	ENSMUSG00000038994	H1	TS H1.9	0	0	-	-
Hist1h2ab	ENSMUSG00000061615	H2A	canonical	14.08	3.38	0.240	0.335
Hist1h2ac	ENSMUSG00000069270	H2A	canonical	7.33	1.20	0.163	0.286
Hist1h2ad	ENSMUSG00000071478	H2A	canonical	5.11	1.05	0.205	0.370
Hist1h2ae	ENSMUSG00000069272	H2A	canonical	4.83	0.77	0.160	0.314
Hist1h2ag	ENSMUSG00000069301	H2A	canonical	6.01	1.27	0.211	0.379
Hist1h2ai	ENSMUSG00000071516	H2A	canonical	5.27	0.80	0.153	0.312
Hist1h2an	ENSMUSG00000069309	H2A	canonical	3.65	0.41	0.112	0.330
Hist1h2ao	ENSMUSG00000094248	H2A	canonical	6.25	1.15	0.184	0.356
Hist1h2ap	ENSMUSG00000094777	H2A	canonical	6.26	1.05	0.169	0.351
Hist1h2af	ENSMUSG00000061991	H2A	canonical	3.94	0.92	0.234	0.286
Hist1h2ah	ENSMUSG00000069302	H2A	canonical	4.99	0.78	0.156	0.314
Hist1h2ak	ENSMUSG00000063021	H2A	canonical	14.40	1.52	0.106	0.274
Hist1h2al	ENSMUSG00000091383	H2A	canonical	0.38	0.07	0.194	0.143
Hist2h2aa1	ENSMUSG00000064220	H2A	canonical	37.72	10.72	0.284	0.314
Hist2h2aa2	ENSMUSG00000063954	H2A	canonical	44.72	13.15	0.294	0.322

Hist2h2ab	ENSMUSG00000063689	H2A	canonical	1.31	0.19	0.144	0.212
Hist2h2ac	ENSMUSG00000068855	H2A	canonical	16.41	4.61	0.281	0.243
Hist3h2a	ENSMUSG00000078851	H2A	canonical	8.28	5.36	0.648	0.151
H2afj	ENSMUSG00000060032	H2A	H2A.J	3.03	2.30	0.761	0.445
H2afx	ENSMUSG00000049932	H2A	H2A.X	8.63	4.77	0.553	0.416
H2afz	ENSMUSG00000037894	H2A	H2A.Z	69.22	75.76	1.094	0.638
H2afv	ENSMUSG00000041126	H2A	H2A.Z	12.45	11.91	0.956	0.741
H2afy	ENSMUSG00000015937	H2A	macro H2A	22.42	24.38	1.087	0.603
H2afy2	ENSMUSG00000020086	H2A	macro H2A	9.54	9.11	0.954	0.735
H2afy3	ENSMUSG00000101167	H2A	macro H2A.3	0	0	-	-
Hist1h2aa	ENSMUSG00000060081	H2A	TS H2A.1	0	0	-	-
H2al1a	ENSMUSG00000100626	H2A	H2A.L	0	0	-	-
H2al1c	ENSMUSG00000096097	H2A	H2A.L	0	0	-	-
H2al1d	ENSMUSG00000094904	H2A	H2A.L	0	0	-	-
H2al1f	ENSMUSG00000095655	H2A	H2A.L	0	0	-	-
H2al1g	ENSMUSG00000095662	H2A	H2A.L	0	0	-	-
H2al1h	ENSMUSG00000099443	H2A	H2A.L	0	0	-	-
H2al1i	ENSMUSG00000095445	H2A	H2A.L	0	0	-	-
H2al1b	ENSMUSG00000101819	H2A	H2A.L	0	0	-	-
H2al1e	ENSMUSG00000095413	H2A	H2A.L	0	0	-	-
H2al1j	ENSMUSG00000069038	H2A	H2A.L	0	0	-	-
H2al1k	ENSMUSG00000100448	H2A	H2A.L	0	0	-	-
H2al1m	ENSMUSG00000100200	H2A	H2A.L	0.21	0	-	-
H2al1n	ENSMUSG00000078346	H2A	H2A.L	0	0	-	-
H2al1o	ENSMUSG00000061065	H2A	H2A.L	0	0	-	-
H2afb1	ENSMUSG00000062651	H2A	H2A.L	0	0	-	-
H2al2b	ENSMUSG00000095573	H2A	H2A.L	0	0	-	-
H2al2c	ENSMUSG00000094881	H2A	H2A.L	0	0	-	-
Hypm	ENSMUSG00000040456	H2A	H2A.P	0	0	-	-
H2afb2	ENSMUSG00000082482	H2A	H2A.B	0	0	-	-
H2afb3	ENSMUSG00000083616	H2A	H2A.B	0	0	-	-
Gm14920	ENSMUSG00000067441	H2A	H2A.B	0	0	-	-
Hist1h2bb	ENSMUSG00000075031	H2B	canonical	58.66	31.09	0.530	0.330
Hist1h2bc	ENSMUSG00000018102	H2B	canonical	75.02	62.26	0.830	0.547
Hist1h2be	ENSMUSG00000047246	H2B	canonical	8.78	4.93	0.561	0.402
Hist1h2bg	ENSMUSG00000058385	H2B	canonical	54.19	29.79	0.550	0.522
Hist1h2bf	ENSMUSG00000069268	H2B	canonical	12.99	7.59	0.584	0.482
Hist1h2bj	ENSMUSG00000069300	H2B	canonical	31.22	10.63	0.341	0.386
Hist1h2bl	ENSMUSG00000094338	H2B	canonical	25.52	14.71	0.577	0.506

Hist1h2bn	ENSMUSG00000095217	H2B	canonical	58.33	31.99	0.548	0.460
Hist1h2bq	ENSMUSG00000069307	H2B	canonical	6.30	3.45	0.548	0.404
Hist1h2br	ENSMUSG00000069303	H2B	canonical	11.13	5.64	0.507	0.343
Hist1h2bq	ENSMUSG00000069307	H2B	canonical	6.30	3.45	0.548	0.404
Hist1h2br	ENSMUSG00000069303	H2B	canonical	11.13	5.64	0.507	0.343
Hist1h2bh	ENSMUSG00000064168	H2B	canonical	21.22	9.45	0.445	0.396
Hist1h2bk	ENSMUSG00000062727	H2B	canonical	44.56	20.03	0.450	0.345
Hist1h2bm	ENSMUSG00000096807	H2B	canonical	32.08	19.90	0.620	0.483
Hist1h2bp	ENSMUSG00000069308	H2B	canonical	7.24	3.81	0.526	0.264
Hist2h2be	ENSMUSG00000068854	H2B	canonical	0.83	2.17	2.617	0.019
Hist3h2ba	ENSMUSG00000056895	H2B	canonical	1.47	0.95	0.647	0.615
Hist3h2bb	ENSMUSG00000080712	H2B	canonical	1.66	2.26	1.357	0.517
Hist1h2ba	ENSMUSG00000050799	H2B	sperm H2B	0.72	0.47	0.647	0.489
Hist2h2bb	ENSMUSG00000105827	H2B	canonical	0	0	-	-
1700024p04rik	ENSMUSG00000045022	H2B	subH2B	0	0	-	-
H2bfm	ENSMUSG00000048155	H2B	H2B.W	0	0	-	-
Hist1h3a	ENSMUSG00000069265	H3	canonical	13.94	5.18	0.372	0.384
Hist1h3g	ENSMUSG00000099517	H3	canonical	16.82	5.27	0.313	0.279
Hist1h3h	ENSMUSG00000101355	H3	canonical	21.59	6.20	0.287	0.226
Hist1h3i	ENSMUSG00000101972	H3	canonical	39.53	23.30	0.589	0.537
Hist1h3b	ENSMUSG00000069267	H3	canonical	24.57	9.76	0.397	0.341
Hist1h3c	ENSMUSG00000069310	H3	canonical	24.95	10.08	0.404	0.227
Hist1h3d	ENSMUSG00000099583	H3	canonical	17.60	7.91	0.449	0.425
Hist1h3e	ENSMUSG00000069273	H3	canonical	8.85	3.48	0.393	0.241
Hist1h3f	ENSMUSG00000100210	H3	canonical	11.10	4.05	0.365	0.307
Hist2h3b	ENSMUSG00000074403	H3	canonical	9.61	3.37	0.350	0.377
Hist2h3c2	ENSMUSG00000081058	H3	canonical	3.32	1.37	0.412	0.401
H3f3a	ENSMUSG00000060743	H3	H3.3	95.66	94.39	0.987	0.937
H3f3b	ENSMUSG00000016559	H3	H3.3	122.89	130.10	1.059	0.780
Gm6421	ENSMUSG00000094518	H3	H3.3	15.72	10.54	0.670	0.322
Gm10257	ENSMUSG00000096789	H3	H3.3	7.37	5.66	0.767	0.488
Cenpa	ENSMUSG00000029177	H3	cenH3	19.08	21.18	1.110	0.468
H3f3c	ENSMUSG00000082029	H3	H3.5	116.29	102.04	0.877	0.287
Hist2h3c1	ENSMUSG00000093769	H3	canonical	0	0	-	-
Gm12260	ENSMUSG00000080152	H3	TS H3.4	0	0	-	-
Hist1h4a	ENSMUSG00000060093	H4	canonical	34.85	11.56	0.332	0.379
Hist1h4b	ENSMUSG00000069266	H4	canonical	47.65	12.84	0.269	0.247
Hist1h4c	ENSMUSG00000060678	H4	canonical	102.01	32.57	0.319	0.291
Hist1h4d	ENSMUSG00000061482	H4	canonical	124.40	41.41	0.333	0.284
Hist1h4f	ENSMUSG00000069274	H4	canonical	82.80	37.85	0.457	0.317
Hist1h4h	ENSMUSG00000060981	H4	canonical	52.11	18.08	0.347	0.171

Hist1h4i	ENSMUSG00000060639	H4	canonical	4.51	2.49	0.553	0.234
Hist1h4j	ENSMUSG00000067455	H4	canonical	9.82	3.45	0.351	0.310
Hist1h4k	ENSMUSG00000064288	H4	canonical	42.69	21.68	0.508	0.387
Hist1h4m	ENSMUSG00000069306	H4	canonical	77.49	32.80	0.423	0.327
Hist1h4n	ENSMUSG00000069305	H4	canonical	65.29	27.97	0.428	0.340
Hist2h4	ENSMUSG00000091405	H4	canonical	5.75	3.42	0.595	0.446
Hist4h4	ENSMUSG00000096010	H4	canonical	2.34	0.85	0.363	0.139

Extended Table 3.2. KEGG pathway analysis of differentially expressed genes from cardiac cultures plated on soft or stiff PDMS substrates. Global gene expression data from RNAseq analysis was used to screen for pathways with enriched differential gene expression (p<0.2, FPKM>1) using the KEGG database via DAVID. Listed are pathway terms involved in signal transduction cascades, the number of differentially expressed genes, the percentage of differentially expressed genes compared to the total number of genes associated with that pathway as well as p-values and corrected p-value Benjamini-scores obtained via the Benjamini-Hochberg procedure.

Term	Gene count	% total	*p*-value	Benjamini
Signaling pathways regulating stem cell pluripotency	29	1.2	0.0002	0.0650
Rap1 signaling pathway	35	1.4	0.0050	0.2100
Toll-like receptor signaling pathway	20	0.8	0.0055	0.1800
TNF signaling pathway	20	0.8	0.0120	0.3000
MAPK signaling pathway	37	1.5	0.0210	0.2800
PI3K-Akt signaling pathway	48	2	0.0270	0.3200
Adrenergic signaling in cardiomyocytes	24	1	0.0280	0.3100
HIF-1 signaling pathway	18	0.7	0.0310	0.3300
Cholinergic synapse	19	0.8	0.0340	0.3500
cGMP-PKG signaling pathway	26	1.1	0.0370	0.3300
Insulin resistance	18	0.7	0.0500	0.3600
AMPK signaling pathway	20	0.8	0.0520	0.3700
ErbB signaling pathway	15	0.6	0.0530	0.3700
ECM-receptor interaction	15	0.6	0.0580	0.3700
Neurotrophin signaling pathway	19	0.8	0.0650	0.3800
Estrogen signaling pathway	16	0.7	0.0670	0.3800
Wnt signaling pathway	21	0.9	0.0750	0.4000
VEGF signaling pathway	11	0.4	0.0770	0.4000
Hippo signaling pathway	22	0.9	0.0820	0.4100
Jak-STAT signaling pathway	21	0.9	0.0930	0.4300
Calcium signaling pathway	25	1	0.0960	0.4300

Extended Table 3.3. Substrate specificity of differentially expressed histone methylating genes. List of differentially expressed (p<0.2) genes between soft and stiff PDMS, as determined by RNAseq, with the GO term association *histone methylation* (GO:0016571). Shown are substrate specificities for mono (1), di (2), tri (3) or any methylation of the respective target histone residue as obtained from either UniProt or AmiGO database. H3K9 residues were amongst the most prevalent substrates.

Gene	Ensembl ID	Substrate specificity	Source	FC	P-value
Ehmt1	ENSMUSG00000036893	H3K9me1/2	UniProt	0.847	0.0185
Paxbp1	ENSMUSG00000022974	H3K4me2/3	UniProt	0.751	0.0666
Pwp1	ENSMUSG00000001785	H3K20me3	AmiGO	0.860	0.0797
Setdb1	ENSMUSG00000015697	H3K9me3	UniProt	0.823	0.0830
Rtf1	ENSMUSG00000027304	H3K4me3	UniProt	1.127	0.1119
Setd1a	ENSMUSG00000042308	H3K4me	UniProt	0.670	0.1190
Setd1b	ENSMUSG00000038384	H3K4me	UniProt	0.193	0.1573
Eed	ENSMUSG00000030619	H3K9me, H3K27me	UniProt	0.719	0.1687
Arid4b	ENSMUSG00000039219	H3K9me3, H3K20me3	AmiGO	1.158	0.1881

Extended Table 3.4. PCR primers for gene expression analysis.

Gene	Forward	Reward
Gapdh	TGTCAAGCTCATTTCCTGGTATG	GGGATAGGGCCTCTCTTGCT
ActB	GATCAAGATCATTGCTCCTCCTG	AGGGTGTAAAACGCAGCTCA
Gata4	CTCCATGTCCCAGACATTCAGT	GATGCATAGCCTTGTGGGGA
Hand2	CACCAGCTACATCGCCTACC	TCTCATTCAGCTCTTTCTTCCTCT
Mef2c	ACCTCCCAGCTTTGAGATGC	CCATCAGACCGCCTGTGTTA
Nkx2-5	ATTTTACCCGGGAGCCTACG	CAGCGCGCACAGCTCTTTT
Atp2a2	CCGGCTGAAGAAGGAAAAACC	CCACGATTGCATTGGCTACC
Myh6	CTCTGGATTGGTCTCCCAGC	GTCATTCTGTCACTCAAACTCTGG
Scn5a	ATATGTTGAGTACACCTTCACCGC	CGATCACACTGAAGTCTAGCCA
Tnni3	CGTTCTGAGGACTCGTTGCC	TTAAACTTGCCACGGAGGTCA
Kdm6a	TGGAAACGTGCCTTACCTGC	TGAAGCCCCTGAGTGGAGTT
Eed	TGGGCGATTTGATTACAGCCA	GGGTCAGTGTTGTGCATTTGG
Ezh1	TGGATATAGCAAGTCCCCCA	ACATACAGAGCCTTTGCTCCC
Ezh2	TCCATGCAACACCCAACACATA	ACTCCTTAGCTCCCTCCAGAT
Kdm3a	CAGGACAACTGGGACTTGGAG	CCACACACACCTTCAAGTCTTTC
Ehmt1	GCTAAGGGAAGATACACCTATGGC	CACTCTGTTGGTGCCTTCCT
Ehmt2	GAACTCTGGTAGCCTGTCCG	GCTCATCCACAGAGTACGCA
Setdb1	CATACAGCAGCGCAAGAAGC	AGTTAGTCACTTCCCTGGATGC

3.6.2. EXTENDED FIGURES

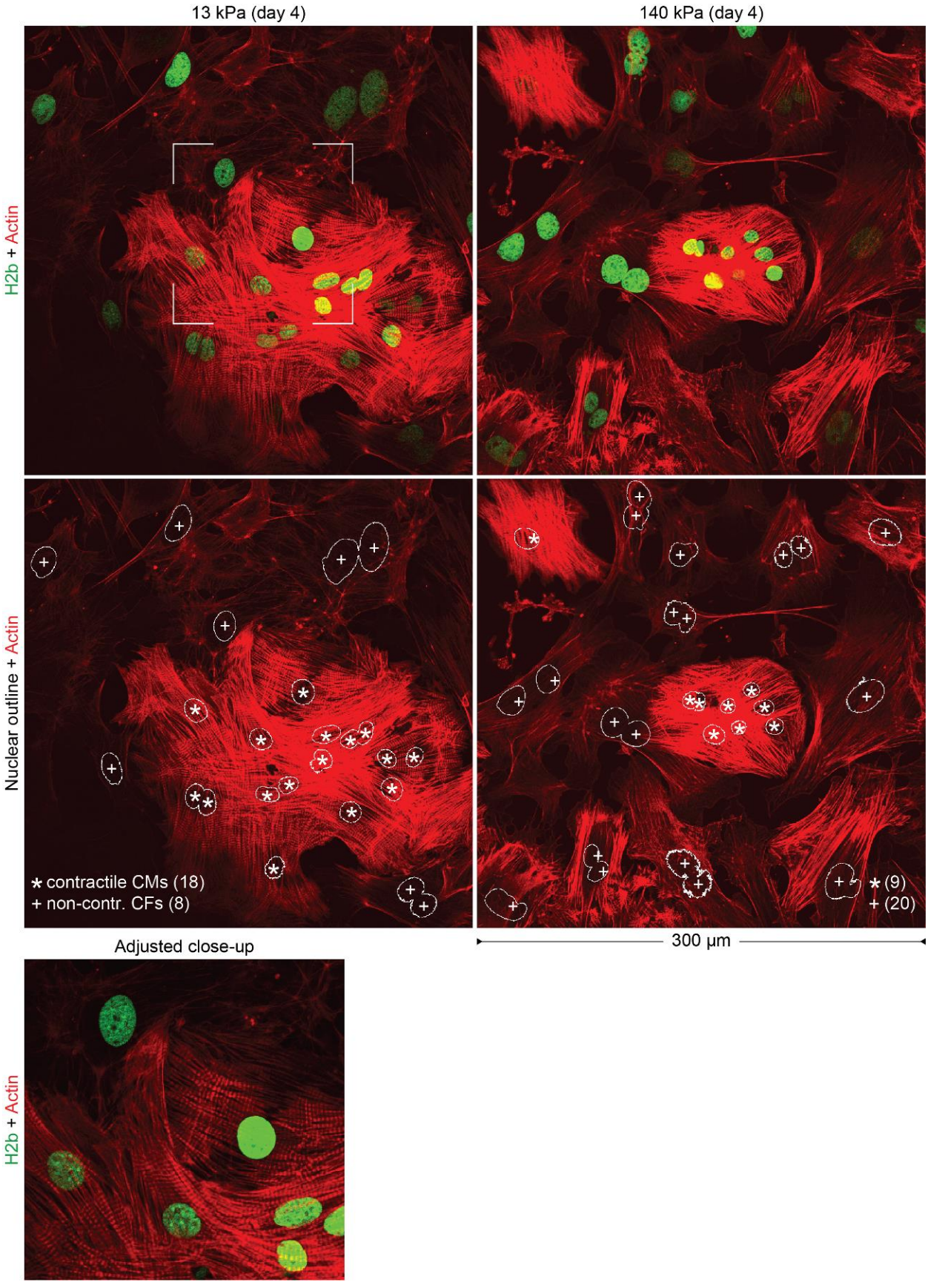
13 kPa (day 4)
140 kPa (day 4)
H2b + Actin
Nuclear outline + Actin
* contractile CMs (18)
+ non-contr. CFs (8)
* (9)
+ (20)
300 µm
Adjusted close-up
H2b + Actin

Extended Figure 3.1. Determining the ratio of contractile CMs to non-contractile CFs in embryonic cardiac cultures on substrates with different stiffness. Embryonic cardiac cells were isolated from (E)18.5 H2b-eGFP embryo hearts and cultured on soft (13 kPa) or stiff (140 kPa) PDMS. After two or four days, cultures were stained for actin and images of 300×300 μm^2 areas were acquired. Using cell nuclei as reference, cells with clearly formed striated myofibrils were counted as contractile CM (*) or otherwise as non-contractile CF (+). Close-up shows the area indicated by a rectangle in the upper-left frame with adjusted intensity settings to accentuate myofibril striations.

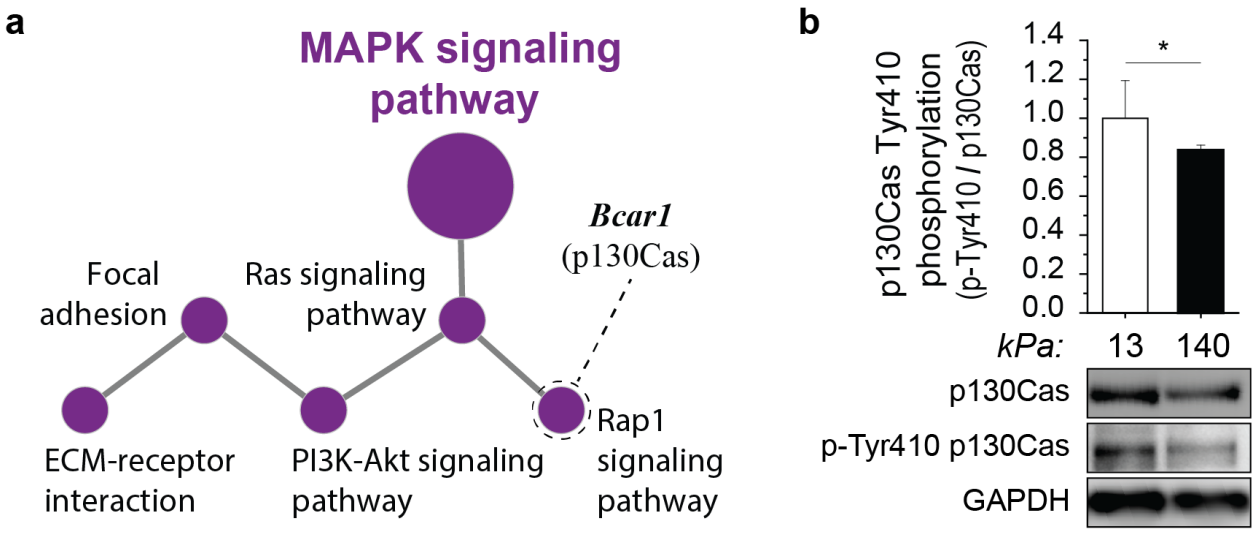

Extended Figure 3.2. Stiff substrates alter cell-ECM interaction pathways and inhibit stretch-activation of associated p130Cas. Cardiac cells were cultured on soft (13 kPa) or stiff (140 kPa) PDMS for four days before RNA or protein was extracted. **a)** Network analysis of global gene expression change revealed alterations in MAPK signaling and associated pathways that play a role in cell-substrate interaction. Rap1 signaling included the downregulation *Bcar1* coding for p130Cas, a mechanosensitive protein located within the Z-disk lattice in CMs. **b)** Western blot analysis showed reduced tyrosine-410 phosphorylation of the stretch-sensitive mechanosensor p130Cas on stiff PDMS compared to soft; SD; n=3; T-test: * $p<0.05$.

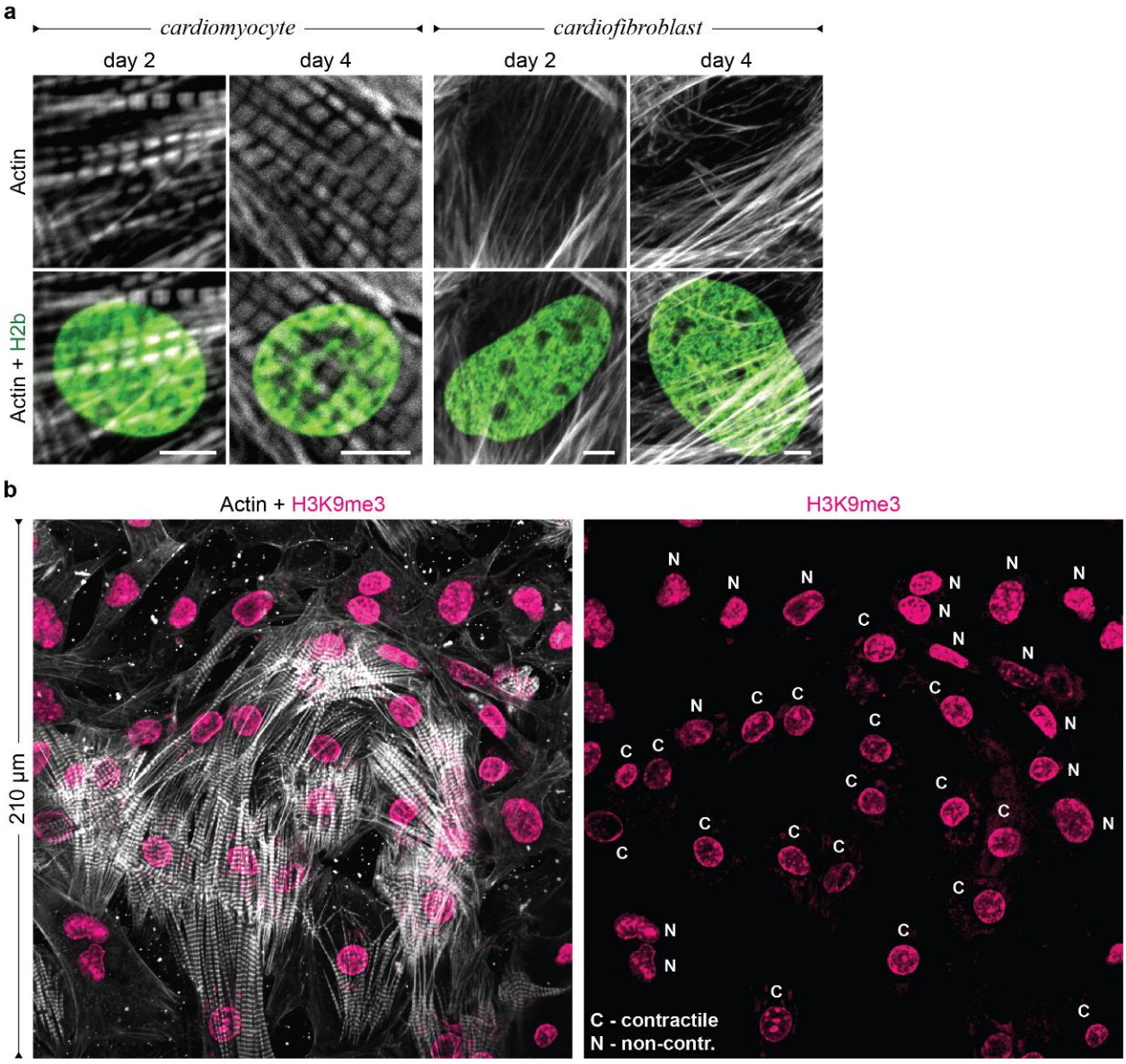

Extended Figure 3.3. Contractile CMs and non-contractile CFs show differences in the positioning of H3K9 trimethylated chromatin *in vitro*. Embryonic cardiac cells were isolated from (E)18.5 H2b-eGFP embryo hearts and cultured on soft (13 kPa) PDMS substrates. **a)** Actin staining corresponding to the data from Figure 3.3b to distinguish CMs from CFs via the formation of contractile myofibrils; scales=5 µm. **b)** After two days in culture, contractile (C) CMs with clearly formed myofibrils showed enrichment of H3K9me3-marked chromatin at the nuclear border while actin-fiber forming non-contractile cells (N) showed a more homogenous distribution throughout the nuclear interior.

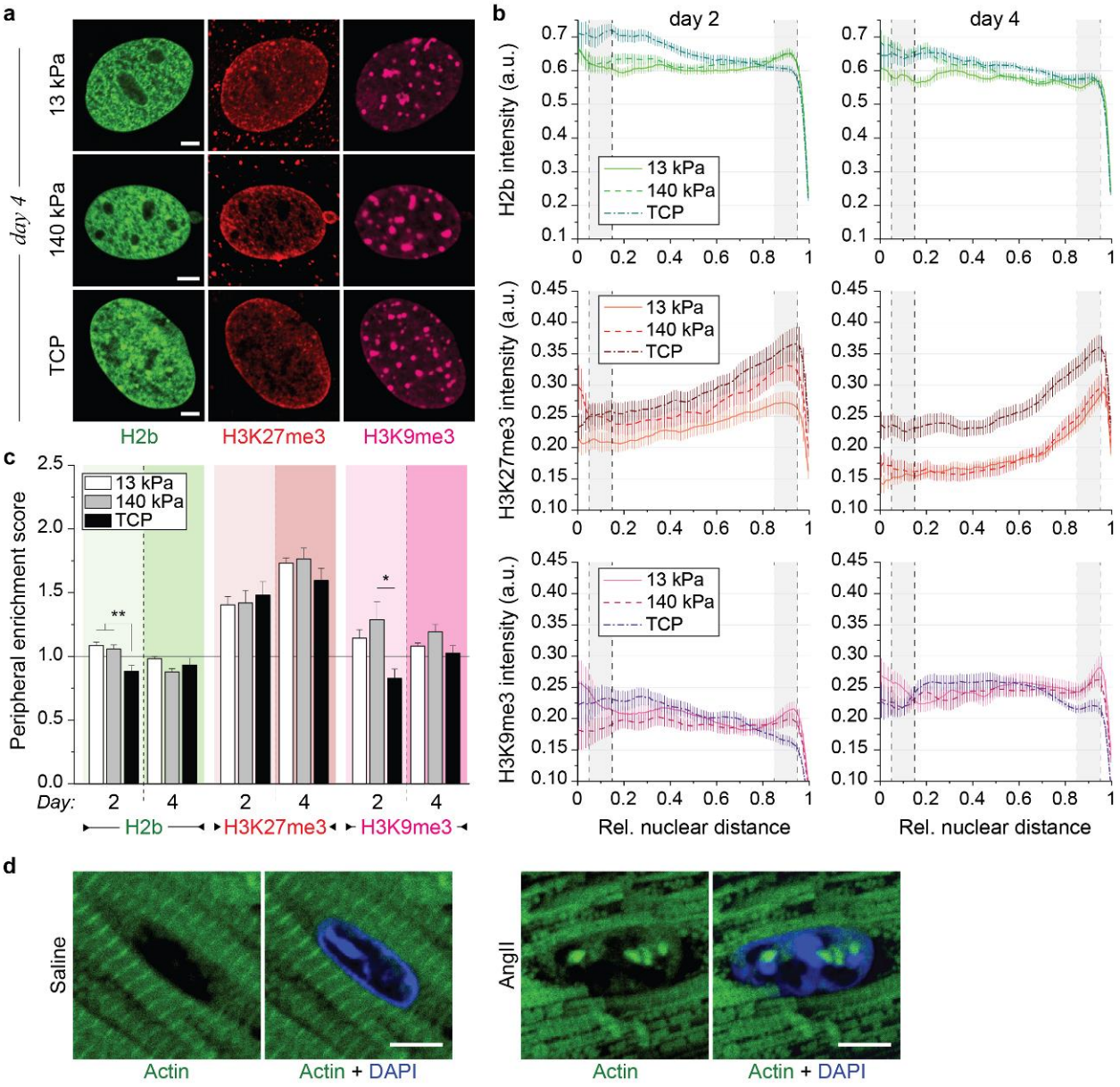

Extended Figure 3.4. Effect of stiff mechanical environments on chromatin organization in non-contractile CFs *in vitro*. a) Embryonic cardiac cells were isolated from (E)18.5 H2b-eGFP embryo hearts and cultured on either soft (13 kPa) PDMS, stiff (140 kPa) PDMS or TCP for two or four days after which cells were stained for H3K27me3 and H3K9me3 as well as actin to distinguish CFs from CMs. **b)** CF nuclei were evaluated for peripheral enrichment of overall chromatin (H2b) or epigenetically marked chromatin using a custom MATLAB code that analyzed marker intensity with respect to its relative distance to the nuclear center (0=center, 1=periphery). Gray areas indicate center and peripheral bin; SEM; n≥30 from 3 exp. **c)** Enrichment scores for each chromatin marker were calculated as the quotient of intensity of the peripheral bin (0.85-0.95) divided by the center bin (0.05-0.15). Substrate stiffness only minorly affected chromatin organization and enrichment of overall and H3K9me3-marked chromatin remained low while

enrichment of H3K27me3-modified chromatin remained high throughout the four-day culture period; SEM; n≥30 from 3 exp.; 1W-ANOVA: * $p<0.05$, ** $p<0.01$. **d)** Actin staining corresponding to the data from Figure 3.4e. All scales=5 µm.

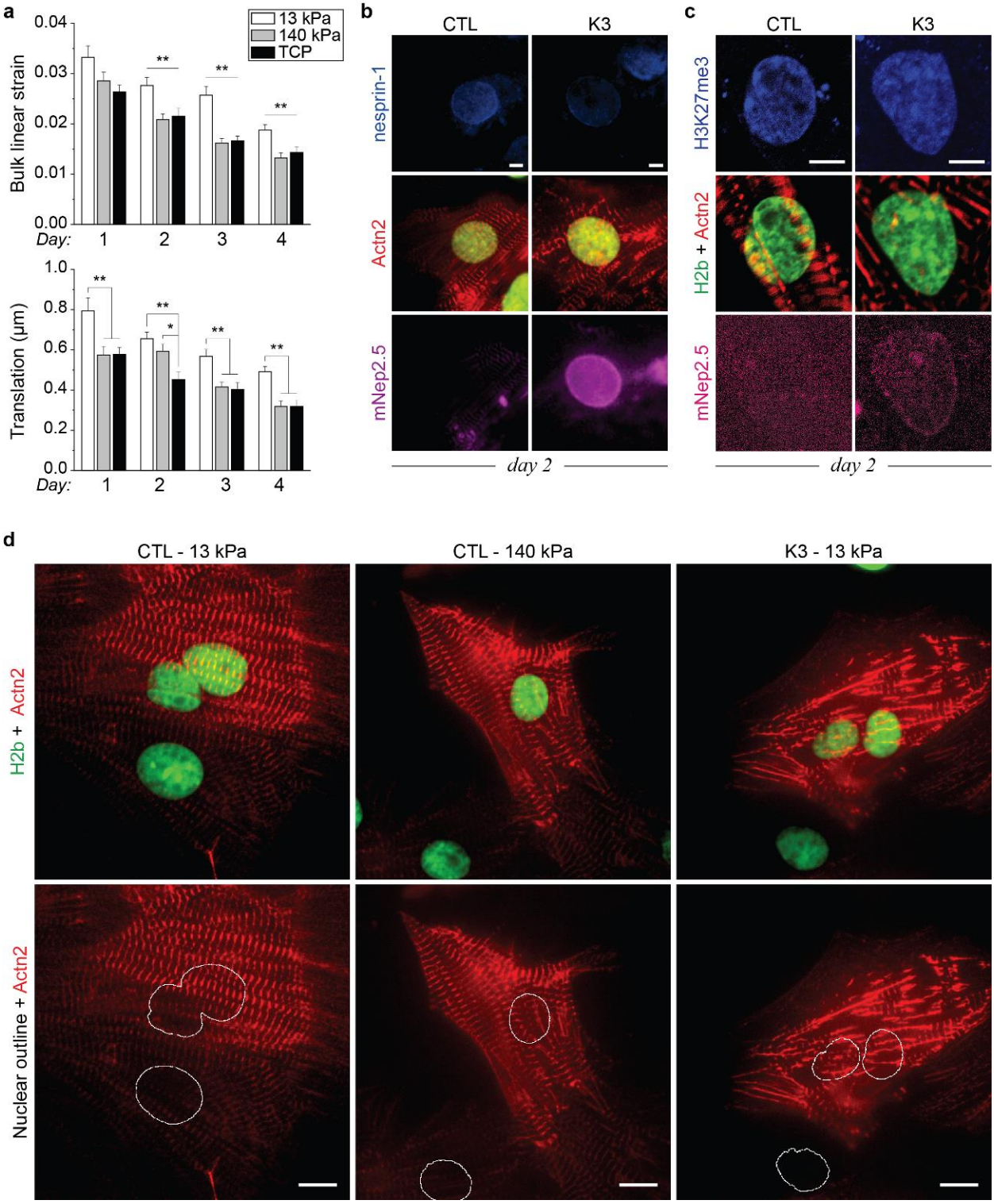

Extended Figure 3.5. LINC complex disruption in CMs. Embryonic cardiac cells were isolated from (E)18.5 H2b-eGFP embryo hearts. **a)** Image series of nuclei of CMs cultured on either soft (13 kPa) PDMS, stiff (140 kPa) PDMS or TCP for four days were recorded during contraction and bulk linear strain and translational movement of nuclei were determined. Nuclei of CMs cultured

on soft substrates showed higher bulk linear strain and translational movement compared to stiff PDMS and TCP; SEM; n>44 from 4 exp.; 1W-ANOVA: * $p<0.05$, ** $p<0.01$. **b)** On day one, cells were infected with an adenoviral vector that disrupted LINC connection or a control vector (see Figure 3.5a). 24h post infection, widefield images of fixed CMs infected with the decoupling vector showed successful integration of the truncated nesprin construct (mNep2.5) into the outer nuclear membrane while no distinct localization was observed for the control vector. Decoupled cells showed disrupted myofibril formation, particularly around the nucleus, and diminished presence of nesprin-1 at the nuclear membrane; scales=5 µm. **c**) CMs were infected at day 1 and stained for actin and H3K27me3 on day two (shown) and day four. Decoupled cells (K3) showed abolished enrichment of overall and H3K9me3-marked chromatin compared to infected control cells (CTL) while H3K27me3-marked chromatin was similarly enriched (see also Figure 3.5); scales=5 µm. **d)** Images of infected cells plated on either soft (13 kPa) or stiff (140 kPa) PDMS. Decoupled cells show disrupted sarcomere fibers, particularly around the nucleus. See also Extended Videos 1-3; scales=10 µm.

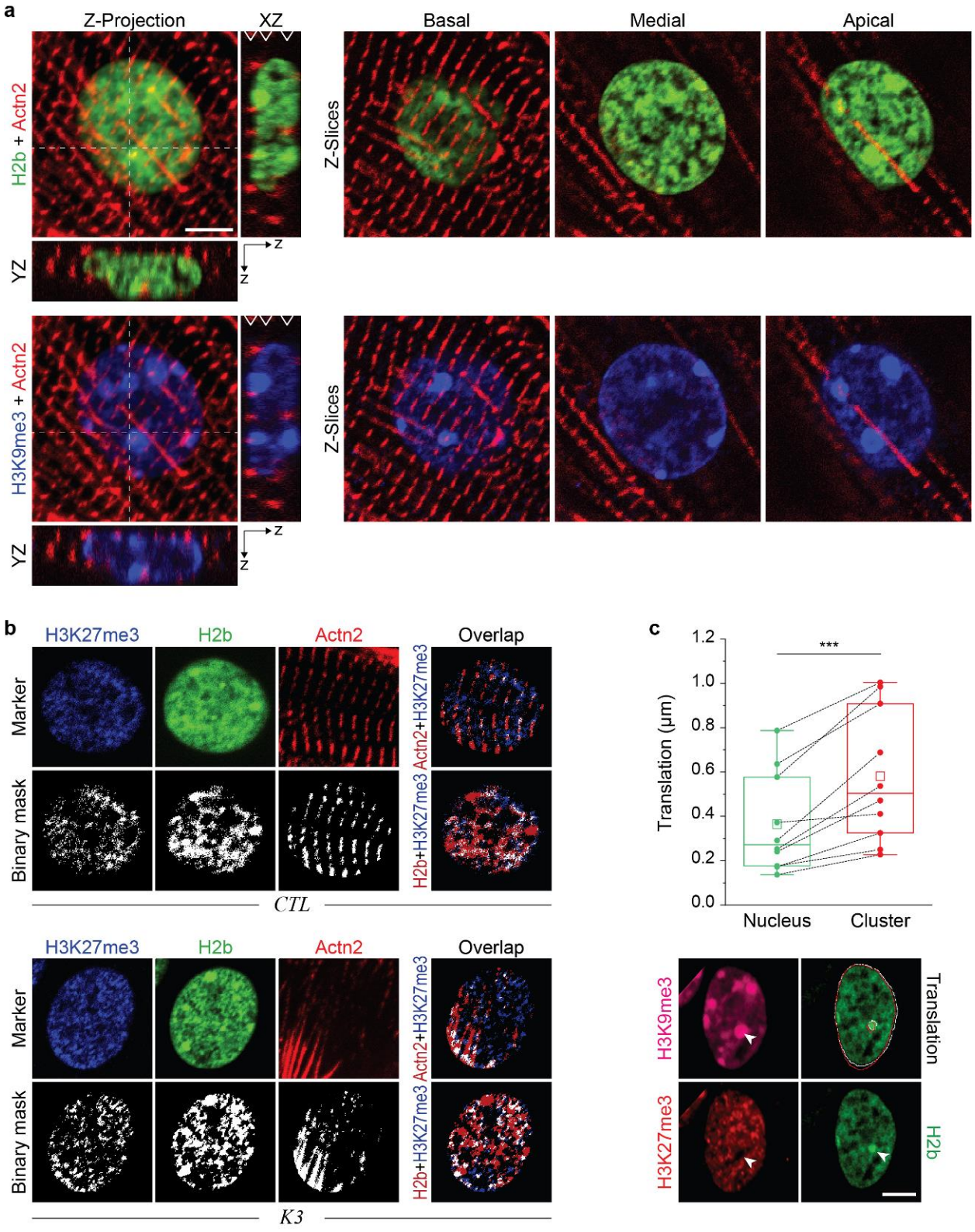

Extended Figure 3.6. Co-localization of chromatin markers with myofibrils in CMs after LINC complex disruption. Embryonic cardiac cells were isolated from (E)18.5 H2b-eGFP

embryo hearts and cultured on soft PDMS (13 kPa). **a)** CMs were infected with K3 or CTL (shown) on day one and stained for H3K9me3 (shown) or H3K27me3 on day four after which z-stacks were recorded on a confocal microscope. Left: Z-projection as well as XZ and YZ slices along white dashed lines for a CTL infected CM. Right: Panels show representative z-slices at different z-positions (basal, medial, apical) indicated by white arrows in the XZ projection. Basal z-slices were used for marker overlap analysis; scale=5 µm. **b)** CMs were infected with K3 or CTL on day one and stained for H3K9me3 (see Figure 3.6f) or H3K27me3 (shown) on day four to analyze marker overlap. **c)** Nuclear image stacks of beating CMs were recorded on day two after which cells were stained for H3K9me3 and H3K27me3 and translation of dense, H3K9me3-rich heterochromatin clusters and overall nuclear translation were analyzed. Translational movement was higher for heterochromatin clusters than for nuclei during contractions. White and red outlines indicate nuclear and cluster boundary during rest and peak contraction, respectively; n=10 from 3 exp.; T-test: *** $p<0.001$; scale=5 µm.

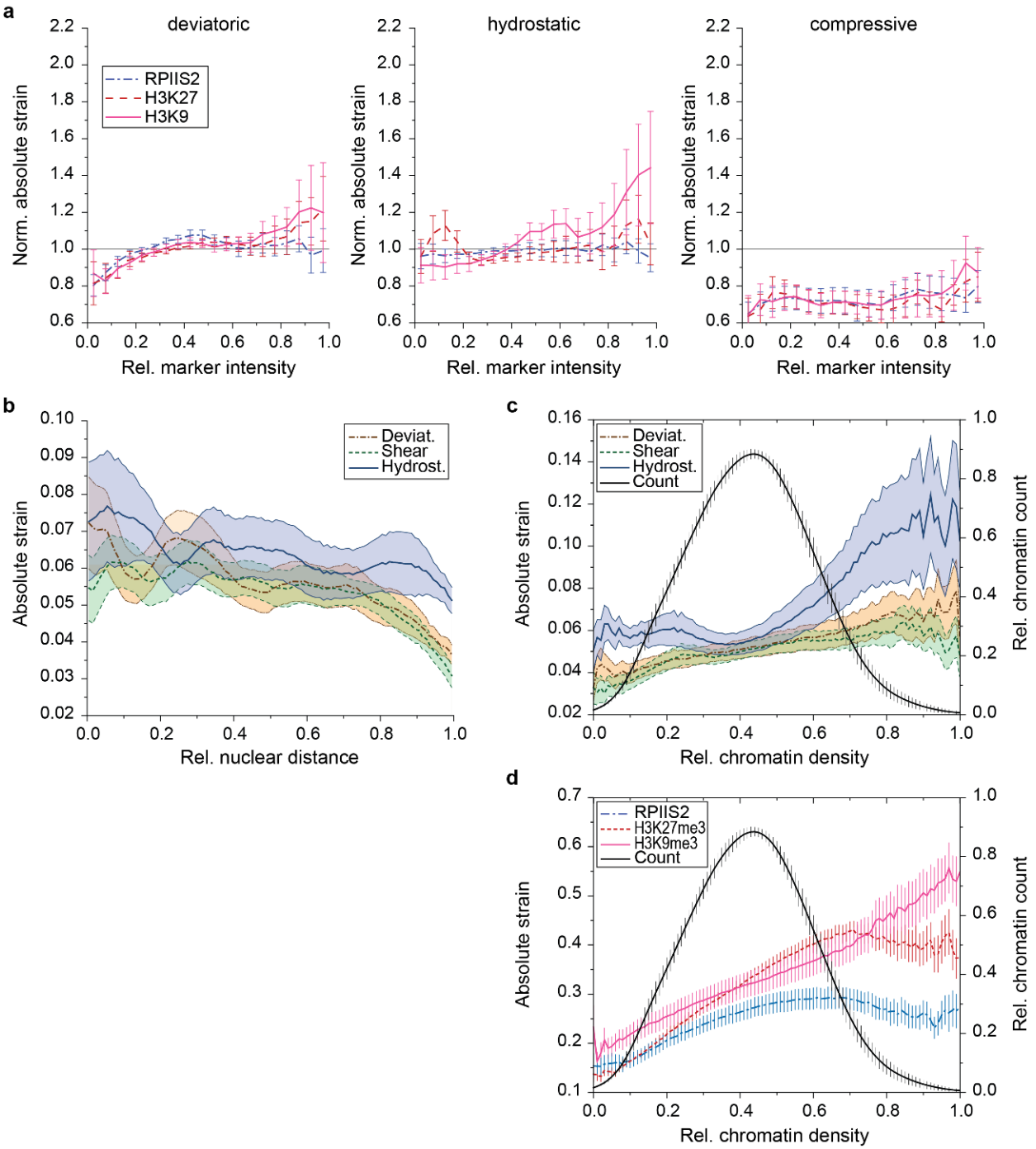

Extended Figure 3.7. Extended analysis of intranuclear strains during CM contraction. CMs were isolated from (E)18.5 H2b-eGFP embryo hearts and cultured on soft (13 kPa) PDMS for two days. Intranuclear strain maps of CM nuclei during contraction were generated via *deformation microscopy* after which cells were stained for H3K9me3, H3K27me3 or actively transcribed chromatin (RPIIS2) and strain occupancy for chromatin markers was analyzed (see Figure 3.7). **a)** Intranuclear strains were analyzed over chromatin marker intensities. **b)** Intranuclear strains were

analyzed over distance to the nuclear center. Strains declined towards the nuclear border. **c, d)** Intranuclear strains and chromatin marker intensities were analyzed over relative chromatin density based on H2b intensity. Chromatin density distribution (histogram) is represented as relative chromatin count on the right *y*-axis. Hydrostatic strains are lowest around medium chromatin density (density histogram peak) and increases for denser chromatin which is primarily occupied by H3K9me3 modifications.

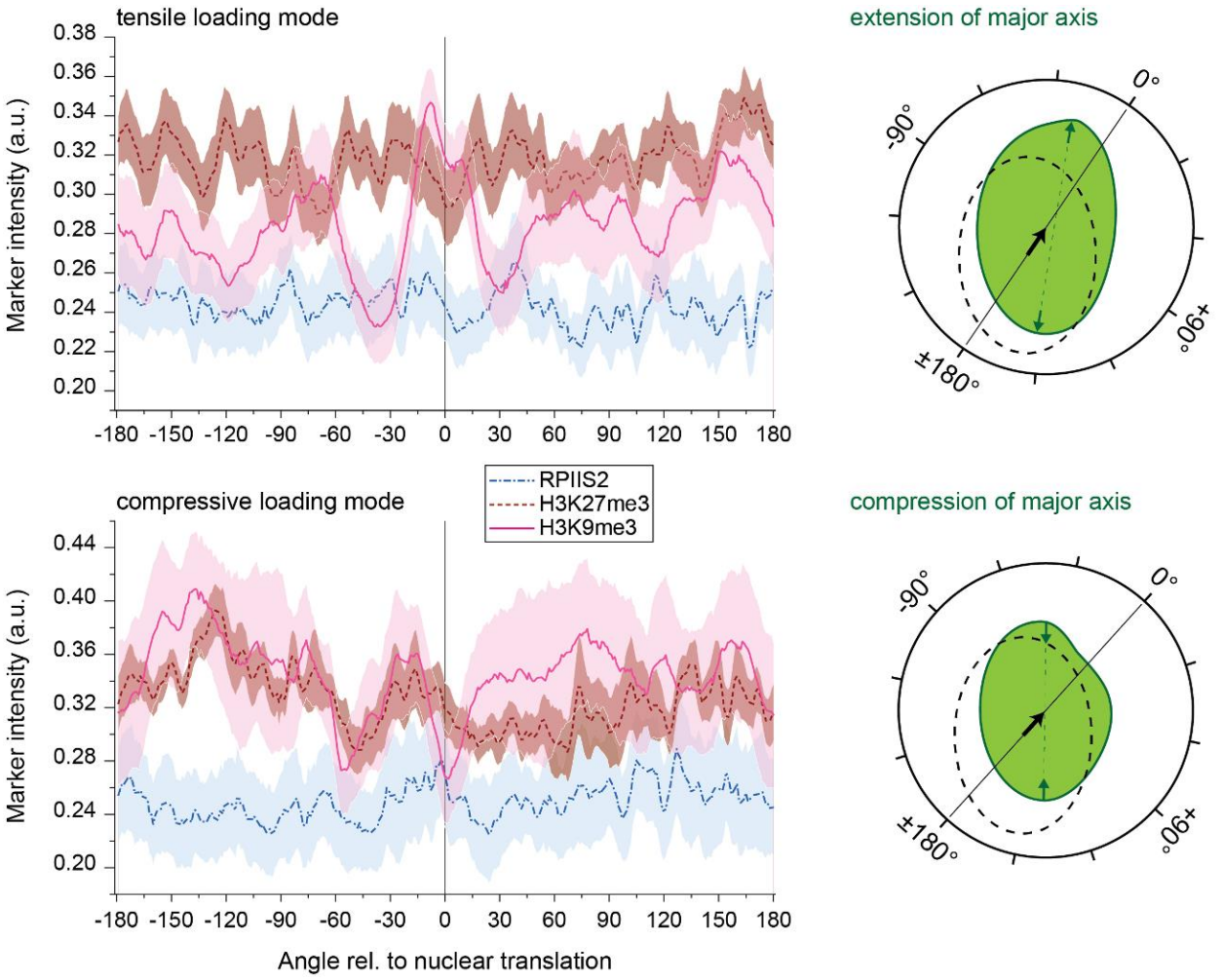

Extended Figure 3.8. H3K9 methylated chromatin occupancy peaks in the direction of contraction in nuclei with tensile loading mode. CMs were isolated from (E)18.5 H2b-eGFP embryo hearts and cultured on soft (13 kPa) PDMS for two days. Image stacks of CM nuclei were recorded during contractions to determine the direction of nuclear translation. Cells were then stained for chromatin markers H3K9me3, H3K27me3 or actively transcribed chromatin (RPIIS2). Chromatin marker occupancy was calculated with respect to the angle of the nuclear center with the angle of nuclear translation set to 0°. Cells with extended major axis during contraction (tensile loading mode, n=20, same as intranuclear analysis) showed a distinct peak of H3K9me3 intensity ±30° around the direction of translation while a decline in H3K9me3 intensity was observed for cells with shortened major axis (compressive loading mode, n=8). Right side provides a graphic illustration of angular analysis showing nuclear outlines during resting phase (doted black) and peak contraction (solid green). The black arrow indicates the direction of translation, which defines the 0° point, and green arrows demonstrate extension or compression of the nuclear major axis used to determine the loading mode of cells; areas=SEM; from 5 exp.

3.7. REFERENCES

1. Engler, A. J., Sen, S., Sweeney, H. L. & Discher, D. E. Matrix elasticity directs stem cell lineage specification. *Cell* **126**, 677–89 (2006).
2. Phillip, J. M., Aifuwa, I., Walston, J. & Wirtz, D. The Mechanobiology of Aging. *Annu. Rev. Biomed. Eng.* **17**, 113–141 (2015).
3. Lampi, M. C. & Reinhart-King, C. A. Targeting extracellular matrix stiffness to attenuate disease: From molecular mechanisms to clinical trials. *Sci. Transl. Med.* **10**, eaao0475 (2018).
4. Thienpont, B. *et al.* The H3K9 dimethyltransferases EHMT1/2 protect against pathological cardiac hypertrophy. *J. Clin. Invest.* **127**, 335–348 (2017).
5. Zhang, Q. J. *et al.* The histone trimethyllysine demethylase JMJD2A promotes cardiac hypertrophy in response to hypertrophic stimuli in mice. *J. Clin. Invest.* **121**, 2447–2456 (2011).
6. Swift, J. *et al.* Nuclear lamin-A scales with tissue stiffness and enhances matrix-directed differentiation. *Science* **341**, 1240104 (2013).
7. Fedorchak, G. R., Kaminski, A. & Lammerding, J. Cellular mechanosensing: Getting to the nucleus of it all. *Prog. Biophys. Mol. Biol.* (2014). doi:10.1016/j.pbiomolbio.2014.06.009
8. Heo, S.-J. *et al.* Differentiation alters stem cell nuclear architecture, mechanics, and mechano-sensitivity. *Elife* **5**, (2016).
9. Uzer, G. *et al.* Cell mechanosensitivity to extremely low-magnitude signals is enabled by a LINCed nucleus. *Stem Cells* **33**, 2063–2076 (2015).

10. Spagnol, S. T., Armiger, T. J. & Dahl, K. N. Mechanobiology of Chromatin and the Nuclear Interior. *Cell. Mol. Bioeng.* **9**, 268–276 (2016).

11. Crisp, M. *et al.* Coupling of the nucleus and cytoplasm: Role of the LINC complex. *J. Cell Biol.* **172**, 41–53 (2006).

12. Apel, E. D., Lewis, R. M., Grady, R. M. & Sanes, J. R. Syne-1, a dystrophin- and Klarsicht-related protein associated with synaptic nuclei at the neuromuscular junction. *J. Biol. Chem.* **275**, 31986–95 (2000).

13. Zhang, Q., Ragnauth, C., Greener, M. J., Shanahan, C. M. & Roberts, R. G. The nesprins are giant actin-binding proteins, orthologous to Drosophila melanogaster muscle protein MSP-300. *Genomics* **80**, 473–81 (2002).

14. Guilluy, C. *et al.* Isolated nuclei adapt to force and reveal a mechanotransduction pathway in the nucleus. *Nat. Cell Biol.* **16**, 376–381 (2014).

15. Davidson, P. M. & Lammerding, J. Broken nuclei - lamins, nuclear mechanics, and disease. *Trends Cell Biol.* **24**, 247–256 (2013).

16. Puckelwartz, M. J. *et al.* Nesprin-1 mutations in human and murine cardiomyopathy. *J. Mol. Cell. Cardiol.* **48**, 600–8 (2010).

17. Banerjee, I. *et al.* Targeted ablation of nesprin 1 and nesprin 2 from murine myocardium results in cardiomyopathy, altered nuclear morphology and inhibition of the biomechanical gene response. *PLoS Genet.* **10**, e1004114 (2014).

18. Hug, C. B. & Vaquerizas, J. M. The Birth of the 3D Genome during Early Embryonic Development. *Trends Genet.* **34**, 903–914 (2018).

19. Solovei, I. *et al.* LBR and lamin A/C sequentially tether peripheral heterochromatin and inversely regulate differentiation. *Cell* **152**, 584–98 (2013).

20. de Las Heras, J. I. *et al.* Tissue specificity in the nuclear envelope supports its functional complexity. *Nucleus* **4**, 460–77 (2014).

21. Joffe, B., Leonhardt, H. & Solovei, I. Differentiation and large scale spatial organization of the genome. *Curr. Opin. Genet. Dev.* **20**, 562–9 (2010).

22. Parada, L. A., McQueen, P. G. & Misteli, T. Tissue-specific spatial organization of genomes. *Genome Biol.* **5**, R44 (2004).

23. Dekker, J. *et al.* The 4D nucleome project. *Nature* **549**, 219–226 (2017).

24. Pombo, A. & Dillon, N. Three-dimensional genome architecture: players and mechanisms. *Nat. Rev. Mol. Cell Biol.* **16**, 245–57 (2015).

25. Olins, A. L. & Olins, D. E. Cytoskeletal influences on nuclear shape in granulocytic HL-60 cells. *BMC Cell Biol.* **5**, 30 (2004).

26. Kim, S. H. *et al.* Spatial genome organization during T-cell differentiation. *Cytogenet. Genome Res.* **105**, 292–301 (2004).

27. Solovei, I. *et al.* Nuclear architecture of rod photoreceptor cells adapts to vision in mammalian evolution. *Cell* **137**, 356–68 (2009).

28. Engler, A. J. *et al.* Myotubes differentiate optimally on substrates with tissue-like stiffness: Pathological implications for soft or stiff microenvironments. *J. Cell Biol.* **166**, 877–887 (2004).

29. Jacot, J. G., McCulloch, A. D. & Omens, J. H. Substrate stiffness affects the functional maturation of neonatal rat ventricular myocytes. *Biophys. J.* **95**, 3479–87 (2008).

30. Yahalom-Ronen, Y., Rajchman, D., Sarig, R., Geiger, B. & Tzahor, E. Reduced matrix rigidity promotes neonatal cardiomyocyte dedifferentiation, proliferation and clonal expansion. *Elife* **4**, (2015).

31. Ghosh, S. *et al.* Deformation Microscopy for Dynamic Intracellular and Intranuclear Mapping of Mechanics with High Spatiotemporal Resolution. *Cell Rep.* **27**, 1607-1620.e4 (2019).

32. Henderson, J. T., Shannon, G., Veress, A. I. & Neu, C. P. Direct measurement of intranuclear strain distributions and RNA synthesis in single cells embedded within native tissue. *Biophys. J.* **105**, 2252–61 (2013).

33. Barnes, J. M., Przybyla, L. & Weaver, V. M. Tissue mechanics regulate brain development, homeostasis and disease. *J. Cell Sci.* **130**, 71–82 (2017).

34. Sreejit, P., Kumar, S. & Verma, R. S. An improved protocol for primary culture of cardiomyocyte from neonatal mice. *Vitr. Cell. Dev. Biol. - Anim.* **44**, 45–50 (2008).

35. Young, J. L., Kretchmer, K., Ondeck, M. G., Zambon, A. C. & Engler, A. J. Mechanosensitive kinases regulate stiffness-induced cardiomyocyte maturation. *Sci. Rep.* **4**, 6425 (2014).

36. Kennani, S. El *et al.* MS_HistoneDB, a manually curated resource for proteomic analysis of human and mouse histones. *Epigenetics Chromatin* **10**, 2 (2017).

37. Terme, J.-M. *et al.* Histone H1 variants are differentially expressed and incorporated into chromatin during differentiation and reprogramming to pluripotency. *J. Biol. Chem.* **286**, 35347–57 (2011).

38. Barrero, M. J., Sese, B., Martí, M. & Izpisua Belmonte, J. C. Macro histone variants are critical for the differentiation of human pluripotent cells. *J. Biol. Chem.* **288**, 16110–6 (2013).

39. Xia, W. & Jiao, J. Histone variant H3.3 orchestrates neural stem cell differentiation in the developing brain. *Cell Death Differ.* **24**, 1548–1563 (2017).

40. Valenzuela, N. *et al.* Cardiomyocyte-specific conditional knockout of the histone chaperone HIRA in mice results in hypertrophy, sarcolemmal damage and focal replacement fibrosis. *Dis. Model. Mech.* **9**, 335–45 (2016).

41. Rose, B. A., Force, T. & Wang, Y. Mitogen-activated protein kinase signaling in the heart: angels versus demons in a heart-breaking tale. *Physiol. Rev.* **90**, 1507–46 (2010).

42. Riccio, A. Dynamic epigenetic regulation in neurons: enzymes, stimuli and signaling pathways. *Nat. Neurosci.* **13**, 1330–7 (2010).

43. Hogan, M. S., Parfitt, D. E., Zepeda-Mendoza, C. J., Shen, M. M. & Spector, D. L. Transient pairing of homologous Oct4 alleles accompanies the onset of embryonic stem cell differentiation. *Cell Stem Cell* **16**, 275–288 (2015).

44. Filion, G. J. *et al.* Systematic protein location mapping reveals five principal chromatin types in Drosophila cells. *Cell* **143**, 212–24 (2010).

45. Mysliwiec, M. R. *et al.* Jarid2 (Jumonji, AT rich interactive domain 2) regulates NOTCH1 expression via histone modification in the developing heart. *J. Biol. Chem.* **287**, 1235–1241 (2012).

46. Dal-Pra, S., Hodgkinson, C. P., Mirotsou, M., Kirste, I. & Dzau, V. J. Demethylation of H3K27 Is Essential for the Induction of Direct Cardiac Reprogramming by MIR Combo. *Circ. Res.* **120**, 1403–1413 (2017).

47. Lu, W. *et al.* Nesprin interchain associations control nuclear size. *Cell. Mol. Life Sci.* **69**, 3493–3509 (2012).

48. Grady, R. M., Starr, D. a, Ackerman, G. L., Sanes, J. R. & Han, M. Syne proteins anchor muscle nuclei at the neuromuscular junction. *Proc. Natl. Acad. Sci. U. S. A.* **102**, 4359–4364 (2005).

49. Iyer, K. V., Pulford, S., Mogilner, A. & Shivashankar, G. V. Mechanical activation of cells induces chromatin remodeling preceding MKL nuclear transport. *Biophys. J.* **103**, 1416–1428 (2012).

50. Balakrishnan, L. & Milavetz, B. Epigenetic Regulation of Viral Biological Processes. *Viruses* **9**, (2017).

51. Akimoto, T. *et al.* Skeletal muscle adaptation in response to mechanical stress in p130cas $^{-/-}$ mice. *Am. J. Physiol. Physiol.* **304**, C541–C547 (2013).

52. Sawada, Y. *et al.* Force Sensing by Mechanical Extension of the Src Family Kinase Substrate p130Cas. *Cell* **127**, 1015–1026 (2006).

53. Kovacic-Milivojević, B., Damsky, C. C., Gardner, D. G. & Ilić, D. Requirements for the localization of p130 Cas to Z-lines in cardiac myocytes. *Cell. Mol. Biol. Lett.* **7**, 323–9 (2002).

54. Auld, A. L. & Folker, E. S. Nucleus-dependent sarcomere assembly is mediated by the LINC complex. *Mol. Biol. Cell* **27**, 2351–2359 (2016).

55. Ni, Z. *et al.* P-TEFb is critical for the maturation of RNA polymerase II into productive elongation in vivo. *Mol. Cell. Biol.* **28**, 1161–70 (2008).

56. Sexton, T., Schober, H., Fraser, P. & Gasser, S. M. Gene regulation through nuclear organization. *Nat. Struct. Mol. Biol.* **14**, 1049–55 (2007).

57. Honda, H. *et al.* Cardiovascular anomaly, impaired actin bundling and resistance to Src-induced transformation in mice lacking p130(Cas). *Nat. Genet.* **19**, 361–365 (1998).

58. Queisser, G., Wiegert, S. & Bading, H. Structural dynamics of the cell nucleus: basis for morphology modulation of nuclear calcium signaling and gene transcription. *Nucleus* **2**, 98–104 (2011).

59. Stephens, A. D. *et al.* Chromatin histone modifications and rigidity affect nuclear morphology independent of lamins. *Mol. Biol. Cell* **29**, 220–233 (2018).

60. Alam, S. G. *et al.* The mammalian LINC complex regulates genome transcriptional responses to substrate rigidity. *Sci. Rep.* **6**, 38063 (2016).

61. Spitzer, N. C. Electrical activity in early neuronal development. *Nature* **444**, 707–712 (2006).

62. Mehta, I. S., Amira, M., Harvey, A. J. & Bridger, J. M. Rapid chromosome territory relocation by nuclear motor activity in response to serum removal in primary human fibroblasts. *Genome Biol.* **11**, R5 (2010).

63. Kulashreshtha, M., Mehta, I. S., Kumar, P. & Rao, B. J. Chromosome territory relocation during DNA repair requires nuclear myosin 1 recruitment to chromatin mediated by ϒ-H2AX signaling. *Nucleic Acids Res.* **44**, 8272–91 (2016).

64. Wilkie, G. S. *et al.* Several Novel Nuclear Envelope Transmembrane Proteins Identified in Skeletal Muscle Have Cytoskeletal Associations. *Mol. Cell. Proteomics* **10**, M110.003129 (2011).

65. Zuleger, N. *et al.* Specific nuclear envelope transmembrane proteins can promote the location of chromosomes to and from the nuclear periphery. *Genome Biol.* **14**, R14 (2013).

66. Aureille, J., Belaadi, N. & Guilluy, C. Mechanotransduction via the nuclear envelope: a distant reflection of the cell surface. *Curr. Opin. Cell Biol.* **44**, 59–67 (2017).

67. Pasqualini, F. S. *et al.* Traction force microscopy of engineered cardiac tissues. *PLoS One* **13**, e0194706 (2018).

68. Xu, X., Li, Z., Cai, L., Calve, S. & Neu, C. P. Mapping the Nonreciprocal

Micromechanics of Individual Cells and the Surrounding Matrix Within Living Tissues. *Sci. Rep.* **6**, 24272 (2016).

69. Worke, L. J. *et al.* Densification of Type I Collagen Matrices as a Model for Cardiac Fibrosis. *Adv. Healthc. Mater.* **6**, (2017).

70. Li, Q. *et al.* Selection of reference genes for normalization of quantitative polymerase chain reaction data in mouse models of heart failure. *Mol. Med. Rep.* **11**, 393–9 (2015).

71. Martino, A. *et al.* Selection of reference genes for normalization of real-time PCR data in minipig heart failure model and evaluation of TNF-α mRNA expression. *J. Biotechnol.* **153**, 92–9 (2011).

72. Pereyra, A. S. *et al.* Loss of cardiac carnitine palmitoyltransferase 2 results in rapamycin-resistant, acetylation-independent hypertrophy. *J. Biol. Chem.* **292**, 18443–18456 (2017).

73. Pugach, E. K., Blenck, C. L., Dragavon, J. M., Langer, S. J. & Leinwand, L. A. Estrogen receptor profiling and activity in cardiac myocytes. *Mol. Cell. Endocrinol.* **431**, 62–70 (2016).

74. Chu, J. *et al.* Non-invasive intravital imaging of cellular differentiation with a bright red-excitable fluorescent protein. *Nat. Methods* **11**, 572–578 (2014).

Bibliography

Abad, Patricia C., Jason Lewis, I. Saira Mian, David W. Knowles, Jennifer Sturgis, Sunil Badve, Jun Xie, and Sophie A. Lelièvre. 2007. "NuMA Influences Higher Order Chromatin Organization in Human Mammary Epithelium." *Molecular Biology of the Cell* 18(2):348–61.

Akimoto, Takayuki, Kanako Okuhira, Katsuji Aizawa, Shogo Wada, Hiroaki Honda, Toru Fukubayashi, and Takashi Ushida. 2013. "Skeletal Muscle Adaptation in Response to Mechanical Stress in P130cas $^{-/-}$ Mice." *American Journal of Physiology-Cell Physiology* 304(6):C541–47.

Alam, Samer G., Qiao Zhang, Nripesh Prasad, Yuan Li, Srikar Chamala, Ram Kuchibhotla, Birendra Kc, Varun Aggarwal, Shristi Shrestha, Angela L. Jones, Shawn E. Levy, Kyle J. Roux, Jeffrey A. Nickerson, and Tanmay P. Lele. 2016. "The Mammalian LINC Complex Regulates Genome Transcriptional Responses to Substrate Rigidity." *Scientific Reports* 6(1):38063.

Albrethsen, Jakob, Jaco C. Knol, and Connie R. Jimenez. 2009. "Unravelling the Nuclear Matrix Proteome." *Journal of Proteomics* 72(1):71–81.

Ali, M. Yusuf, Andrej Vilfan, Kathleen M. Trybus, and David M. Warshaw. 2016. "Cargo Transport by Two Coupled Myosin Va Motors on Actin Filaments and Bundles." *Biophysical Journal* 111(10):2228–40.

Almuzzaini, Bader, Aishe A. Sarshad, Ann Kristin Östlund Farrants, and Piergiorgio Percipalle. 2015. "Nuclear Myosin 1 Contributes to a Chromatin Landscape Compatible with RNA Polymerase II Transcription Activation." *BMC Biology* 13(1):1–15.

Apel, E. D., R. M. Lewis, R. M. Grady, and J. R. Sanes. 2000. “Syne-1, a Dystrophin- and Klarsicht-Related Protein Associated with Synaptic Nuclei at the Neuromuscular Junction.” *The Journal of Biological Chemistry* 275(41):31986–95.

Auld, Alexander L. and Eric S. Folker. 2016. “Nucleus-Dependent Sarcomere Assembly Is Mediated by the LINC Complex” edited by K. Weis. *Molecular Biology of the Cell* 27(15):2351–59.

Aureille, Julien, Néjma Belaadi, and Christophe Guilluy. 2017. “Mechanotransduction via the Nuclear Envelope: A Distant Reflection of the Cell Surface.” *Current Opinion in Cell Biology* 44:59–67.

Balakrishnan, Lata and Barry Milavetz. 2017. “Epigenetic Regulation of Viral Biological Processes.” *Viruses* 9(11).

Banerjee, Indroneal, Jianlin Zhang, Thomas Moore-Morris, Emily Pfeiffer, Kyle S. Buchholz, Ao Liu, Kunfu Ouyang, Matthew J. Stroud, Larry Gerace, Sylvia M. Evans, Andrew McCulloch, and Ju Chen. 2014. “Targeted Ablation of Nesprin 1 and Nesprin 2 from Murine Myocardium Results in Cardiomyopathy, Altered Nuclear Morphology and Inhibition of the Biomechanical Gene Response.” *PLoS Genetics* 10(2):e1004114.

Barboro, Paola, Cristina D’Arrigo, Alberto Diaspro, Michele Mormino, Ingles Alberti, Silvio Parodi, Eligio Patrone, and Cecilia Balbi. 2002. “Unraveling the Organization of the Internal Nuclear Matrix: RNA-Dependent Anchoring of NuMA to a Lamin Scaffold.” *Experimental Cell Research* 279(2):202–18.

Barnes, J. Matthew, Laralynne Przybyla, and Valerie M. Weaver. 2017. “Tissue Mechanics Regulate Brain Development, Homeostasis and Disease.” *Journal of Cell Science* 130(1):71–82.

Barrero, María J., Borja Sese, Mercè Martí, and Juan Carlos Izpisua Belmonte. 2013. “Macro Histone Variants Are Critical for the Differentiation of Human Pluripotent Cells.” *The Journal of Biological Chemistry* 288(22):16110–16.

Bartalena, Guido, Reto Grieder, Ram I. Sharma, Tomaso Zambelli, Roman Muff, and Jess G. Snedeker. 2011. “A Novel Method for Assessing Adherent Single-Cell Stiffness in Tension: Design and Testing of a Substrate-Based Live Cell Functional Imaging Device.” *Biomedical Microdevices* 13(2):291–301.

Battulin, Nariman, Veniamin S. Fishman, Alexander M. Mazur, Mikhail Pomaznoy, Anna A. Khabarova, Dmitry A. Afonnikov, Egor B. Prokhortchouk, and Oleg L. Serov. 2015. “Comparison of the Three-Dimensional Organization of Sperm and Fibroblast Genomes Using the Hi-C Approach.” *Genome Biology* 16(1):77.

Belin, Brittany J., Beth a Cimini, Elizabeth H. Blackburn, and R. Dyche Mullins. 2013. “Visualization of Actin Filaments and Monomers in Somatic Cell Nuclei.” *Molecular Biology of the Cell* 24(7):982–94.

Bloom, Kerry and Ajit Joglekar. 2010. “Towards Building a Chromosome Segregation Machine.” *Nature* 463(7280):446–56.

Bolzer, Andreas, Gregor Kreth, Irina Solovei, Daniela Koehler, Kaan Saracoglu, Christine Fauth, Stefan Müller, Roland Eils, Christoph Cremer, Michael R. Speicher, and Thomas Cremer. 2005. “Three-Dimensional Maps of All Chromosomes in Human Male Fibroblast Nuclei and Prometaphase Rosettes.” *PLoS Biology* 3(5):e157.

Bošković, Ana, André Eid, Julien Pontabry, Takashi Ishiuchi, Coralie Spiegelhalter, Edupuganti V. S. Raghu Ram, Eran Meshorer, and Maria-Elena Torres-Padilla. 2014. “Higher Chromatin Mobility Supports Totipotency and Precedes Pluripotency in Vivo.” *Genes &*

Development 28(10):1042–47.

Campbell, Neil A. and Jane B. Reece. 1997. *Biology : Concepts & Connections*. Addison Wesley Longman.

Carter, Dennis R., Gary S. Beaupré, Marcy Wong, R. Lane Smith, Tom P. Andriacchi, and David J. Schurman. 2004. "The Mechanobiology of Articular Cartilage Development and Degeneration." *Clinical Orthopaedics and Related Research* 427(427 Suppl):S69-77.

Chalut, Kevin J., Markus Höpfler, Franziska Lautenschläger, Lars Boyde, Chii Jou Chan, Andrew Ekpenyong, Alfonso Martinez-Arias, and Jochen Guck. 2012. "Chromatin Decondensation and Nuclear Softening Accompany Nanog Downregulation in Embryonic Stem Cells." *Biophysical Journal* 103(10):2060–70.

Chionna, A., M. Dwikat, E. Panzarini, B. Tenuzzo, E. C. Carlà, T. Verri, P. Pagliara, L. Abbro, and L. Dini. 2003. "Cell Shape and Plasma Membrane Alterations after Static Magnetic Fields Exposure." *European Journal of Histochemistry : EJH* 47(4):299–308.

Chu, Jun, Russell D. Haynes, Stéphane Y. Corbel, Pengpeng Li, Emilio González-González, John S. Burg, Niloufar J. Ataie, Amy J. Lam, Paula J. Cranfill, Michelle A. Baird, Michael W. Davidson, Ho-Leung Ng, K. Christopher Garcia, Christopher H. Contag, Kang Shen, Helen M. Blau, and Michael Z. Lin. 2014. "Non-Invasive Intravital Imaging of Cellular Differentiation with a Bright Red-Excitable Fluorescent Protein." *Nature Methods* 11(5):572–78.

Chuang, Chien-Hui, Anne E. Carpenter, Beata Fuchsova, Terezina Johnson, Primal de Lanerolle, and Andrew S. Belmont. 2006. "Long-Range Directional Movement of an Interphase Chromosome Site." *Current Biology : CB* 16(8):825–31.

Cleveland, D. W. 1995. "NuMA: A Protein Involved in Nuclear Structure, Spindle Assembly,

and Nuclear Re-Formation." *Trends in Cell Biology* 5(2):60–64.

Cremer, T. and C. Cremer. 2001. "Chromosome Territories, Nuclear Architecture and Gene Regulation in Mammalian Cells." *Nature Reviews. Genetics* 2(4):292–301.

Cremer, Thomas and Marion Cremer. 2010. "Chromosome Territories." *Cold Spring Harbor Perspectives in Biology* 2(3):a003889.

Crisp, Melissa, Qian Liu, Kyle Roux, J. B. Rattner, Catherine Shanahan, Brian Burke, Phillip D. Stahl, and Didier Hodzic. 2006. "Coupling of the Nucleus and Cytoplasm: Role of the LINC Complex." *Journal of Cell Biology* 172(1):41–53.

Dahl, Kris Noel, Samuel M. Kahn, Katherine L. Wilson, and Dennis E. Discher. 2004. "The Nuclear Envelope Lamina Network Has Elasticity and a Compressibility Limit Suggestive of a Molecular Shock Absorber." *Journal of Cell Science* 117(Pt 20):4779–86.

Dal-Pra, Sophie, Conrad P. Hodgkinson, Maria Mirotsou, Imke Kirste, and Victor J. Dzau. 2017. "Demethylation of H3K27 Is Essential for the Induction of Direct Cardiac Reprogramming by MIR Combo." *Circulation Research* 120(9):1403–13.

Das, A. T., M. E. Ludérus, and W. H. Lamers. 1993. "Identification and Analysis of a Matrix-Attachment Region 5' of the Rat Glutamate-Dehydrogenase-Encoding Gene." *European Journal of Biochemistry* 215(3):777–85.

Davidson, Patricia M. and Jan Lammerding. 2013. "Broken Nuclei - Lamins, Nuclear Mechanics, and Disease." *Trends in Cell Biology* 24(4):247–56.

Deguchi, Shinji, Shoko Kudo, Tsubasa S. Matsui, Wenjing Huang, and Masaaki Sato. 2015. "Piezoelectric Actuator-Based Cell Microstretch Device with Real-Time Imaging Capability." *AIP Advances* 5(6):1–6.

Dekker, Job, Andrew S. Belmont, Mitchell Guttman, Victor O. Leshyk, John T. Lis, Stavros

Lomvardas, Leonid A. Mirny, Clodagh C. O'Shea, Peter J. Park, Bing Ren, Joan C. Ritland Politz, Jay Shendure, Sheng Zhong, and the 4D Nucleome 4D Nucleome Network. 2017. "The 4D Nucleome Project." *Nature* 549(7671):219–26.

Dixon, Jesse R., Siddarth Selvaraj, Feng Yue, Audrey Kim, Yan Li, Yin Shen, Ming Hu, Jun S. Liu, and Bing Ren. 2012. "Topological Domains in Mammalian Genomes Identified by Analysis of Chromatin Interactions." *Nature* 485(7398):376–80.

Du, Zhenhai, Hui Zheng, Bo Huang, Rui Ma, Jingyi Wu, Xianglin Zhang, Jing He, Yunlong Xiang, Qiujun Wang, Yuanyuan Li, Jing Ma, Xu Zhang, Ke Zhang, Yang Wang, Michael Q. Zhang, Juntao Gao, Jesse R. Dixon, Xiaowo Wang, Jianyang Zeng, and Wei Xie. 2017. "Allelic Reprogramming of 3D Chromatin Architecture during Early Mammalian Development." *Nature* 547(7662):232–35.

Dundr, Miroslav, Jason K. Ospina, Myong-Hee Sung, Sam John, Madhvi Upender, Thomas Ried, Gordon L. Hager, and A. Gregory Matera. 2007. "Actin-Dependent Intranuclear Repositioning of an Active Gene Locus in Vivo." *The Journal of Cell Biology* 179(6):1095–1103.

Engler, Adam J., Christine Carag-Krieger, Colin P. Johnson, Matthew Raab, Hsin-Yao Tang, David W. Speicher, Joseph W. Sanger, Jean M. Sanger, and Dennis E. Discher. 2008. "Embryonic Cardiomyocytes Beat Best on a Matrix with Heart-like Elasticity: Scar-like Rigidity Inhibits Beating." *Journal of Cell Science* 121(Pt 22):3794–3802.

Engler, Adam J., Maureen A. Griffin, Shamik Sen, Carsten G. Bönnemann, H. Lee Sweeney, Dennis E. Discher, Christine Carag-Krieger, Colin P. Johnson, Matthew Raab, Hsin-Yao Tang, David W. Speicher, Jean M. Joseph W. Sanger, Jean M. Joseph W. Sanger, and Dennis E. Discher. 2004. "Myotubes Differentiate Optimally on Substrates with Tissue-like

Stiffness: Pathological Implications for Soft or Stiff Microenvironments." *Journal of Cell Biology* 166(6):877–87.

Engler, Adam J., Shamik Sen, H. Lee Sweeney, and Dennis E. Discher. 2006. "Matrix Elasticity Directs Stem Cell Lineage Specification." *Cell* 126(4):677–89.

Fanelli, C., S. Coppola, R. Barone, C. Colussi, G. Gualandi, P. Volpe, and L. Ghibelli. 1999. "Magnetic Fields Increase Cell Survival by Inhibiting Apoptosis via Modulation of Ca2+ Influx." *FASEB Journal : Official Publication of the Federation of American Societies for Experimental Biology* 13(1):95–102.

Fedorchak, Gregory R., Ashley Kaminski, and Jan Lammerding. 2014. "Cellular Mechanosensing: Getting to the Nucleus of It All." *Progress in Biophysics and Molecular Biology*.

Filion, Guillaume J., Joke G. van Bemmel, Ulrich Braunschweig, Wendy Talhout, Jop Kind, Lucas D. Ward, Wim Brugman, Inês J. de Castro, Ron M. Kerkhoven, Harmen J. Bussemaker, and Bas van Steensel. 2010. "Systematic Protein Location Mapping Reveals Five Principal Chromatin Types in Drosophila Cells." *Cell* 143(2):212–24.

Flyamer, Ilya M., Johanna Gassler, Maxim Imakaev, Hugo B. Brandão, Sergey V Ulianov, Nezar Abdennur, Sergey V Razin, Leonid A. Mirny, and Kikuë Tachibana-Konwalski. 2017. "Single-Nucleus Hi-C Reveals Unique Chromatin Reorganization at Oocyte-to-Zygote Transition." *Nature* 544(7648):110–14.

Gassler, Johanna, Hugo B. Brandão, Maxim Imakaev, Ilya M. Flyamer, Sabrina Ladstätter, Wendy A. Bickmore, Jan-Michael Peters, Leonid A. Mirny, and Kikuë Tachibana. 2017. "A Mechanism of Cohesin-Dependent Loop Extrusion Organizes Zygotic Genome Architecture." *The EMBO Journal* 36(24):3600–3618.

Ghodbane, Soumaya, Aida Lahbib, Mohsen Sakly, and Hafedh Abdelmelek. 2013. “Bioeffects of Static Magnetic Fields: Oxidative Stress, Genotoxic Effects, and Cancer Studies.” *BioMed Research International* 2013:602987.

Ghosh, Soham, Benjamin Seelbinder, Jonathan T. Henderson, Ryan D. Watts, Adrienne K. Scott, Alexander I. Veress, and Corey P. Neu. 2019. “Deformation Microscopy for Dynamic Intracellular and Intranuclear Mapping of Mechanics with High Spatiotemporal Resolution.” *Cell Reports* 27(5):1607-1620.e4.

Grady, R. Mark, Daniel a Starr, Gail L. Ackerman, Joshua R. Sanes, and Min Han. 2005. “Syne Proteins Anchor Muscle Nuclei at the Neuromuscular Junction.” *Proceedings of the National Academy of Sciences of the United States of America* 102(12):4359–64.

Guelen, Lars, Ludo Pagie, Emilie Brasset, Wouter Meuleman, Marius B. Faza, Wendy Talhout, Bert H. Eussen, Annelies de Klein, Lodewyk Wessels, Wouter de Laat, and Bas van Steensel. 2008. “Domain Organization of Human Chromosomes Revealed by Mapping of Nuclear Lamina Interactions.” *Nature* 453(7197):948–51.

Gueth-Hallonet, C., J. Wang, J. Harborth, K. Weber, and M. Osborn. 1998. “Induction of a Regular Nuclear Lattice by Overexpression of NuMA.” *Experimental Cell Research* 243(2):434–52.

Guilak, F., J. R. Tedrow, and R. Burgkart. 2000. “Viscoelastic Properties of the Cell Nucleus.” *Biochemical and Biophysical Research Communications* 269(3):781–86.

Guilluy, Christophe, Lukas D. Osborne, Laurianne Van Landeghem, Lisa Sharek, Richard Superfine, Rafael Garcia-Mata, and Keith Burridge. 2014. “Isolated Nuclei Adapt to Force and Reveal a Mechanotransduction Pathway in the Nucleus.” *Nature Cell Biology* 16(4):376–81.

Haque, Farhana, David J. Lloyd, Dawn T. Smallwood, Carolyn L. Dent, Catherine M. Shanahan, Andrew M. Fry, Richard C. Trembath, and Sue Shackleton. 2006. "SUN1 Interacts with Nuclear Lamin A and Cytoplasmic Nesprins to Provide a Physical Connection between the Nuclear Lamina and the Cytoskeleton." *Molecular and Cellular Biology* 26(10):3738–51.

Harshad, Kamble, Myeongjun Jun, Sungsu Park, Matthew J. Barton, Raja K. Vadivelu, James St John, and Nam Trung Nguyen. 2016. "An Electromagnetic Cell-Stretching Device for Mechanotransduction Studies of Olfactory Ensheathing Cells." *Biomedical Microdevices* 18(3):1–10.

Hemphill, Matthew A., Stephanie Dauth, Chung Jong Yu, Borna E. Dabiri, and Kevin Kit Parker. 2015. "Traumatic Brain Injury and the Neuronal Microenvironment: A Potential Role for Neuropathological Mechanotransduction." *Neuron* 85(6):1177–92.

Henderson, Jonathan T., Garrett Shannon, Alexander I. Veress, and Corey P. Neu. 2013. "Direct Measurement of Intranuclear Strain Distributions and RNA Synthesis in Single Cells Embedded within Native Tissue." *Biophysical Journal* 105(10):2252–61.

Heo, Su-Jin, Tristan P. Driscoll, Stephen D. Thorpe, Nandan L. Nerurkar, Brendon M. Baker, Michael T. Yang, Christopher S. Chen, David A. Lee, and Robert L. Mauck. 2016. "Differentiation Alters Stem Cell Nuclear Architecture, Mechanics, and Mechano-Sensitivity." *ELife* 5.

Heo, Su Jin, Stephen D. Thorpe, Tristan P. Driscoll, Randall L. Duncan, David A. Lee, and Robert L. Mauck. 2015. "Biophysical Regulation of Chromatin Architecture Instills a Mechanical Memory in Mesenchymal Stem Cells." *Scientific Reports* 5(5):16895.

Herbomel, G., A. Grichine, A. Fertin, A. Delon, C. Vourc'h, C. Souchier, and Y. Usson. 2016. "Wavelet Transform Analysis of Chromatin Texture Changes during Heat Shock." *Journal*

of Microscopy 262(3):295–305.

Hogan, Megan S., David Emlyn Parfitt, Cinthya J. Zepeda-Mendoza, Michael M. Shen, and David L. Spector. 2015. “Transient Pairing of Homologous Oct4 Alleles Accompanies the Onset of Embryonic Stem Cell Differentiation.” *Cell Stem Cell* 16(3):275–88.

Honda, Hiroaki, Hideaki Oda, Tetsuya Nakamoto, Zen Ichiro Honda, Ryuichi Sakai, Takahiro Suzuki, Toshiki Saito, Kenji Nakamura, Kazuki Nakao, Takatoshi Ishikawa, Motoya Katsuki, Yoshio Yazaki, and Hisamaru Hirai. 1998. “Cardiovascular Anomaly, Impaired Actin Bundling and Resistance to Src- Induced Transformation in Mice Lacking P130(Cas).” *Nature Genetics* 19(4):361–65.

Huang, Lawrence, Pattie S. Mathieu, and Brian P. Helmke. 2010. “A Stretching Device for High-Resolution Live-Cell Imaging.” *Annals of Biomedical Engineering* 38(5):1728–40.

Huang, Lingzhen, Liang Dong, Yantian Chen, Hanshi Qi, and Dengming Xiao. 2006. “Effects of Sinusoidal Magnetic Field Observed on Cell Proliferation, Ion Concentration, and Osmolarity in Two Human Cancer Cell Lines.” *Electromagnetic Biology and Medicine* 25(2):113–26.

Hug, Clemens B., Alexis G. Grimaldi, Kai Kruse, and Juan M. Vaquerizas. 2017. “Chromatin Architecture Emerges during Zygotic Genome Activation Independent of Transcription.” *Cell* 169(2):216-228.e19.

Hug, Clemens B. and Juan M. Vaquerizas. 2018. “The Birth of the 3D Genome during Early Embryonic Development.” *Trends in Genetics* 34(12):903–14.

Huh, Dongeun, Yu-suke Torisawa, Geraldine A. Hamilton, Hyun Jung Kim, and Donald E. Ingber. 2012. “Microengineered Physiological Biomimicry: Organs-on-Chips.” *Lab on a Chip* 12(12):2156–64.

Iyer, K. Venkatesan, S. Pulford, A. Mogilner, and G. V. Shivashankar. 2012. “Mechanical Activation of Cells Induces Chromatin Remodeling Preceding MKL Nuclear Transport.” *Biophysical Journal* 103(7):1416–28.

Jaalouk, Diana E. and Jan Lammerding. 2009. “Mechanotransduction Gone Awry.” *Nature Reviews. Molecular Cell Biology* 10(1):63–73.

Jacot, Jeffrey G., Andrew D. McCulloch, and Jeffrey H. Omens. 2008. “Substrate Stiffness Affects the Functional Maturation of Neonatal Rat Ventricular Myocytes.” *Biophysical Journal* 95(7):3479–87.

Joffe, Boris, Heinrich Leonhardt, and Irina Solovei. 2010. “Differentiation and Large Scale Spatial Organization of the Genome.” *Current Opinion in Genetics & Development* 20(5):562–69.

Jung, Yoon Hee, Michael E. G. Sauria, Xiaowen Lyu, Manjinder S. Cheema, Juan Ausio, James Taylor, and Victor G. Corces. 2017. “Chromatin States in Mouse Sperm Correlate with Embryonic and Adult Regulatory Landscapes.” *Cell Reports* 18(6):1366–82.

Juutilainen, J. and K. Saali. 1986. “Development of Chick Embryos in 1 Hz to 100 KHz Magnetic Fields.” *Radiation and Environmental Biophysics* 25(2):135–40.

Kaaij, Lucas J. T., Robin H. van der Weide, René F. Ketting, and Elzo de Wit. 2018. “Systemic Loss and Gain of Chromatin Architecture throughout Zebrafish Development.” *Cell Reports* 24(1):1-10.e4.

Ke, Yuwen, Yanan Xu, Xuepeng Chen, Songjie Feng, Zhenbo Liu, Yaoyu Sun, Xuelong Yao, Fangzhen Li, Wei Zhu, Lei Gao, Haojie Chen, Zhenhai Du, Wei Xie, Xiaocui Xu, Xingxu Huang, and Jiang Liu. 2017. “3D Chromatin Structures of Mature Gametes and Structural Reprogramming during Mammalian Embryogenesis.” *Cell* 170(2):367-381.e20.

Kennani, Sara El, Annie Adrait, Alexey K. Shaytan, Saadi Khochbin, Christophe Bruley, Anna R. Panchenko, David Landsman, Delphine Pflieger, and Jérôme Govin. 2017. "MS_HistoneDB, a Manually Curated Resource for Proteomic Analysis of Human and Mouse Histones." *Epigenetics & Chromatin* 10:2.

Khatau, Shyam B., Christopher M. Hale, P. J. Stewart-Hutchinson, Meet S. Patel, Colin L. Stewart, Peter C. Searson, Didier Hodzic, and Denis Wirtz. 2009. "A Perinuclear Actin Cap Regulates Nuclear Shape." *Proceedings of the National Academy of Sciences* 106(45):19017–22.

Kim, S. H., P. G. McQueen, M. K. Lichtman, E. M. Shevach, L. A. Parada, and T. Misteli. 2004. "Spatial Genome Organization during T-Cell Differentiation." *Cytogenetic and Genome Research* 105(2–4):292–301.

Koehler, Daniela, Valeri Zakhartchenko, Lutz Froenicke, Gary Stone, Roscoe Stanyon, Eckhard Wolf, Thomas Cremer, and Alessandro Brero. 2009. "Changes of Higher Order Chromatin Arrangements during Major Genome Activation in Bovine Preimplantation Embryos." *Experimental Cell Research* 315(12):2053–63.

Kovacic-Milivojević, Branka, Caroline C. Damsky, David G. Gardner, and Dusko Ilić. 2002. "Requirements for the Localization of P130 Cas to Z-Lines in Cardiac Myocytes." *Cellular & Molecular Biology Letters* 7(2):323–29.

Kulashreshtha, Mugdha, Ishita S. Mehta, Pradeep Kumar, and Basuthkar J. Rao. 2016. "Chromosome Territory Relocation during DNA Repair Requires Nuclear Myosin 1 Recruitment to Chromatin Mediated by ϒ-H2AX Signaling." *Nucleic Acids Research* 44(17):8272–91.

de Laat, Wouter and Frank Grosveld. 2003. "Spatial Organization of Gene Expression: The

Active Chromatin Hub." *Chromosome Research : An International Journal on the Molecular, Supramolecular and Evolutionary Aspects of Chromosome Biology* 11(5):447–59.

Lampi, Marsha C. and Cynthia A. Reinhart-King. 2018. "Targeting Extracellular Matrix Stiffness to Attenuate Disease: From Molecular Mechanisms to Clinical Trials." *Science Translational Medicine* 10(422):eaao0475.

de Las Heras, Jose I., Peter Meinke, Dzmitry G. Batrakou, Vlastimil Srsen, Nikolaj Zuleger, Alastair Rw Kerr, and Eric C. Schirmer. 2014. "Tissue Specificity in the Nuclear Envelope Supports Its Functional Complexity." *Nucleus (Austin, Tex.)* 4(6):460–77.

Lawrence, Moyra, Sylvain Daujat, and Robert Schneider. 2016. "Lateral Thinking: How Histone Modifications Regulate Gene Expression." *Trends in Genetics* 32(1):42–56.

Le, Huy Quang, Sushmita Ghatak, Ching-Yan Chloé Yeung, Frederik Tellkamp, Christian Günschmann, Christoph Dieterich, Assa Yeroslaviz, Bianca Habermann, Ana Pombo, Carien M. Niessen, and Sara A. Wickström. 2016. "Mechanical Regulation of Transcription Controls Polycomb-Mediated Gene Silencing during Lineage Commitment." *Nature Cell Biology* 18(8):864–75.

Lee, Hyungsuk, William J. Adams, Patrick W. Alford, Megan L. McCain, Adam W. Feinberg, Sean P. Sheehy, Josue A. Goss, and Kevin Kit Parker. 2015. "Cytoskeletal Prestress Regulates Nuclear Shape and Stiffness in Cardiac Myocytes." *Experimental Biology and Medicine (Maywood, N.J.)* 240(11):1543–54.

Li, Qiaoling, Tingting Hu, Liang Chen, Jiayin Sun, Jun Xie, Rang Li, and Biao Xu. 2015. "Selection of Reference Genes for Normalization of Quantitative Polymerase Chain Reaction Data in Mouse Models of Heart Failure." *Molecular Medicine Reports* 11(1):393–

99.

Lieberman-Aiden, Erez, Nynke L. van Berkum, Louise Williams, Maxim Imakaev, Tobias Ragoczy, Agnes Telling, Ido Amit, Bryan R. Lajoie, Peter J. Sabo, Michael O. Dorschner, Richard Sandstrom, Bradley Bernstein, M. A. Bender, Mark Groudine, Andreas Gnirke, John Stamatoyannopoulos, Leonid A. Mirny, Eric S. Lander, and Job Dekker. 2009. "Comprehensive Mapping of Long-Range Interactions Reveals Folding Principles of the Human Genome." *Science (New York, N.Y.)* 326(5950):289–93.

Liu, Jiaqiang, Jing Liu, Jing Mao, Xiao Yuan, Zhu Lin, and Yongming Li. 2009. "Caspase-3-Mediated Cyclic Stretch-Induced Myoblast Apoptosis via a Fas/FasL-Independent Signaling Pathway during Myogenesis." *Journal of Cellular Biochemistry* 107(4):834–44.

Lu, Wenshu, Maria Schneider, Sascha Neumann, Verena Maren Jaeger, Surayya Taranum, Martina Munck, Sarah Cartwright, Christine Richardson, James Carthew, Kowoon Noh, Martin Goldberg, Angelika A. Noegel, and Iakowos Karakesisoglou. 2012. "Nesprin Interchain Associations Control Nuclear Size." *Cellular and Molecular Life Sciences* 69(20):3493–3509.

Lydersen, B. K. and D. E. Pettijohn. 1980. "Human-Specific Nuclear Protein That Associates with the Polar Region of the Mitotic Apparatus: Distribution in a Human/Hamster Hybrid Cell." *Cell* 22(2 Pt 2):489–99.

Makatsori, Dimitra, Niki Kourmouli, Hara Polioudaki, Leonard D. Shultz, Kelvin McLean, Panayiotis A. Theodoropoulos, Prim B. Singh, and Spyros D. Georgatos. 2004. "The Inner Nuclear Membrane Protein Lamin B Receptor Forms Distinct Microdomains and Links Epigenetically Marked Chromatin to the Nuclear Envelope." *The Journal of Biological Chemistry* 279(24):25567–73.

Malone, C. J., W. D. Fixsen, H. R. Horvitz, and M. Han. 1999. “UNC-84 Localizes to the Nuclear Envelope and Is Required for Nuclear Migration and Anchoring during C. Elegans Development.” *Development (Cambridge, England)* 126(14):3171–81.

Manilal, S., T. M. Nguyen, C. A. Sewry, and G. E. Morris. 1996. “The Emery-Dreifuss Muscular Dystrophy Protein, Emerin, Is a Nuclear Membrane Protein.” *Human Molecular Genetics* 5(6):801–8.

Manuelidis, L. 1985. “Individual Interphase Chromosome Domains Revealed by in Situ Hybridization.” *Human Genetics* 71(4):288–93.

Martiel, Jean-Louis, Aldo Leal, Laetitia Kurzawa, Martial Balland, Irene Wang, Timothée Vignaud, Qingzong Tseng, and Manuel Théry. 2015. “Measurement of Cell Traction Forces with ImageJ.” *Methods in Cell Biology* 125:269–87.

Martino, Alessandro, Manuela Cabiati, Manuela Campan, Tommaso Prescimone, Daiana Minocci, Chiara Caselli, Anna Maria Rossi, Daniela Giannessi, and Silvia Del Ry. 2011. “Selection of Reference Genes for Normalization of Real-Time PCR Data in Minipig Heart Failure Model and Evaluation of TNF-α MRNA Expression.” *Journal of Biotechnology* 153(3–4):92–99.

Matharu, Navneet and Nadav Ahituv. 2015. “Minor Loops in Major Folds: Enhancer-Promoter Looping, Chromatin Restructuring, and Their Association with Transcriptional Regulation and Disease.” edited by E. M. C. Fisher. *PLoS Genetics* 11(12):e1005640.

Mayr, Manuel, Yanhua Hu, Hainaut Hainaut, and Qingbo Xu. 2002. “Mechanical Stress-Induced DNA Damage and Rac-P38MAPK Signal Pathways Mediate P53-Dependent Apoptosis in Vascular Smooth Muscle Cells.” *FASEB Journal : Official Publication of the Federation of American Societies for Experimental Biology* 16(11):1423–25.

Mehta, Ishita S., Manelle Amira, Amanda J. Harvey, and Joanna M. Bridger. 2010. “Rapid Chromosome Territory Relocation by Nuclear Motor Activity in Response to Serum Removal in Primary Human Fibroblasts.” *Genome Biology* 11(1):R5.

Miyakoshi, Junji. 2005. “Effects of Static Magnetic Fields at the Cellular Level.” *Progress in Biophysics and Molecular Biology* 87(2–3):213–23.

Mysliwiec, Matthew R., Clayton D. Carlson, Josh Tietjen, Holly Hung, Aseem Z. Ansari, and Youngsook Lee. 2012. “Jarid2 (Jumonji, AT Rich Interactive Domain 2) Regulates NOTCH1 Expression via Histone Modification in the Developing Heart.” *Journal of Biological Chemistry* 287(2):1235–41.

Ni, Zhuoyu, Abbie Saunders, Nicholas J. Fuda, Jie Yao, Jose-Ramon Suarez, Watt W. Webb, and John T. Lis. 2008. “P-TEFb Is Critical for the Maturation of RNA Polymerase II into Productive Elongation in Vivo.” *Molecular and Cellular Biology* 28(3):1161–70.

Nickerson, J. 2001. “Experimental Observations of a Nuclear Matrix.” *Journal of Cell Science* 114(Pt 3):463–74.

Nozaki, Tadasu, Ryosuke Imai, Mai Tanbo, Ryosuke Nagashima, Sachiko Tamura, Tomomi Tani, Yasumasa Joti, Masaru Tomita, Kayo Hibino, Masato T. Kanemaki, Kerstin S. Wendt, Yasushi Okada, Takeharu Nagai, and Kazuhiro Maeshima. 2017. “Dynamic Organization of Chromatin Domains Revealed by Super-Resolution Live-Cell Imaging.” *Molecular Cell* 67(2):282-293.e7.

Olins, Ada L. and Donald E. Olins. 2004. “Cytoskeletal Influences on Nuclear Shape in Granulocytic HL-60 Cells.” *BMC Cell Biology* 5(1):30.

Olins, Ada L., Monika Zwerger, Harald Herrmann, Hanswalter Zentgraf, Amos J. Simon, Marc Monestier, and Donald E. Olins. 2008. “The Human Granulocyte Nucleus: Unusual Nuclear

Envelope and Heterochromatin Composition." *European Journal of Cell Biology* 87(5):279–90.

Panagopoulos, Dimitris J., Andreas Karabarbounis, and Lukas H. Margaritis. 2002. "Mechanism for Action of Electromagnetic Fields on Cells." *Biochemical and Biophysical Research Communications* 298(1):95–102.

Parada, Luis A., Philip G. McQueen, and Tom Misteli. 2004. "Tissue-Specific Spatial Organization of Genomes." *Genome Biology* 5(7):R44.

Pasqualini, Francesco Silvio, Ashutosh Agarwal, Blakely Bussie O'Connor, Qihan Liu, Sean P. Sheehy, and Kevin Kit Parker. 2018. "Traction Force Microscopy of Engineered Cardiac Tissues" edited by N. D. Leipzig. *PLOS ONE* 13(3):e0194706.

Pendleton, Annmarie, Brian Pope, Alan Weeds, and Anna Koffer. 2003. "Latrunculin B or ATP Depletion Induces Cofilin-Dependent Translocation of Actin into Nuclei of Mast Cells." *Journal of Biological Chemistry* 278(16):14394–400.

Pereyra, Andrea S., Like Y. Hasek, Kate L. Harris, Alycia G. Berman, Frederick W. Damen, Craig J. Goergen, and Jessica M. Ellis. 2017. "Loss of Cardiac Carnitine Palmitoyltransferase 2 Results in Rapamycin-Resistant, Acetylation-Independent Hypertrophy." *The Journal of Biological Chemistry* 292(45):18443–56.

Phillip, Jude M., Ivie Aifuwa, Jeremy Walston, and Denis Wirtz. 2015. "The Mechanobiology of Aging." *Annual Review of Biomedical Engineering* 17(1):113–41.

Pierce, Benjamin A. 2005. *Genetics : A Conceptual Approach*. 2nd ed. W.H. Freeman.

Pirozzoli, M. C., C. Marino, G. A. Lovisolo, C. Laconi, L. Mosiello, and A. Negroni. 2003. "Effects of 50 Hz Electromagnetic Field Exposure on Apoptosis and Differentiation in a Neuroblastoma Cell Line." *Bioelectromagnetics* 24(7):510–16.

Politz, Joan C. Ritland, Tobias Ragoczy, and Mark Groudine. “When Untethered, Something Silent inside Comes.” *Nucleus (Austin, Tex.)* 4(3):153–55.

Pombo, Ana and Niall Dillon. 2015. “Three-Dimensional Genome Architecture: Players and Mechanisms.” *Nature Reviews. Molecular Cell Biology* 16(4):245–57.

Pope, Benjamin D., Tyrone Ryba, Vishnu Dileep, Feng Yue, Weisheng Wu, Olgert Denas, Daniel L. Vera, Yanli Wang, R. Scott Hansen, Theresa K. Canfield, Robert E. Thurman, Yong Cheng, Günhan Gülsoy, Jonathan H. Dennis, Michael P. Snyder, John A. Stamatoyannopoulos, James Taylor, Ross C. Hardison, Tamer Kahveci, Bing Ren, and David M. Gilbert. 2014. “Topologically Associating Domains Are Stable Units of Replication-Timing Regulation.” *Nature* 515(7527):402–5.

Puckelwartz, Megan J., Eric J. Kessler, Gene Kim, Megan M. Dewitt, Yuan Zhang, Judy U. Earley, Frederic F. S. Depreux, James Holaska, Stephanie K. Mewborn, Peter Pytel, and Elizabeth M. McNally. 2010. “Nesprin-1 Mutations in Human and Murine Cardiomyopathy.” *Journal of Molecular and Cellular Cardiology* 48(4):600–608.

Pugach, Emily K., Christa L. Blenck, Joseph M. Dragavon, Stephen J. Langer, and Leslie A. Leinwand. 2016. “Estrogen Receptor Profiling and Activity in Cardiac Myocytes.” *Molecular and Cellular Endocrinology* 431:62–70.

Queisser, Gillian, Simon Wiegert, and Hilmar Bading. 2011. “Structural Dynamics of the Cell Nucleus: Basis for Morphology Modulation of Nuclear Calcium Signaling and Gene Transcription.” *Nucleus (Austin, Tex.)* 2(2):98–104.

Rabl, Carl. 1885. “Über Zelltheilung.” *Morphol. Jahrb.* 10:214–330.

Radulescu, Andreea E. and Don W. Cleveland. 2010. “NuMA after 30 Years: The Matrix Revisited.” *Trends in Cell Biology* 20(4):214–22.

Rao, Suhas S. P., Su-Chen Huang, Brian Glenn St Hilaire, Jesse M. Engreitz, Elizabeth M. Perez, Kyong-Rim Kieffer-Kwon, Adrian L. Sanborn, Sarah E. Johnstone, Gavin D. Bascom, Ivan D. Bochkov, Xingfan Huang, Muhammad S. Shamim, Jaeweon Shin, Douglass Turner, Ziyi Ye, Arina D. Omer, James T. Robinson, Tamar Schlick, Bradley E. Bernstein, Rafael Casellas, Eric S. Lander, and Erez Lieberman Aiden. 2017. "Cohesin Loss Eliminates All Loop Domains." *Cell* 171(2):305-320.e24.

Rao, Suhas S. P., Miriam H. Huntley, Neva C. Durand, Elena K. Stamenova, Ivan D. Bochkov, James T. Robinson, Adrian L. Sanborn, Ido Machol, Arina D. Omer, Eric S. Lander, and Erez Lieberman Aiden. 2014. "A 3D Map of the Human Genome at Kilobase Resolution Reveals Principles of Chromatin Looping." *Cell* 159(7):1665–80.

del Real, Alvaro, Flor M. Pérez-Campo, Agustín F. Fernández, Carolina Sañudo, Carmen G. Ibarbia, María I. Pérez-Núñez, Wim Van Criekinge, Maarten Braspenning, María A. Alonso, Mario F. Fraga, and Jose A. Riancho. 2017. "Differential Analysis of Genome-Wide Methylation and Gene Expression in Mesenchymal Stem Cells of Patients with Fractures and Osteoarthritis." *Epigenetics* 12(2):113–22.

Riccio, Antonella. 2010. "Dynamic Epigenetic Regulation in Neurons: Enzymes, Stimuli and Signaling Pathways." *Nature Neuroscience* 13(11):1330–37.

Rogakou, Emmy P., Duane R. Pilch, Ann H. Orr, Vessela S. Ivanova, and William M. Bonner. 1998. "DNA Double-Stranded Breaks Induce Histone H2AX Phosphorylation on Serine 139." *Journal of Biological Chemistry* 273(10):5858–68.

Rose, Beth A., Thomas Force, and Yibin Wang. 2010. "Mitogen-Activated Protein Kinase Signaling in the Heart: Angels versus Demons in a Heart-Breaking Tale." *Physiological Reviews* 90(4):1507–46.

Rosellini, Elisabetta, Yu Shrike Zhang, Bianca Migliori, Niccoletta Barbani, Luigi Lazzeri, Su Ryon Shin, Mehmet Remzi Dokmeci, and Maria Grazia Cascone. 2018. "Protein/Polysaccharide-Based Scaffolds Mimicking Native Extracellular Matrix for Cardiac Tissue Engineering Applications." *Journal of Biomedical Materials Research Part A* 106(3):769–81.

Sawada, Yasuhiro, Masako Tamada, Benjamin J. Dubin-Thaler, Oksana Cherniavskaya, Ryuichi Sakai, Sakae Tanaka, and Michael P. Sheetz. 2006. "Force Sensing by Mechanical Extension of the Src Family Kinase Substrate P130Cas." *Cell* 127(5):1015–26.

Seelbinder, Benjamin, Soham Ghosh, Alycia G. Berman, Stephanie E. Schneider, Craig J. Goergen, Sarah Calve, and Corey P. Neu. 2018. "The Nucleus Mediates Mechanosensitive Reorganization of Epigenetically Marked Chromatin during Cardiac Maturation and Pathology." *BioRXiv*.

Sexton, Tom, Heiko Schober, Peter Fraser, and Susan M. Gasser. 2007. "Gene Regulation through Nuclear Organization." *Nature Structural & Molecular Biology* 14(11):1049–55.

Shao, Yue, Xinyu Tan, Roman Novitski, Mishaal Muqaddam, Paul List, Laura Williamson, Jianping Fu, and Allen P. Liu. 2013. "Uniaxial Cell Stretching Device for Live-Cell Imaging of Mechanosensitive Cellular Functions." *Review of Scientific Instruments* 84(11):1–8.

Solovei, I. and B. Joffe. 2010. "Inverted Nuclear Architecture and Its Development during Differentiation of Mouse Rod Photoreceptor Cells: A New Model to Study Nuclear Architecture." *Russian Journal of Genetics* 46(9):1029–32.

Solovei, Irina, Moritz Kreysing, Christian Lanctôt, Süleyman Kösem, Leo Peichl, Thomas Cremer, Jochen Guck, and Boris Joffe. 2009. "Nuclear Architecture of Rod Photoreceptor

Cells Adapts to Vision in Mammalian Evolution." *Cell* 137(2):356–68.

Solovei, Irina, Audrey S. Wang, Katharina Thanisch, Christine S. Schmidt, Stefan Krebs, Monika Zwerger, Tatiana V Cohen, Didier Devys, Roland Foisner, Leo Peichl, Harald Herrmann, Helmut Blum, Dieter Engelkamp, Colin L. Stewart, Heinrich Leonhardt, and Boris Joffe. 2013. "LBR and Lamin A/C Sequentially Tether Peripheral Heterochromatin and Inversely Regulate Differentiation." *Cell* 152(3):584–98.

Somech, Raz, Sigal Shaklai, Orit Geller, Ninette Amariglio, Amos J. Simon, Gideon Rechavi, and Einav Nili Gal-Yam. 2005. "The Nuclear-Envelope Protein and Transcriptional Repressor LAP2beta Interacts with HDAC3 at the Nuclear Periphery, and Induces Histone H4 Deacetylation." *Journal of Cell Science* 118(Pt 17):4017–25.

Spagnol, Stephen T., Travis J. Armiger, and Kris Noel Dahl. 2016. "Mechanobiology of Chromatin and the Nuclear Interior." *Cellular and Molecular Bioengineering* 9(2):268–76.

Spitzer, Nicholas C. 2006. "Electrical Activity in Early Neuronal Development." *Nature* 444(7120):707–12.

Sreejit, P., Suresh Kumar, and Rama S. Verma. 2008. "An Improved Protocol for Primary Culture of Cardiomyocyte from Neonatal Mice." *In Vitro Cellular & Developmental Biology - Animal* 44(3–4):45–50.

Stephens, Andrew D., Patrick Z. Liu, Edward J. Banigan, Luay M. Almassalha, Vadim Backman, Stephen A. Adam, Robert D. Goldman, and John F. Marko. 2018. "Chromatin Histone Modifications and Rigidity Affect Nuclear Morphology Independent of Lamins." edited by T. Misteli. *Molecular Biology of the Cell* 29(2):220–33.

Sutherland, H. and W. A. Bickmore. 2009. "Transcription Factories: Gene Expression in Unions?" *Nature Reviews Genetics* 10(7):457–66.

Swift, Joe, Irena L. Ivanovska, Amnon Buxboim, Takamasa Harada, P. C. Dave P. Dingal, Joel Pinter, J. David Pajerowski, Kyle R. Spinler, Jae-Won Shin, Manorama Tewari, Florian Rehfeldt, David W. Speicher, and Dennis E. Discher. 2013. "Nuclear Lamin-A Scales with Tissue Stiffness and Enhances Matrix-Directed Differentiation." *Science (New York, N.Y.)* 341(6149):1240104.

Tajik, Arash, Yuejin Zhang, Fuxiang Wei, Jian Sun, Qiong Jia, Wenwen Zhou, Rishi Singh, Nimish Khanna, Andrew S. Belmont, and Ning Wang. 2016. "Transcription Upregulation via Force-Induced Direct Stretching of Chromatin." *Nature Materials*.

Tenuzzo, Bernadette, Alfonsina Chionna, Elisa Panzarini, Remigio Lanubile, Patrizia Tarantino, Bruno Di Jeso, Majdi Dwikat, and Luciana Dini. 2006. "Biological Effects of 6 MT Static Magnetic Fields: A Comparative Study in Different Cell Types." *Bioelectromagnetics* 27(7):560–77.

Terme, Jean-Michel, Borja Sesé, Lluis Millán-Ariño, Regina Mayor, Juan Carlos Izpisúa Belmonte, María José Barrero, and Albert Jordan. 2011. "Histone H1 Variants Are Differentially Expressed and Incorporated into Chromatin during Differentiation and Reprogramming to Pluripotency." *The Journal of Biological Chemistry* 286(41):35347–57.

Thienpont, Bernard, Jan Magnus Aronsen, Emma Louise Robinson, Hanneke Okkenhaug, Elena Loche, Arianna Ferrini, Patrick Brien, Kanar Alkass, Antonio Tomasso, Asmita Agrawal, Olaf Bergmann, Ivar Sjaastad, Wolf Reik, and Hywel Llewelyn Roderick. 2017. "The H3K9 Dimethyltransferases EHMT1/2 Protect against Pathological Cardiac Hypertrophy." *The Journal of Clinical Investigation* 127(1):335–48.

Toume, Samer, Amit Gefen, and Daphne Weihs. 2016. "Printable Low-Cost, Sustained and Dynamic Cell Stretching Apparatus." *Journal of Biomechanics* 49(8):1336–39.

Tsuda, Y., H. Yasutake, A. Ishijima, and T. Yanagida. 1996. “Torsional Rigidity of Single Actin Filaments and Actin-Actin Bond Breaking Force under Torsion Measured Directly by in Vitro Micromanipulation.” *Proceedings of the National Academy of Sciences of the United States of America* 93(23):12937–42.

Upadhyay, Daya, Eduardo Correa-Meyer, Jacob I. Sznajder, and David W. Kamp. 2003. “FGF-10 Prevents Mechanical Stretch-Induced Alveolar Epithelial Cell DNA Damage via MAPK Activation.” *American Journal of Physiology. Lung Cellular and Molecular Physiology* 284(2):L350-9.

Uzer, Gunes, William R. Thompson, Buer Sen, Zhihui Xie, Sherwin S. Yen, Sean Miller, Guniz Bas, Maya Styner, Clinton T. Rubin, Stefan Judex, Keith Burridge, and Janet Rubin. 2015. “Cell Mechanosensitivity to Extremely Low-Magnitude Signals Is Enabled by a LINCed Nucleus.” *Stem Cells* 33(6):2063–76.

Valenzuela, Nicolas, Qiying Fan, Faisal Fa’ak, Benjamin Soibam, Harika Nagandla, Yu Liu, Robert J. Schwartz, Bradley K. McConnell, and M. David Stewart. 2016. “Cardiomyocyte-Specific Conditional Knockout of the Histone Chaperone HIRA in Mice Results in Hypertrophy, Sarcolemmal Damage and Focal Replacement Fibrosis.” *Disease Models & Mechanisms* 9(3):335–45.

Vergnes, L., M. Peterfy, M. O. Bergo, S. G. Young, and K. Reue. 2004. “Lamin B1 Is Required for Mouse Development and Nuclear Integrity.” *Proceedings of the National Academy of Sciences* 101(28):10428–33.

Vietri Rudan, Matteo, Christopher Barrington, Stephen Henderson, Christina Ernst, Duncan T. Odom, Amos Tanay, and Suzana Hadjur. 2015. “Comparative Hi-C Reveals That CTCF Underlies Evolution of Chromosomal Domain Architecture.” *Cell Reports* 10(8):1297–

1309.

Wijchers, Patrick J., Peter H. L. Krijger, Geert Geeven, Yun Zhu, Annette Denker, Marjon J. A. M. Verstegen, Christian Valdes-Quezada, Carlo Vermeulen, Mark Janssen, Hans Teunissen, Lisette C. M. Anink-Groenen, Pernette J. Verschure, and Wouter de Laat. 2016. "Cause and Consequence of Tethering a SubTAD to Different Nuclear Compartments." *Molecular Cell* 61(3):461–73.

Wilkie, Gavin S., Nadia Korfali, Selene K. Swanson, Poonam Malik, Vlastimil Srsen, Dzmitry G. Batrakou, Jose de las Heras, Nikolaj Zuleger, Alastair R. W. Kerr, Laurence Florens, and Eric C. Schirmer. 2011. "Several Novel Nuclear Envelope Transmembrane Proteins Identified in Skeletal Muscle Have Cytoskeletal Associations." *Molecular & Cellular Proteomics* 10(1):M110.003129.

Wittmann, Malte, Gillian Queisser, Anja Eder, J. Simon Wiegert, C. Peter Bengtson, Andrea Hellwig, Gabriel Wittum, and Hilmar Bading. 2009. "Synaptic Activity Induces Dramatic Changes in the Geometry of the Cell Nucleus: Interplay between Nuclear Structure, Histone H3 Phosphorylation, and Nuclear Calcium Signaling." *The Journal of Neuroscience : The Official Journal of the Society for Neuroscience* 29(47):14687–700.

Wong, Xianrong, Teresa R. Luperchio, and Karen L. Reddy. 2014. "NET Gains and Losses: The Role of Changing Nuclear Envelope Proteomes in Genome Regulation." *Current Opinion in Cell Biology* 28:105–20.

Worke, L. J., J. E. Barthold, B. Seelbinder, T. Novak, R. P. Main, S. L. Harbin, and C. P. Neu. 2017. "Densification of Type I Collagen Matrices as a Model for Cardiac Fibrosis." *Advanced Healthcare Materials* 6(22).

Wutz, Gordana, Csilla Várnai, Kota Nagasaka, David A. Cisneros, Roman R. Stocsits, Wen

Tang, Stefan Schoenfelder, Gregor Jessberger, Matthias Muhar, M. Julius Hossain, Nike Walther, Birgit Koch, Moritz Kueblbeck, Jan Ellenberg, Johannes Zuber, Peter Fraser, and Jan-Michael Peters. 2017. "Topologically Associating Domains and Chromatin Loops Depend on Cohesin and Are Regulated by CTCF, WAPL, and PDS5 Proteins." *The EMBO Journal* 36(24):3573–99.

Xia, Wenlong and Jianwei Jiao. 2017. "Histone Variant H3.3 Orchestrates Neural Stem Cell Differentiation in the Developing Brain." *Cell Death and Differentiation* 24(9):1548–63.

Xu, Xin, Zhiyu Li, Luyao Cai, Sarah Calve, and Corey P. Neu. 2016. "Mapping the Nonreciprocal Micromechanics of Individual Cells and the Surrounding Matrix Within Living Tissues." *Scientific Reports* 6(1):24272.

Yahalom-Ronen, Yfat, Dana Rajchman, Rachel Sarig, Benjamin Geiger, and Eldad Tzahor. 2015. "Reduced Matrix Rigidity Promotes Neonatal Cardiomyocyte Dedifferentiation, Proliferation and Clonal Expansion." *ELife* 4.

Young, Jennifer L., Kyle Kretchmer, Matthew G. Ondeck, Alexander C. Zambon, and Adam J. Engler. 2014. "Mechanosensitive Kinases Regulate Stiffness-Induced Cardiomyocyte Maturation." *Scientific Reports* 4:6425.

Zhang, Qing Jun, Hou Zao Chen, Lin Wang, De Pei Liu, Joseph A. Hill, and Zhi Ping Liu. 2011. "The Histone Trimethyllysine Demethylase JMJD2A Promotes Cardiac Hypertrophy in Response to Hypertrophic Stimuli in Mice." *Journal of Clinical Investigation* 121(6):2447–56.

Zhang, Qiuping, Cassandra Ragnauth, Marc J. Greener, Catherine M. Shanahan, and Roland G. Roberts. 2002. "The Nesprins Are Giant Actin-Binding Proteins, Orthologous to Drosophila Melanogaster Muscle Protein MSP-300." *Genomics* 80(5):473–81.

Zorn, Christian, Thomas Cremer, Christoph Cremer, and J�rgen Zimmer. 1976. “Laser UV Microirradiation of Interphase Nuclei and Post-Treatment with Caffeine.” *Human Genetics* 35(1):83–89.

Zuleger, Nikolaj, Shelagh Boyle, David a Kelly, Jose I. de Las Heras, Vassiliki Lazou, Nadia Korfali, Dzmitry G. Batrakou, K. Natalie Randles, Glenn E. Morris, David J. Harrison, Wendy a Bickmore, and Eric C. Schirmer. 2013. “Specific Nuclear Envelope Transmembrane Proteins Can Promote the Location of Chromosomes to and from the Nuclear Periphery.” *Genome Biology* 14(2):R14.